博士論文

Theoretical study on peculiar optical responses in metal grating

(金属グレーティングにおける特異な光学応答の理論的研究)

吉川　遼

広島大学大学院先端物質科学研究科

2020 年 3 月

目次

主論文

Contents

Chapter 1

Introduction

1.1 Optics in society

Light [1] is a fundamental matter for us. We get the image of the objects through light, in other words, we mainly depend the recognition of our surroundings on our eyes. From very old times, people have been manipulating light in their lives. For example, mirrors are the most primitive tool to change the direction of propagating light by the reflection. Lenses are other primitive tools. Using lenses, the light can be concentrated at one point. It is said that people used magnifying glasses in ancient Roman times. During the middle ages, various important optical tools were invented. Eyeglasses were invented in the 14th century, which are still used in today's world. Microscopes and telescopes are invented in the 17th century. The invention of these two greatly contributed to the promotion of the various field of science such as Biology or Astronomy. One of the most significant invention for our society occurred in the 20th century; the lasers. The Internet has been developed so much as today because the optical fiber communication was enabled by lasers. The compact data storage such as CDs or DVDs were also realized. In addition, lasers are used in surgery. These are only a few examples of whole applications of light. Of course, the LED is another important invention.

In the present days, technologies using light still have many potentials to solve various problems. In addition to the classical optics, the research field of photonics or especially nanophotonics, which will be described in detail in the next section has intensively studied for a few decades. The difference between optics and photonics are not always clear, however, the former sometimes refer to the study of light in macro scale using the glass lenses and prisms while the latter refers to the study of light in micro scale in which photon is involved. The study of (nano)photonics became popular by the recent development of nano fabrication technologies.

One of the most expected application is photonic integrated circuit, in which the light is used as a signal instead of electrons. Since the invention of the integration technologies, the density of integrated circuit has been rising, and contributed to the dramatic development of the computers. In these days, however, problems such as the

high power consumption and heat generation arise because of the quite high miniaturization of current integrated circuits. These problems prevent further development of the computers. Since the photonic integrated circuit might solve the above problems, it is considered as the alternative means in the future.

Photonics also handles with energy problem. Because of the environmental problems and the increasing the total amount of energy consumption in the world, renewable energy is considered for the stable energy supply. Most familiar one is solar energy. The current efficiency of the solar cell is relatively low which is about 20 percents. It is expected the techonology of photonics enables realizing better efficiency.

Let us take a look at the study of light. The attempt to elucidate the nature of light has also been conducted from the old time. In B.C., the ancient Greek or Roman philosophers such as Democritus and Aristotle tried to identify the concepts of light. However, it is relatively the recent era, the 17th century when the theory of optics was developed dramatically. In the 17th century, the study for the fundamental properties of light such as polarization, birefringence, the color of light and velocity is greatly advanced. Refraction theory was developed by scientists like Snell, Fermat, and Huygens. Newton who formulated the fundamental law of classical dynamics also contributed to optics. Newton argued that the white light was composed of the summation of waves with different colors, which is a quite common fact in today's optics.

In the following centuries, the theory of light developed and eventually, the behavior of light could be described in the framework of electromagnetic theory by Maxwell. It is easy to imagine that recent technological developments would have been impossible without the development of optics.

1.2 Nanophotonics

The development of nano-fabrication technologies made us possible to manipulate the light by the artificially fabricated thin plane device. The hundred-nanometer sized patterns are fabricated on the thin dielectric plane. When the light impinges on the pattern, its behavior changes. Using this patterned plane device, light can be controlled. As the advantage, the size of the device is quite small compared to the conventional bulky devices made of glasses. The research field is called nanophotonics. Although it cannot be completely distinguished, this field is roughly divided into three categories; photonic crystals [2], metasurfaces [3] and surface plasmon photonics (plasmonics) [4].

The photonic crystal is the artificial structure made by periodically arranged with dielectric structures on the period whose scale is comparable to the wavelength of the light. Figure 1.1 (a) shows the schematic of the photonic crystal slab, the hole is drilled in the dielectric membrane on the constant period. The hole is filled with the dielectric whose dielectric constant is different from that used for the membrane. Because of the periodicity, the (photonic) band gap is formed similar to the solid crystals. This means the light in a certain frequency band cannot propagate inside the photonic crystal. The concept of the photonic crystal was first proposed by Yablonovich [5] in the late 1980s.

As the application, photonic crystal waveguide is proposed. By eliminating the holes in certain positions, light can be guided along where there is no hole as shown in Fig. 1.1 (b).

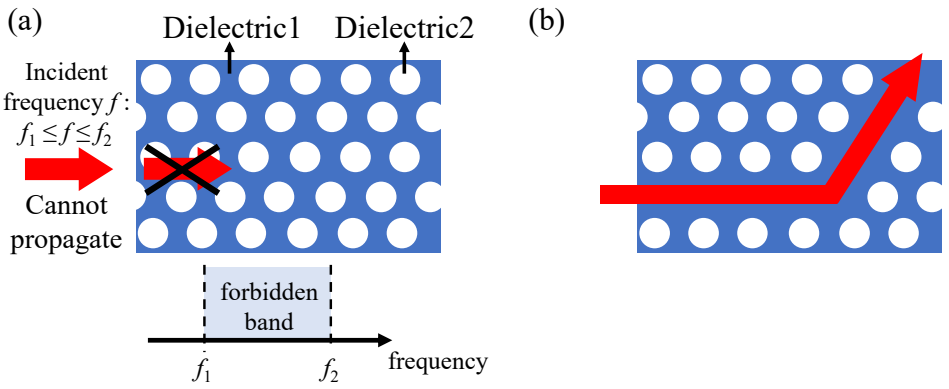

Figure 1.1: (a) Schematic of the photonic crystal slab structure. Circular holes in which the dielectric2 is filled are arranged on the periodic constant on the planar membrane with dielectric1. Similar to the solid crystals, forbidden band is formed for the light impinging on the structure. Light whose frequency lies inside the forbidden band cannot propagate in the structure. (b) Schematic of the photonic crystal waveguide. Consider removing the holes of certain positions so that there is a path in the periodic hole array as shown in (b). In this case, the light with frequency in the forbidden band can be guided along the path.

In addition, the field of metasurface has grown significantly from its theoretical proposal in 2011 [3]. The metasurface is the subwavelength array composed of a unit cell of the meta-atoms. Each meta-atoms are made of metal or dielectric materials. Figure 1.2 (a) schematically shows an example of the patch structure which is used in the metasurface. In each unit cell, geometrical parameters of individual rectangle patches are gradually varied. Therefore, the impinging light takes different responses according to the different in-plane position, and eventually, the propagation direction of light changes. This deflection is called anomalous refraction. The most popularly investigated application is meta-lens as shown in Fig. 1.2 (b). By properly arranging the meta-atoms, the impinging parallel light can be concentrated at one point. Thus, the compact lens is realized, which is called meta-lens [6]. In addition to the compactness, meta-lens can ease the chromatic aberration which is an unavoidable problem in the bulky glass lenses.

Plasmonics is another subject of growing interest. Plasmonic crystals were made by the metal in contrast to the dielectric structure on photonic crystals. Figure 1.3 is the illustration of a cylindrical plasmonic structure. This is only one of the examples, and various types of geometries are used. In addition, coupling to the surface plasmon was indicated by the dispersion relation. By the diffraction from the array, the incident light

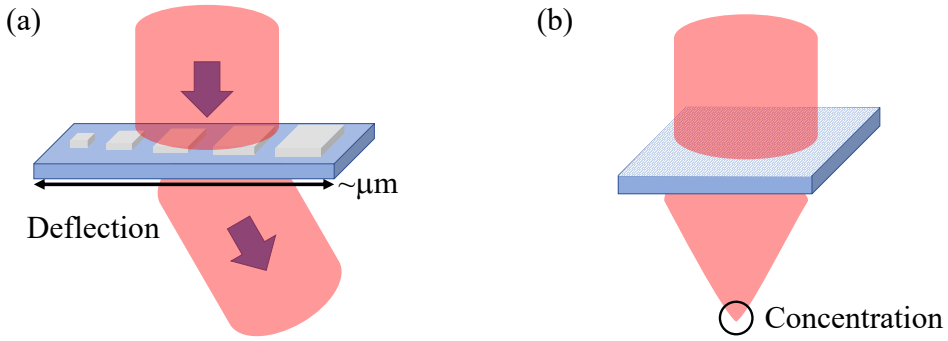

Figure 1.2: (a) Example of patch structure meta atom unit cell. In the unit atom, geometrical parameters of rectangular patches are gradually varied. Therefore, impinging light is diffracted in a certain direction. (b) Example of the metasurface application. By properly arranging the meta atom cells, light can be concentrated at one focal point, which enables the very thin compact lense.

can couple to the surface plasmons. A few applications were displayed. One of the most advantageous point of the plasmonic crystal is its ability to concentrate light beyond the diffraction limit, which realizes the very compact optical devices. The sensitivity of the surface plasmon to the surrounding environment can be used for sensors. Besides, various applications such as filters, cancer treatment and improving the efficiency of solar cells are expected.

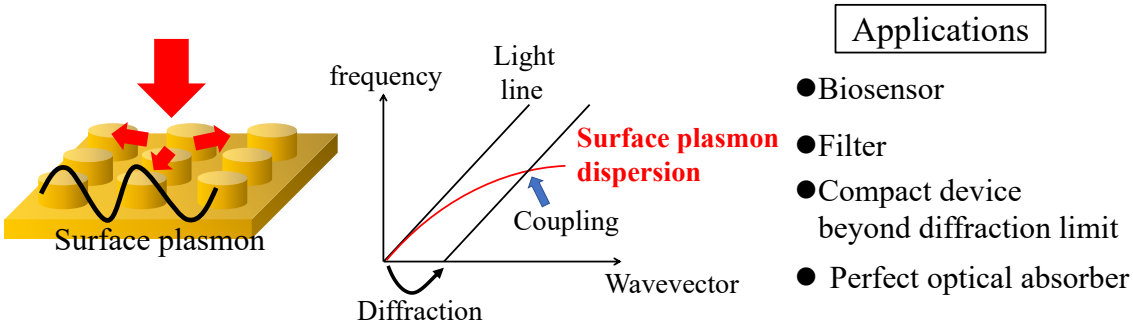

Figure 1.3: Cylindrical array plasmonic structure (left). The dispersion relation indicates the coupling to surface plasmon by the diffraction from array. A few applications were displayed.

As a recent trend in nanophotonics, phenomena such as extraordinary transmission (EOT) [7], bound states in the continuum (BICs) [8] and exceptional point (EP) [9] are

studied intensively in order to realize novel applications to optical devices.

The first one, EOT was reported in 1998 by Ebbesen et al. They reported the strong transmission of light through the subwavelength hole array drilled on the metal membrane. This phenomenon was greatly drawn attention since such an enhanced transmission was contrary to the classical diffraction theory, which states that the light cannot be concentrated beyond the diffraction limit [10]. After the theoretical investigation, it was revealed that the surface plasmon was involved in the EOT. The discovery greatly accelerated the study of the plasmonics.

BIC was reported in 2008 [11] in photonics. However, its concept was firstly proposed in 1929 [12] in quantum mechanics. If a physical system has the radiation port of the energy, the resonant state on the system decays as time evolves. In contrast to such a state, the BIC is purely localized and does not decay. Using the BIC, the confinement of light on the nanostructure is greatly improved. Therefore the BIC is recently gaining popularity.

The EP was also discussed in the quantum mechanics at first, and then it is discussed in the photonics. In the theoretical aspect, the study of EP contributes to the development of the study of the non-Hermitian system. In addition, some applications such as unidirectional reflectionless is proposed. Unidirectional reflectionless can be applied to prevent the reflection wave propagating into the laser cavity, which hinders the stable operation of the laser.

1.3 Study on the metal grating

In this work, we focus on the metal grating. Although the EOT was found very recently as described above, similar phenomena were reported in metal grating over 100 years ago. First of all, let me describe the history of the study on the optical response of the metal grating. Fraunhofer was the first one to study the grating. Since then, the spectral analysis using the grating began.

One remarkable finding occurred at the beginning of the 20th century. In 1902, Wood found the anomalous bright or dark bands in the spectra of the reflected wave from the metal grating [13], which could not have been explained by the existed theories. This peculiar behavior is widely known as Wood's anomaly. After Wood's report, a lot of theoretical studies to explain the optical properties of the metal grating have been conducted. The early theoretical work was provided by Rayleigh [14] in 1907. Rayleigh discovered that the anomalies are seen near the wavelength where the radiative or non-radiative state of the particular diffraction order switches. Because of the Rayleigh's report, the anomaly is also called Rayleigh anomaly. After that, Fano attributed to the anomalies to the excitation of a surface wave on the grating in 1941 [15]. Hessel and Oliner explained anomalies using the guided wave of the grating in 1965 [16]. From the late 1900s, some reported the involvement of the surface plasmon resonance to the anomalies [17]. Despite these thorough works, sufficient physical interpretations for the anomalies were yet to be present at that time.

Corresponding to the discovery of EOT phenomenon on two-dimensional metal hole array, the study for metal grating was further accelerated since the EOT like resonant transmission behavior was also observed in the transmission type metal gratings. The cross-sectional view of the ordinary transmission type metal grating is shown in Fig. 1.4(a). In contrast to the reflection type grating, light can be transmitted through the slits and diffraction occurs for the transmitted waves. In the early 2000s, many scientists have worked on to analyze the series of peculiar behaviors. One of the difficulties for the interpretation of the anomalies is that it is hard to distinguish what kind of particular physical factor is involved. In transmission type grating, anomalies are often observed as the dip of the transmission spectrum (0 transmission) or enhanced transmission. These spectrum structures lie very close to each other in the spectrum bands. Fig. 1.4(b) shows the schematic illustration of typically seen spectrum. In the 0th order transmission spectrum, asymmetric spectrum profile (dip and peak) will show up. Moreover, they often lie at the wavelength of surface plasmon resonance on flat metal. Therefore, at least in the 2000s, there were many interpretations to attribute the excitation of surface plasmon to the enhanced transmission [18] or attribute the surface plasmon to 0 (inhibited) transmission [19]. In fact, it is gradually becoming apparent that such as anomalous dip or peak in transmission spectra was caused by the interference of several factors. In 2014, Yoon et al [20] explained the series of dip and peak in transmission spectra as the Fano interference of two types of different transmission. In this way, the various theoretical works to elucidate the origin of anomalies have been provided in these 100 years, and became almost clear.

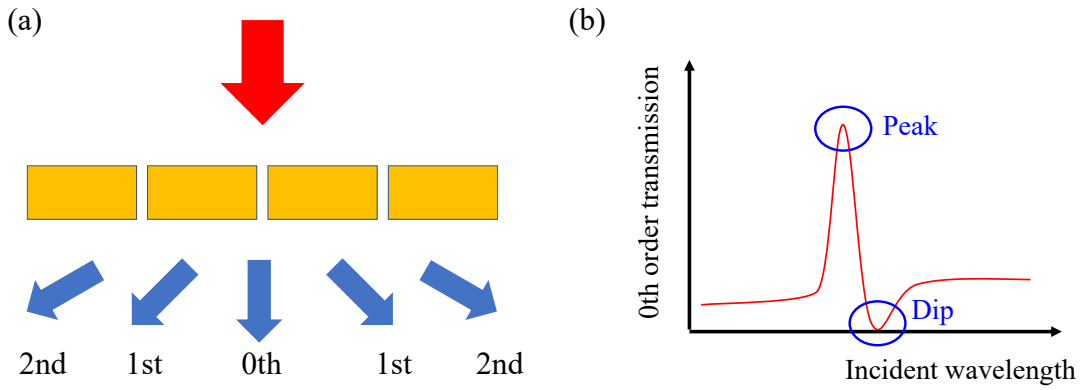

Figure 1.4: (a) Cross sectional view of the transmission type metal grating. (b) Typically observed schematics of 0th order transmission spectrum through transmission type metal grating. Transmission dip and peak appears and these spectrum structures often lies near the wavelength where radiative or non-radiative state of the particular diffraction order switches.

1.4 Purpose of this work

The purpose of this work is to analyze the peculiar optical responses of the metal grating. This work is important for the theoretical and practical aspects.

In the theoretical aspect, the metal grating is very convenient for the theoretical study. Despite its geometrical simplicity, metal grating exhibits most of the peculiar phenomena which are observed in other nanophotonic structures. Since the geometry of the metal grating is very simple, it can be described by relatively simple electromagnetic frameworks such as a mode expansion method. In addition, the polarization can be separated completely in two orthogonal modes. These facts make it easier to analyze the phenomena, which makes it possible to understand the physics of those important phenomena.

In the practical aspect, metal grating is frequently and ordinarily used in various applications. For example, spectroscopy, waveguide couplers and plasmon sensors. In those devices, we might want to avoid some of the phenomena because such phenomena are sometimes unfavorable for the operation of the devices. If the mechanism of the peculiar phenomena was understood clearly, we can predict whether the particular phenomena appear on certain structure parameters and how such phenomena can be avoided.

In this work, the numerical electromagnetic field analysis method was used for analysis.

1.5 Structure of the thesis

The main contents are divided into 6 chapters.

In Chapter 1, we have introduced the background and purpose of this study.

In Chapter 2, method of analysis used in this study is explained.

In Chapter 3, we analyzed the optical properties of single metal grating and the influence of surrounding environmental effect (the presence of substrate). In the structure, the anomalous phenomena are seen near the wavelength where the radiative state of the diffraction order changes. Based on the bound mode of the system, we analyzed the peculiar behavior observed in the transmission or electric field enhancement spectra.

In Chapter 4, we analyzed the more complicated grating system; metal grating placed on the dielectric waveguide, which corresponds to the grating coupler device. In the structure, the presence of bound states in the continuum (BIC) is confirmed. We discuss the polarization effect for the emergence of the BIC. For analysis, the theoretical model; temporal coupled-mode theory (TCMT) was used.

In Chapter 5, we also discuss the same system as in Chapter 4 and BIC. But in this chapter, we discuss the effect of the parameter change for the BIC. In addition, another observed phenomenon is also discussed.

Finally, in chapter 6, overall summary and future perspective of this work is described as a conclusion.

Chapter 2

Method of analysis

Spatial coupled mode theory (SCMT) [21, 35] was used for the electromagnetic field analysis in this study. The expression for three and four layers system are described in section 2.1 and 2.2, respectively. The P-polarization case is considered.

In addition, temporal coupled mode theory (TCMT) was used as theoretical model, which is described in section 2.3.

2.1 Spatial coupled mode theory for three layers system

In SCMT with three layers system as shown in Fig. 2.1 the fields above (region I) and below (region III) the grating are expanded into the plane and evanescent waves of the diffraction order n, having the in-plane wavenumber $k_x = k_0 + 2\pi n/\Lambda$, where k_0 is the in-plane wavenumber of the incident wave. In the slit, the field is expanded into the slit mode with propagating (for propagating mode) or attenuating (for cut-off mode) constant q_β. β indicates the index of the slit mode. The fields are connected by the boundary conditions between the regions using the surface impedance $Z_S = \epsilon_m^{-1/2} Z_0$ at the metal surface [23], where Z_0 is the vacuum impedance. The amplitudes A_β and B_β of the slit mode β propagating or attenuating in the $+z$ and $-z$ directions, respectively, are obtained by the equations

$$\sum_\beta \left(G^-_{\mathrm{I},\alpha\beta} A_\beta + G^+_{\mathrm{I},\alpha\beta} B_\beta \right) = \frac{2}{f^+_{k_x=k_0(\mathrm{I})}} Y_{k_x=k_0(\mathrm{I})} S_{k_x=k'_0,\alpha}, \tag{2.1}$$

$$\sum_\beta \left(G^+_{\mathrm{III},\alpha\beta} A_\beta e^{iq_\beta h} + G^-_{\mathrm{III},\alpha\beta} B_\beta e^{-iq_\beta h} \right) = 0, \tag{2.2}$$

where

$$G^\pm_{(\mathrm{I,III}),\alpha\beta} = \sum_{k_x} \frac{Y_{k_x(\mathrm{I,III})}}{f^+_{k_x(\mathrm{I,III})}} S^*_{k_x,\alpha} S_{k_x,\beta} (1 \pm Z_s Y_{\mathrm{eff},\beta}) \mp Y_{\mathrm{slit},\alpha\beta}, \tag{2.3}$$

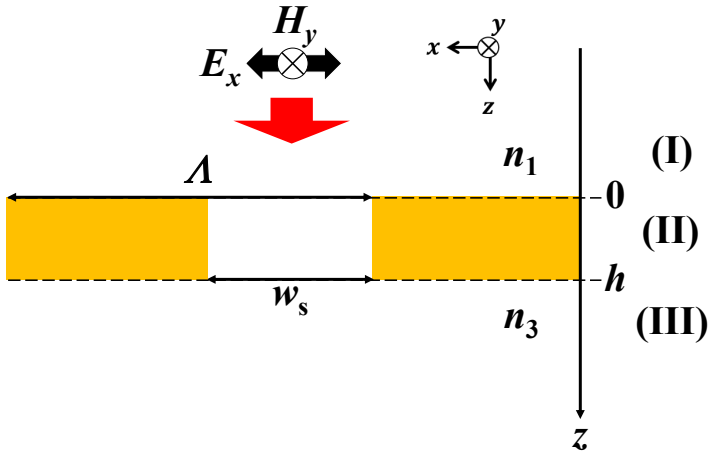

Figure 2.1: Cross sectional view of 3 layers system with periodic grating.

$$
\begin{aligned}
f^{\pm}_{k_x(\mathrm{I,III})} &= 1 \pm Z_S Y_{k_x(\mathrm{I,III})}, \\
Y_{k_x(\mathrm{I,III})} &= \frac{\epsilon_{1,3}}{Z_0}\frac{k_\omega}{k_z}, \\
k_z^2 &= \epsilon_{1,3} k_\omega^2 - |k_x|^2,
\end{aligned}
\tag{2.4}
$$

with $\epsilon_1 = n_1^2$ and $\epsilon_3 = n_3^2$ being the dielectric constants in regions I and III, respectively.

$$
S_{k_x,\alpha} = \int_\Lambda E^*_{x,k_x}(x) E_{x,\mathrm{slit}(\alpha)}(x) dx \tag{2.5}
$$

denotes the overlap integral between the electric fields $E_{x,\mathrm{slit}(\alpha)}(x)$ of the slit mode with mode index α and $E_{x,k_x}(x)$ of the in-plane wavenumber k_x in the dielectric region. Here the asterisk means the complex conjugate. The admittance of the slit mode $Y_{\mathrm{slit},\alpha\beta}$ and the effective admittance $Y_{\mathrm{eff},\alpha}$ in the mean field approximation [21] are given, respectively, by

$$
Y_{\mathrm{slit},\alpha\beta} = \frac{\int_\Lambda E^*_{x,\mathrm{slit}(\alpha)}(x) H_{y,\mathrm{slit}(\beta)}(x) dx}{\int_\Lambda E^*_{x,\mathrm{slit}(\alpha)}(x) E_{x,\mathrm{slit}(\beta)}(x) dx} \tag{2.6}
$$

and

$$
Y_{\mathrm{eff},\alpha} = \frac{\int_\Lambda E^*_{x,k_0}(x) H_{y,\mathrm{slit}(\alpha)}(x) dx}{S_{k_0,\alpha}}. \tag{2.7}
$$

In chapter 3, the explanation of the phenomena was proceeded based on the SCMT with single slit mode approximation of the electromagnetic field inside the slit, which is valid for very narrow slit case. Here the expression of the single mode approximated SCMT is described.

For the fields and the (complex) propagation constant q in the slit, we solved numerically the transcendental equation derived from the boundary conditions for the transverse-magnetic (TM) modes in the metal–insulator–metal waveguide, taking into account the field penetration into the metal of ϵ_m. This mode is a propagating one, having the x component of the electric field $E_{x,slit}$ and y component of the magnetic field $H_{y,slit}$ symmetric in x with respect to the slit center and corresponding to the transverse electromagnetic (TEM) mode in the perfect electric conductor (PEC) approximation ($\epsilon_m \to \infty$). Under the single mode approximation, Eq. 2.1 and 2.2 can be written as

$$G_{\mathrm{I}}^{-}A + G_{\mathrm{I}}^{+}B = \frac{2}{f^{+}_{k_x=k_0(\mathrm{I})}} Y_{k_x=k_0(\mathrm{I})} S_{k_x=k'_0} \tag{2.8}$$

$$G_{\mathrm{III}}^{+}Ae^{iqh} + G_{\mathrm{III}}^{-}Be^{-iqh} = 0, \tag{2.9}$$

where we defined $G^{\pm}_{(\mathrm{I,III}),00} \equiv G^{\pm}_{(\mathrm{I,III})}$, $A_0 \equiv A$, $B_0 \equiv B$, $S_{k_x=k'_0,0} \equiv S_{k_x=k'_0}$, $q_0 \equiv q$.

Using the solutions A and B, the 0th order transmittance can be calculated as

$$T_0 = \left| \frac{Ae^{iqh}(1 + Z_S Y_{\mathrm{eff}}) + Be^{-iqh}(1 - Z_S Y_{\mathrm{eff}})}{f^{+}_{k_0(\mathrm{III})}} S_{k_0} \right|^2 . \tag{2.10}$$

2.2 Spatial coupled mode theory for four layers system

In the four layers system as shown in Fig. 2.2, the fields above (region I) and below (region III and IV) the grating are expanded into the plane and evanescent waves of the diffraction order n, having the in-plane wavenumber $k_x = k_0 + 2\pi n/\Lambda$, where k_0 is the in-plane wavenumber of the incident wave. In the slit, the field is expanded into the slit mode with propagating (for propagating mode) or attenuating (for cut-off mode) constant q_β. β indicates the index of the slit mode. The amplitudes A_β and B_β of the slit mode propagating or attenuating in the $+z$ and $-z$ directions, respectively, are obtained by the equations

$$\sum_{\beta} \left(G^{-}_{\mathrm{I},\alpha\beta} A_\beta + G^{+}_{\mathrm{I},\alpha\beta} B_\beta \right) = \frac{2}{f^{+}_{k_x=k_0(\mathrm{I})}} Y_{k_x=k_0(\mathrm{I})} S_{k_x=k'_0,\alpha}, \tag{2.11}$$

$$\sum_{\beta} \left(G^{+}_{\mathrm{IV},\alpha\beta} A_\beta e^{iq_\beta h_1} + G^{-}_{\mathrm{IV},\alpha\beta} B_\beta e^{-iq_\beta h_1} \right) = 0, \tag{2.12}$$

where

$$G^{\pm}_{\mathrm{I},\alpha\beta} = \sum_{k_x} \frac{Y_{k_x\mathrm{I}}}{f^{+}_{k_x\mathrm{I}}} (S_{k_x,\alpha})^* S_{k_x,\beta} (1 \pm Z_s Y_{\mathrm{eff}}) \mp Y_{\mathrm{slit},\alpha\beta}, \tag{2.13}$$

$$G^{+}_{\mathrm{IV},\alpha\beta} = \sum_{k_x} Y_{k_x\mathrm{III}} \frac{f^{-}_{k_x\mathrm{III-IV}}}{f^{+}_{k_x\mathrm{III-IV}}} (S_{k_x,\alpha})^{*} S_{k_x,\beta}(1 + Z_s Y_{\mathrm{eff}}) - Y_{\mathrm{slit},\alpha\beta}, \tag{2.14}$$

$$f^{+}_{k_x\mathrm{III-IV}} = f^{+}_{k_x\mathrm{III}} \frac{Y_{k_x(\mathrm{III})} + Y_{k_x(\mathrm{IV})}}{2Y_{k_x(\mathrm{III})}} e^{-ik_{z3}(h_2-h_1)} + f^{-}_{k_x\mathrm{III}} \frac{Y_{k_x(\mathrm{III})} - Y_{k_x(\mathrm{IV})}}{2Y_{k_x(\mathrm{III})}} e^{ik_{z3}(h_2-h_1)}, \tag{2.15}$$

$$f^{-}_{k_x\mathrm{III-IV}} = \frac{Y_{k_x(\mathrm{III})} + Y_{k_x(\mathrm{IV})}}{2Y_{k_x(\mathrm{III})}} e^{-ik_{z3}(h_2-h_1)} - \frac{Y_{k_x(\mathrm{III})} - Y_{k_x(\mathrm{IV})}}{2Y_{k_x(\mathrm{III})}} e^{ik_{z3}(h_2-h_1)}. \tag{2.16}$$

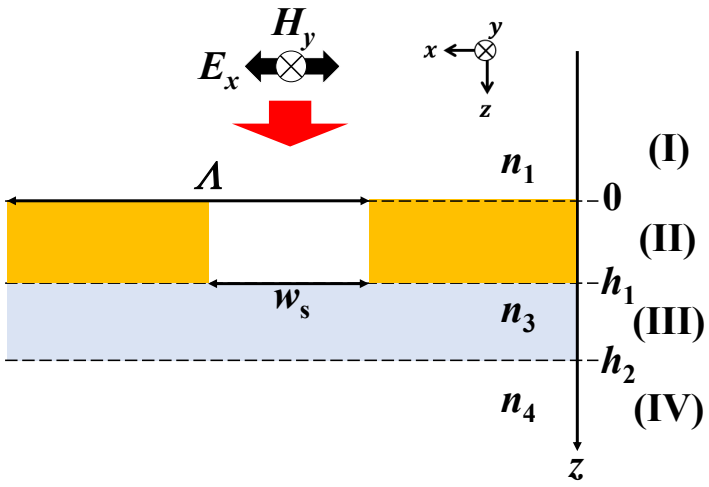

Figure 2.2: Cross sectional view of 4 layers system with periodic grating.

2.3 Temporal coupled mode theory

2.3.1 Two modes and one port system

Temporal coupled mode theory (TCMT) describes the behavior of resonances in a system in the time domain. Since the two resonant modes are involved in this study as described in chapter 4 and 5, expression for the two resonant modes and one port system with a near field coupling and a far (radiation) field coupling was provided here as follows. The time evolution of the two mode amplitude $\mathbf{a}^{\mathrm{T}} = (a_1, a_2)$ can be described by an effective Hamiltonian $\tilde{\mathbf{H}}$ and input wave s_+ with a coupling coefficient vector $\mathbf{D} = (d_1, d_2)$ as

$$\frac{d}{dt}\mathbf{a} = -i\tilde{\mathbf{H}}\mathbf{a} + \mathbf{D}^{\mathrm{T}} s_+ = -i\{\mathbf{\Omega} - i(\mathbf{\Gamma}_i + \mathbf{\Gamma}_e)\}\mathbf{a} + \mathbf{D}^{\mathrm{T}} s_+, \tag{2.17}$$

where

$$\mathbf{\Omega} = \begin{pmatrix} \omega_1 & \alpha \\ \alpha & \omega_2 \end{pmatrix}, \mathbf{\Gamma}_e = \begin{pmatrix} \gamma_{e1} & \gamma_0 \\ \gamma_0^* & \gamma_{e2} \end{pmatrix}, \mathbf{\Gamma}_i = \begin{pmatrix} \gamma_{i1} & 0 \\ 0 & \gamma_{i2} \end{pmatrix}$$

with $\omega_{1,2}, \gamma_{i1,2}$ and $\gamma_{e1,2}$ denoting the eigenfrequency, the internal loss, and the external loss of mode 1 or 2, respectively, and $d_{1,2}$ denoting the coupling between the external radiation and modes 1 and 2 through the port. The off-diagonal terms α in $\mathbf{\Omega}$ and γ_0 in $\mathbf{\Gamma}_e$ represent the near- and far-field coupling, respectively. Here, α is set to be real assuming that the effect of material loss on α is negligible, and that the system without material loss has time-reversal symmetry [24]. Considering the principle of the conservation of energy, the outgoing wave s_- can be written as

$$s_- = c_a s_+ + \mathbf{Da} \tag{2.18}$$

with c_a representing the direct scattering coefficient.

From time-reversal symmetry and the energy conservation principle, the following relations are derived [25]:

$$\mathbf{D}^\dagger \mathbf{D} = 2\mathbf{\Gamma}_e, \tag{2.19}$$

$$c_a \mathbf{D}^* = -\mathbf{D}. \tag{2.20}$$

Using these relations, $\mathbf{D}$ and γ_0 can be rewritten. First, expressing $\mathbf{D}$ as

$$\mathbf{D} = (|d_1|e^{i\varphi_1}, |d_2|e^{i\varphi_2}) \tag{2.21}$$

and applying Eq. 2.19, following relations

$$|d_1| = \sqrt{2\gamma_{e1}}, \tag{2.22}$$

$$|d_2| = \sqrt{2\gamma_{e2}}, \tag{2.23}$$

$$e^{i(-\varphi_1+\varphi_2)} = \frac{\gamma_0}{\sqrt{\gamma_{e1}\gamma_{e2}}} \tag{2.24}$$

are derived. From Eq. 2.20,

$$c_a = -e^{i2\varphi_1}, \tag{2.25}$$

$$c_a = -e^{i2\varphi_2} \tag{2.26}$$

are derived. Subtracting each side of Eq. 2.26 from Eq. 2.25, then

$$e^{i2\varphi_1} = e^{i2\varphi_2}. \tag{2.27}$$

Thus,

$$\varphi_2 = \varphi_1 + m\pi. \tag{2.28}$$

From Eq. 2.24 and Eq. 2.28,

$$\gamma_0 = \pm\sqrt{\gamma_{e1}\gamma_{e2}} \equiv p\sqrt{\gamma_{e1}\gamma_{e2}}. \tag{2.29}$$

Finally, $\mathbf{D}$ can be written as

$$\mathbf{D} = e^{i\varphi_d}(\sqrt{2\gamma_{e1}}, p\sqrt{2\gamma_{e2}}). \tag{2.30}$$

where φ_d is an arbitrary phase and p is a parity (± 1) that represents the phase difference between d_1 and d_2. Here $p = 1$ for the in-phase ($|\varphi_1 - \varphi_2| = 0$) case, and $p = -1$ for the anti-phase ($|\varphi_1 - \varphi_2| = \pi$) case. Hereafter, the phase φ_d is set to zero. This is always possible by adjusting the reference position for the external radiation.

2.3.2 Derivation of the reflection coefficient

The reflection coefficients for the incident wave with angular-frequency ω can be derived in TCMT as follows.

Consider a case that $\mathbf{a}$ is time harmonic, $\mathbf{a} \propto e^{-i\omega t}$. Eq. 2.17 is written as

$$[i(\mathbf{\Omega} - \omega\mathbf{I}) + \mathbf{\Gamma}_i + \mathbf{\Gamma}_e)]\mathbf{a} = \mathbf{D}^T s_+. \tag{2.31}$$

Taking the inverse matrix from the left side of Eq. 2.31,

$$\mathbf{a} = [i(\mathbf{\Omega} - \omega\mathbf{I}) + \mathbf{\Gamma}_i + \mathbf{\Gamma}_e)]^{-1}\mathbf{D}^{\mathrm{T}} s_+. \tag{2.32}$$

Substitute this into Eq. 2.18,

$$r(\omega) \equiv \frac{s_-}{s_+} = c_a + \mathbf{D}[i(\mathbf{\Omega} - \omega\mathbf{I}) + \mathbf{\Gamma}_i + \mathbf{\Gamma}_e)]^{-1}\mathbf{D}^{\mathrm{T}}. \tag{2.33}$$

Under the condition of Eq. 2.19 and Eq. 2.20, inverse matrix is

$$[i(\mathbf{\Omega} - \omega\mathbf{I}) + \mathbf{\Gamma}_i + \mathbf{\Gamma}_e)]^{-1} = \frac{\begin{pmatrix} i(\omega_2 - \omega) + \gamma_{i2} + \gamma_{e2} & -i\alpha - p\sqrt{\gamma_{e1}\gamma_{e2}} \\ -i\alpha - p\sqrt{\gamma_{e1}\gamma_{e2}} & i(\omega_1 - \omega) + \gamma_{i1} + \gamma_{e1} \end{pmatrix}}{\{(\omega_1 - \omega) - i(\gamma_{i1} + \gamma_{e1})\}\{(\omega_2 - \omega) - i(\gamma_{i2} + \gamma_{e2})\} + (i\alpha + p\sqrt{\gamma_{e1}\gamma_{e2}})^2}. \tag{2.34}$$

After the matrix calculation on the RHS of Eq. 2.34, we finally get $r(\omega)$ as

$$r(\omega) = c_a\Bigg[1 + 2\frac{\gamma_{e1}\{i(\omega_2 - \omega) + \gamma_{i2}\} + \gamma_{e2}\{i(\omega_1 - \omega) + \gamma_{i1}\} - i2p\alpha\sqrt{\gamma_{e1}\gamma_{e2}}}{\{(\omega_1 - \omega) - i(\gamma_{i1} + \gamma_{e1})\}\{(\omega_2 - \omega) - i(\gamma_{i2} + \gamma_{e2})\} + (i\alpha + p\sqrt{\gamma_{e1}\gamma_{e2}})^2}\Bigg]. \tag{2.35}$$

2.3.3 Derivation of the amplitudes of modes

The amplitudes of each mode can be obtained from Eq. 2.32 as

$$a_1 = \frac{\{i(\omega - \omega_2) - (\gamma_{i2} + \gamma_{e2})\}\sqrt{2\gamma_{e1}} + (p\sqrt{\gamma_{e1}\gamma_{e2}} + i\alpha)p\sqrt{2\gamma_{e2}}}{\{\omega - \omega_1 + i(\gamma_{i1} + \gamma_{e1})\}\{\omega - \omega_2 + i(\gamma_{i2} + \gamma_{e2})\} - (ip\sqrt{\gamma_{e1}\gamma_{e2}} - \alpha)^2} s_+, \tag{2.36}$$

$$a_2 = \frac{\{i(\omega-\omega_1)-(\gamma_{i1}+\gamma_{e1})\}p\sqrt{2\gamma_{e2}}+(p\sqrt{\gamma_{e1}\gamma_{e2}}+i\alpha)\sqrt{2\gamma_{e1}}}{\{\omega-\omega_1+i(\gamma_{i1}+\gamma_{e1})\}\{\omega-\omega_2+i(\gamma_{i2}+\gamma_{e2})\}-(ip\sqrt{\gamma_{e1}\gamma_{e2}}-\alpha)^2}s_+. \quad (2.37)$$

If $|\omega-\omega_1|$ and $|\omega-\omega_2|$ are much larger than the loss and the coupling coefficients, the amplitudes are approximated by

$$a_1 \simeq \frac{i\sqrt{2\gamma_{e1}}}{\omega-\omega_1}s_+, \quad (2.38)$$

$$a_2 \simeq p\frac{i\sqrt{2\gamma_{e2}}}{\omega-\omega_2}s_+. \quad (2.39)$$

Thus, the phase difference between a_1 and a_2 is determined by p in the region far from resonances where the signs of $\omega-\omega_1$ and $\omega-\omega_2$ are the same.

Chapter 3

Substrate effect on the anomalies of transmission in the metal grating

3.1 Previous study on the optical properties of metal grating

As described in the introduction that although metal gratings are a very fundamental element in optics, a sufficiently complete explanation of their optical response is not easy. In addition to the onset (or passing-off) of a diffraction order, the surface plasmon (SP) [19, 20, 26–38], Fabry– Perot (FP) (or cavity plasmon) [19, 20, 26–31, 33–38], and the Fano resonances [20, 33–35, 38–40] and their interplay make the relevant spectra extremely complicated with anomalous peaks and dips near the wavelength given by the grating formula [41], $\lambda_R = n\Lambda(-\sin\theta \pm 1)/j$, where Λ, n, and θ are the period of the grating, the refractive index of the medium, and the angle of the light incidence, respectively, and $j = \pm 1, \pm 2, \pm 3, \ldots$. Historically, the anomalous structures have been called Wood's or Wood–Rayleigh anomalies [42] and have also been discussed recently in terms of extraordinary optical transmission [7]. In this paper, we call the wavelength λ_R the Rayleigh wavelength for simplicity.

For the grating with a relatively narrow slit, which can be treated as a single-mode waveguide, the 0th order transmission can be written by a FP formula [19, 20, 28, 29, 32–35],

$$T_0 = \left| \frac{\tau_1 \tau_3}{1 - \rho_1 \rho_3 e^{2iqh}} \right|^2 \tag{3.1}$$

where ρ_1 and ρ_3 (τ_1 and τ_3) are the reflection (transmission) coefficients for the slit mode at the incident- and the exit side interfaces, respectively, as illustrated in Fig. 3.1, q is the propagation constant of the slit mode, and h is the grating thickness. Hence, T_0 takes its peaks at the Fabry–Perot (FP) resonances, i.e., the minima in the denominator, neglecting the variation of $|\tau_1 \tau_3|$. The effect of SP at each interface is involved in $\rho_1 \rho_3, \tau_1$, and τ_3. Here, it is important to distinguish the SP at the

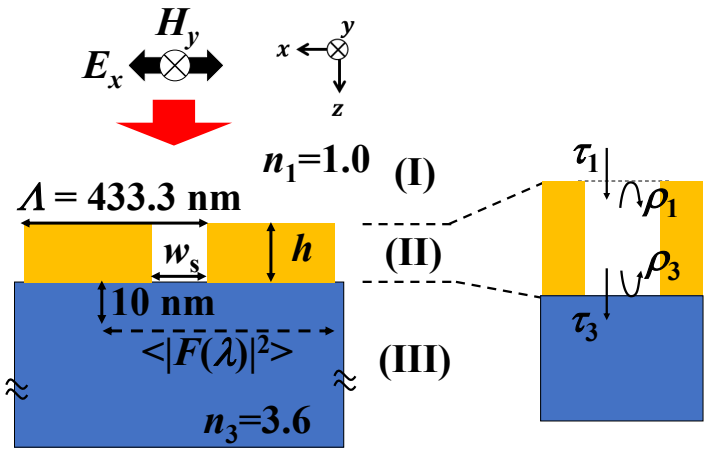

Figure 3.1: Schematic drawing of the structure investigated in this work (left) and the illustration for $\tau's$ and $\rho's$ in Eq. 3.1 (right).

metal–dielectric interfaces with a finite slit width from that at the flat metal–dielectric interface (SPF) [32,33]. It is known [19,20,28,29] that $\tau_{1,3}$, and hence T_0 becomes nearly zero around $\lambda_{SPF} = \Lambda\{\epsilon_m\epsilon_{1,3}/(\epsilon_m+\epsilon_{1,3})\}^{1/2}$, where Λ is the period of the grating and ϵ_m and $\epsilon_{1,3}$ are the permittivity of the metal and of each dielectric medium, respectively. On the other hand, the SP resonance λ_{SP} depends also on the slit width [33]. In particular, for wide slits, the SP resonance disappears (sitting in the region $< \lambda_R$ with a large damping) [33]. Recently, Yoon *et al.* successfully explained the roles of the SP in the transmission spectra of metal gratings by focusing on the case of $\lambda_R < \lambda_{SP} < \lambda_{SPF}$ [20]. In particular, they showed that $\tau's \sim 0$ around λ_{SPF} is understood as the Fano resonance caused by the interference between the wave transmitted from the slit to the free space directly and that by way of the SP at the interface.

Most of the previous reports including [20], however, have dealt with a case where the grating is placed in air (i.e., the dielectric constant below and above the grating is the same). From an application point of view, it is important to consider the grating, or metal apertures in general, on a dielectric substrate. For example, metal gratings on a semiconductor have been shown to improve the performance of optoelectronic devices such as photodiodes [43, 44] and photoconductive switches for terahertz emitters/detectors [45–50]. Metal gratings on a substrate is also an important structure for the perfect (or very high) optical absorption (POA) [51, 52]. Hence, for the design of various devices, it is important to clarify how the presence of the substrate affects the optical response of the grating. Though some reports have commented on the effect of the substrate [26, 31, 34–37, 39], no clear and concrete discussions were given, except for the reports on POA investigating the role of the modes in the substrate [51, 52]. In addition, for the photoconductive switches, it is important to enhance the field near

the grating in the substrate [47], which has not been investigated well.

In this work, we investigated the transmission T_0 and the near-field enhancement E around λ_R in the metal gratings on a semiconductor substrate. We considered rather thin gratings, which are preferred because of easy fabrication. By using a spatial coupled mode theory (SCMT), we can derive approximate analytical expression for, for example, ρ_1 and ρ_3, giving clear physical pictures. It will be shown that, for telecom and longer wavelengths, the peaks in the T_0 and E spectra are pinned at λ_R in the thin gratings and the peak vanishes with decreasing grating thickness. To elucidate the physics behind the phenomena, we analyzed the bound mode (BM) of the system, which corresponds to the FP resonance in narrow slit cases and gives the peaks in T_0 and E. With the decrease of the grating thickness, the BM disappears, which causes the pinning and the vanishing of the peaks. The disappearance of the BM is a feature of the grating on a semiconductor substrate, where the dielectric ambient sandwiching the grating is highly asymmetric, contrary to the grating in the air where the BM is usually present. The essential difference between the symmetric and asymmetric structures comes into the BM in the total reflection phase $\arg(\rho_1\rho_3)$. We also show that the plasmonic band gap is large at the grating–semiconductor interface, enhancing the disappearance of the BM.

3.2 Method and results

3.2.1 Analyzed structure and calculation methods

The structure studied in this work is illustrated in Fig. 3.1. The Au grating with a period $\Lambda = 433.3$ nm, thickness h, and slit width w_s sits on a substrate with a refractive index $n_3 = 3.6$. The period corresponds to the Rayleigh wavelength in the substrate at $\lambda_R = 1560$ nm for normal incidence. For comparison, we also show the results for $n_3 = 1.0$ with $\Lambda = 1560$ nm. The regions above the grating and inside the slit are assumed to be air. Hence, for $n_3 = 3.6$, the dielectric ambient above and below the grating is highly asymmetric, while it is symmetric for $n_3 = 1.0$. In the following, w_s is chosen to be 43.3 nm ($= 0.1\Lambda$ for $n_3 = 3.6$), unless otherwise stated. The permittivity (ϵ_m of Au is modeled by a Drude–Lorentz fit to the Johnson– Christy data [53]. At 1560 nm, ϵ_m is about $-125 + i11.5$. In this paper, we discuss the 0th order transmission (T_0) and the near-field enhancement (E) for a p-polarized plane wave of wavelength λ (wavenumber k_ω) incident from the air side. Although the near-field enhancement could be characterized in various ways, in this work we chose E defined as the ratio of the spatially averaged squared electric field amplitude $|F(\lambda)|^2$ on a plane 10 nm below the interface with and without the grating. This definition is directly related to the enhancement of the photo excitation in the devices [43–50]. Though the magnitude of E calculated in such a way depends on the distance from the metal (10 nm in the present definition) and hence has no definite meaning, the spectral feature and its parameter dependence are important for the device design.

For the calculation of T_0 (0th order transmission), E (electric field enhancement) and other related quantities, we used a SCMT [21] which was described in Chapter 2.

The BM of the system is obtained in SCMT as the nontrivial solution of coupled Eqs. 2.8 and 2.9 without light incidence,

$$G^-_{(\mathrm{I})}G^-_{(\mathrm{III})}e^{-iqh} - G^+_{(\mathrm{I})}G^+_{(\mathrm{III})}e^{iqh} = 0, \tag{3.2}$$

with respect to a complex frequency f_{BM} with a negative imaginary part $\mathrm{Im}[f_{\mathrm{BM}}]$. In this work, the solution was searched for $|\mathrm{Im}[f_{\mathrm{BM}}]|/\mathrm{Re}[f_{\mathrm{BM}}] < 0.3$. The enhancement E is maximized at the BM frequency $\mathrm{Re}[f_{\mathrm{BM}}]$ (wavelength $\lambda_{\mathrm{BM}} = c/\mathrm{Re}[f_{\mathrm{BM}}]$, with c the speed of light in vacuum), since the system is resonantly excited, neglecting the shift due to $\mathrm{Im}[f_{\mathrm{BM}}]$. The reflection coefficients for the slit mode at the slit–dielectric interfaces can be calculated from

$$\rho_1 = \frac{A}{B} = -\frac{G^+_{(\mathrm{I})}}{G^-_{(\mathrm{I})}}, \rho_3 = \frac{B}{A} = -\frac{G^+_{(\mathrm{III})}}{G^-_{(\mathrm{III})}}. \tag{3.3}$$

Using the reflection coefficients, we can rewrite the BM condition Eq. 3.2 as

$$1 - \rho_1\rho_3 e^{2iqh} = 0, \tag{3.4}$$

which is simply the condition for the FP resonance. Hence, as far as the BM exists, the peak in T_0 can be also said to appear at λ_{BM} (with a finite deviation due to $\mathrm{Im}[f_{\mathrm{BM}}]$ and the wavelength dependence of $|\tau_1\tau_3|$).

For $\mathrm{Im}[f_{\mathrm{BM}}] < 0$, the propagation constant q can have a negative imaginary part and the solutions of Eq. 3.4 expressed by

$$\ln(|\rho_1||\rho_3|) - 2h\mathrm{Im}\{q\} + i\{\arg(\rho_1\rho_3) + 2h\mathrm{Re}\{q\} - 2m\pi\} = 0 \tag{3.5}$$

are labeled by an integer m. We can also calculate the bound modes at the grating–substrate interface (BMI), which corresponds to the SP resonance in complex frequency domain, as the nontrivial solution of Eq. 2.9 with no incidence ($A = 0$); i.e.,

$$G^-_{\mathrm{III}} = 0. \tag{3.6}$$

3.2.2 Transmission and enhancement spectra and bound mode

The E and T_0 spectra of the grating on the substrate ($n_3 = 3.6$) are shown in Figs. 3.2 (a) and 3.2 (b), respectively, for various h. To confirm the validity of the SCMT calculation, the results obtained by rigorous coupled wave analysis (RCWA) [21] are also plotted by the dashed lines. The SCMT results are in good agreement with RCWA, particularly in the position of the peaks in the long (> 1500 nm) wavelength range, which is a main issue in the following discussions. In the E spectra for $\lambda > \lambda_R$, the peak red shifts with the increase of h for $h \geq 300$ nm, following the shift of the BM wavelength λ_{BM} indicated by the filled triangles. Qualitatively, such h dependence is a

general feature of FP resonance. For $h \leq 200$ nm, however, the BM disappears and the peak is pinned at $\lambda_{\rm R}$. This is the main subject of this paper and discussed in detail in the next section. The same behavior is seen in the T_0 spectra, except for $h = 300$ nm, where a dip appears instead of a peak. In this case, $\lambda_{\rm BM}$ is close to $\lambda_{\rm SPF}$. One can see that T_0 is nearly 0 around $\lambda_{\rm SPF}$ for all values of h. Hence, the dip (and $T_0 \sim 0$ for all h) is ascribed to the Fano resonance causing $\tau_3 \sim 0$ [see Eq. 3.1]. Though not shown here, $\tau_3 \sim 0$ around $\lambda_{\rm SPF}$ was confirmed by the SCMT calculation.

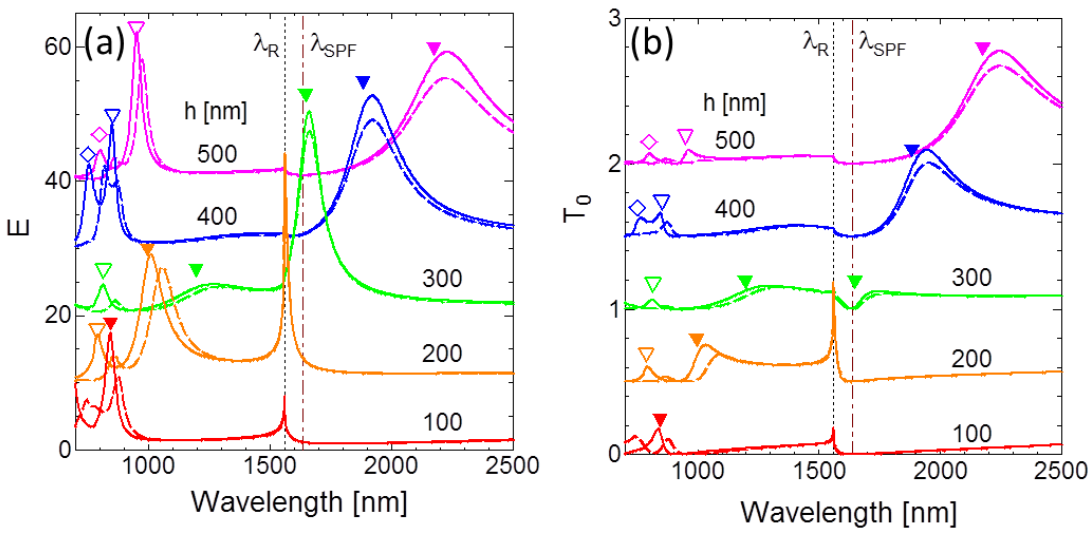

Figure 3.2: Calculated (a) E and (b) T_0 spectra for $n_3 = 3.6$ and $w_s = 43.3$ nm ($= 0.1\Lambda$) for several values of h. The solid and dashed lines are the results by SCMT and RCWA, respectively. The spectra were vertically shifted by a step of 10 in (a) and of 0.5 in (b) for visual clarity. The dotted and dash–dotted lines indicate the position of $\lambda_{\rm R}$ and $\lambda_{\rm SPF}$, respectively. The filled and open triangles indicate the position of $\lambda_{\rm BM}$ of $m = 1$ and $m = 2$, respectively, calculated using the imaginary part of Eq. 3.5. Here, the BMs with same m exist at two wavelengths ($m = 2$ for $h = 400$ and 500 nm, and $m = 1$ for $h = 300$ nm). This occurs because the larger q (shorter λ) is compensated by the smaller $\arg(\rho_1\rho_3)$, for the pair of the wavelengths, one shorter and the other longer than the singular wavelength ($\lambda_{\rm R}$ or λ giving $\arg(\rho_3) = 2\pi$), as will be seen in Fig. 3.6. Physically, it corresponds to the splitting of the FP resonance by the coupling to the SP mode (anticrossing) via the steep variation of ρ's [20], as mentioned in Section 3.1.

Here, we comment on the pinning of the peaks in T_0 and E at $\lambda_{\rm R}$ seen in Fig. 3.2 for the case where BM disappears ($h \leq 200$ nm). From the h dependence of the BM position, the disappearing BM can be thought to lie in the region $\lambda < \lambda_{\rm R}$. In such cases, the BM becomes overdamped due to the coupling to the radiative 1st order diffraction. As a result, as schematically illustrated in Fig. 3.3, the main part of the virtual resonance is shaved off in $\lambda < \lambda_{\rm R}$, leaving the tail in $\lambda > \lambda_{\rm R}$ with a peak at $\lambda_{\rm R}$. This model also explains the decrease of the peak height in E and T_0 at $\lambda_{\rm R}$ with the

decrease of h from 200 nm to 100 nm in Fig. 3.2, since the virtual resonance may get away from λ_{R} with decreasing h.

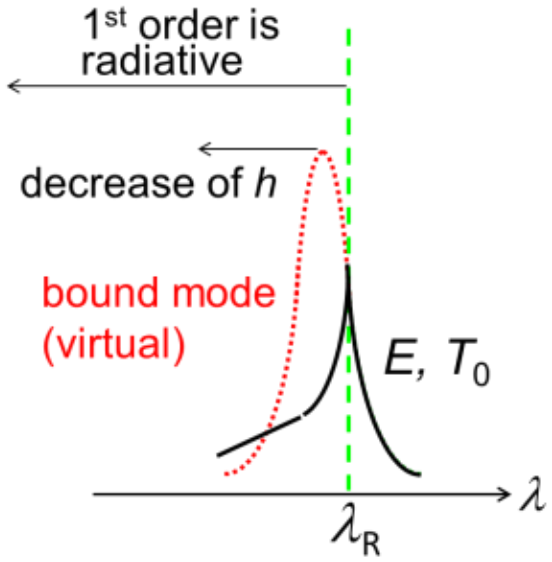

Figure 3.3: Schematic illustration explaining the reason for the pinning of the peaks at λ_{R} when the overdamped BM sits in the radiative range, $\lambda < \lambda_{\mathrm{R}}$.

Next, let us show the results for the case of $n_3 = 1.0$ (grating in air) and $\Lambda = 1560$ nm. Shown in Fig. 3.4 are the (a) E and (b) T_0 spectra around λ_{R} (1560 nm) together with λ_{BM}'s (triangles) for various h. Here, the same w_s(= 43.3 nm) as that for Fig. 3.2 was chosen to keep the slit mode similar. As in Fig. 3.2, the peak positions in the SCMT results (solid lines) are in good agreement with the RCWA results (dashed lines). One can clearly see that the lowest order ($m = 1$) BM indicated by the filled triangles blue shifts with the decrease of h, qualitatively as a feature of FP resonance. Following the shift of the BM, the peaks in E and T_0 blue shift with the decrease of h, though the Fano resonance suppresses the peaks when λ_{BM} gets closer to λ_{SPF}. Here, a significant difference from Fig. 3.2 ($n_3 = 3.6$) can be noticed. The lowest order BM does not disappear even for a small h. Correspondingly, the pinning of the peaks at λ_{R} does not occur.

To see more clearly the difference between the two cases of $n_3 = 3.6$ and $n_3 = 1.0$ in the behavior of the BM, we plotted λ_{BM} as functions of h in Fig. 3.5 (red dots). In the case of $n_3 = 3.6$, the lowest-order BM intersects with $\lambda_{\mathrm{R}} = 1560$ nm at a finite h, as discussed above. In contrast, in the case of $n_3 = 1.0$, the lowest-order BM does not cross λ_{R}, but approaches a wavelength longer than λ_{R} in the limit of $h \to 0$, as seen in Fig. 3.4.

Before discussing the reason for the different behavior in the BM between the two cases, we comment here on the effect of the Fano resonance on E. As can be clearly seen in the case of $h = 300$ nm in Fig. 3.2(a), the Fano resonance does not affect the E spectra in the grating on the substrate. This can be explained as follows. In the case

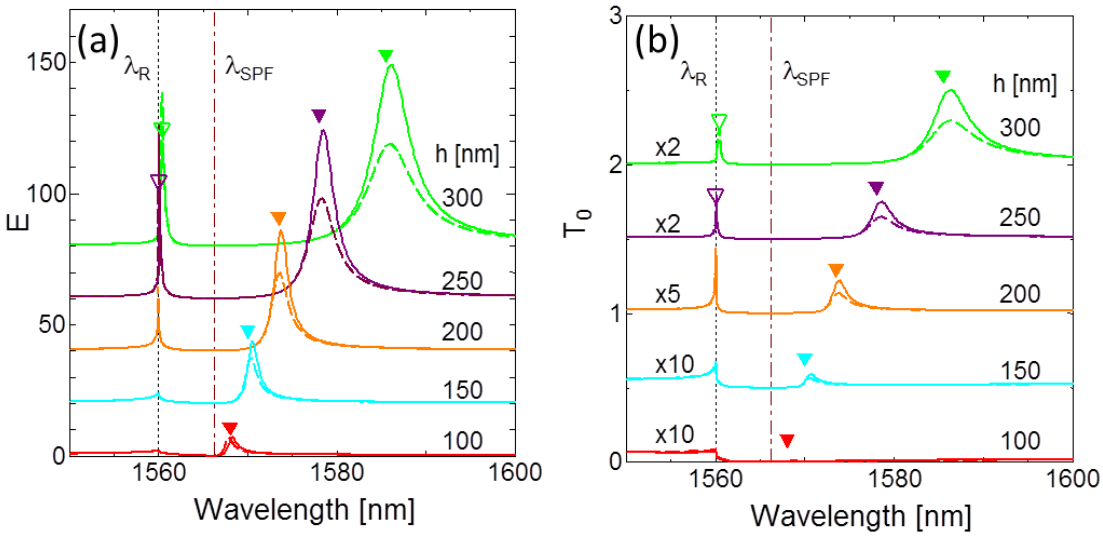

Figure 3.4: Calculated (a) E and (b) T_0 spectra for $n_3 = 1.0$, $\Lambda = 1560$ nm, and $w_s = 43.3$ nm for several values of h. The solid and dashed lines are the results by SCMT and RCWA, respectively. The dotted and dash–dotted lines indicate the position of λ_{R} and λ_{SPF}, respectively. The filled and open triangles indicate the position of λ_{BM} of $m = 1$ and $m = 2$, respectively, calculated using the imaginary part of Eq. 3.5. The spectra were vertically shifted by a step of 20 in (a) and of 0.5 in (b) for visual clarity.

of $n_3 \neq n_1$, λ_{SPF}'s are different between the incident and exit (substrate) sides. Hence, around the λ_{SPF} of the exit side, the Fano resonance occurs in the exit side ($\tau_3 \sim 0$) but not in the incident side ($\tau_1 \neq 0$). In such a case, the slit mode can be excited. On the other hand, as mentioned before, the Fano resonance in the grating is an interference occurring in the far field between the waves directly transmitted from the slit and that through the SP [20]. In other words, the excited slit mode is associated with the SP wave at the exit-side interface, which contributes to the near-field enhancement, even for $\tau_3 \sim 0$. On the contrary, as seen in Fig. 3.4 (a), E is suppressed around λ_{SPF} in the grating in air ($n_1 = n_3$). This is because $\tau_1 (= \tau_3)$ becomes also nearly zero and hence the slit mode is not excited. Therefore, we can say that the survival of the E peak at λ_{SPF} of the substrate-side interface is another feature of the gratings on a substrate, or more generally of gratings in asymmetric ambient.

3.3 Discussions

3.3.1 Reflection phase and bound mode

We discuss first the absence/presence of the BM in terms of the reflection phase for the slit mode. For the wavelength $\lambda > \lambda_{\mathrm{R}}$, where only the 0th order diffraction is radiative, moduli of the reflection coefficients $|\rho_1|$ and $|\rho_3|$ are not small. In such cases, the lowest-

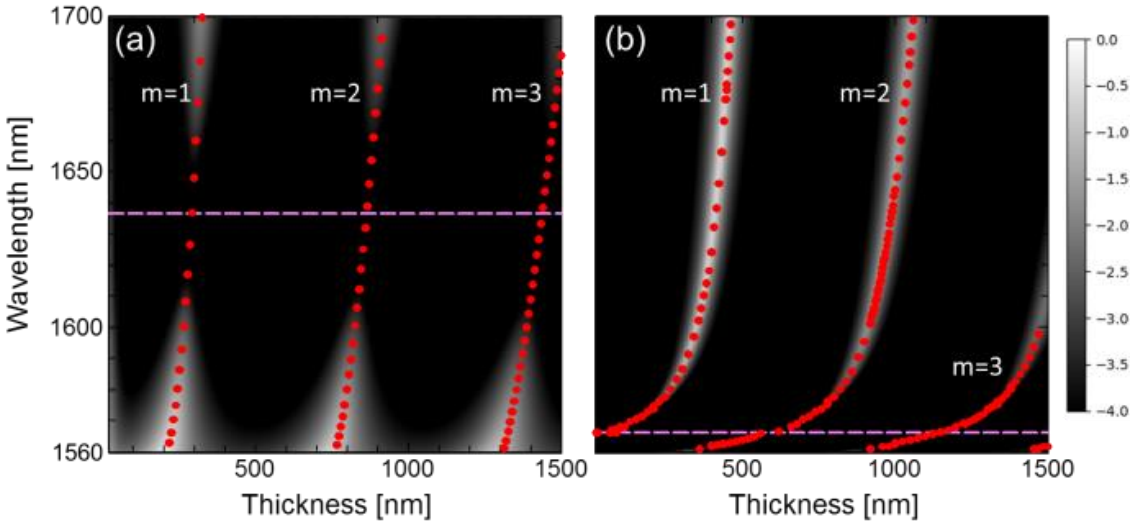

Figure 3.5: Red circles depict the h dependence of $\lambda_{\rm BM}$ for the case of (a) $n_3 = 3.6$ and (b) $n_3 = 1.0$, both with $w_s = 43.3$ nm. For comparison, Log(T_0) is also shown by the gray-scale map. The dashed lines indicate the position of $\lambda_{\rm SPF}$.

order BM is given approximately by the phase condition (imaginary part) of Eq. 3.5 with $m = 1$ and hence the presence of BM in the limit of $h \to 0$ can be discussed in terms of $\arg(\rho_1\rho_3) = 2\pi$. In the highly asymmetric case ($n_3 >> n_1$), assuming $\arg(\rho_1) = 0$ for simplicity, $\arg(\rho_1) = 2\pi$ is necessary for the BM to exist. In the symmetric structure, in contrast, $\arg(\rho_1\rho_3) = \arg(\rho_3^2) = 2\pi$ is realized with $\arg(\rho_3) = \pi$. Therefore, it is important to know the range of $\arg(\rho_3)$. It has been shown numerically that, starting with 0 at large λ, $\arg(\rho_3)$ increases to π at λ_R with decreasing λ in the case of $\epsilon_m \to \infty$ (PEC approximation) [28]. In the case of $\epsilon_m = -5, \arg(\rho_3)$ has been shown to reach a little in excess of 2π at $\lambda_{\rm R}$ [20].

In the SCMT, by considering only the 0th order diffraction $G^{\pm}_{\rm (I,III)}$ and neglecting the metal loss, we can obtain an analytic expression for $\arg(\rho_3)$ as

$$\arg(\rho_3) = \pi + 2\tan^{-1} b, \tag{3.7}$$

where

$$b = \frac{1}{\sqrt{|\epsilon_m|}} \frac{Z_0 Y_{\rm eff}}{S^2} \left[\frac{Y_{\rm slit}}{Y_{\rm eff}} - S^2 \right] - \frac{Z_0 Y_{\rm slit}}{S^2} \frac{\sqrt{k_x^2 - n_3^2 k_\omega^2}}{n_3^2 k_\omega}. \tag{3.8}$$

Here, we also neglected the k_x dependence of S_{kx}, and wrote $|S_{kx}|^2 = S^2$, where S^2 can be estimated roughly to be w_s/Λ. Equation 3.8 indicates that, with decreasing k_ω (increasing λ) from k_x/n_3 (light line, $\lambda = \lambda_{\rm R}$ at $k_x = 2\pi/\Lambda$ corresponding to normal incidence), b and hence $\arg(\rho_3)$ decrease monotonically, neglecting the variation of $Y_{\rm slit}/Y_{\rm eff}$, with a maximum value

$$b_{\rm max} = \frac{1}{\sqrt{|\epsilon_m|}} \frac{Z_0 Y_{\rm eff}}{S^2} \left[\frac{Y_{\rm slit}}{Y_{\rm eff}} - S^2 \right] \tag{3.9}$$

at $k_\omega = k_x/n_3(\lambda = \lambda_R)$. Hence, $\arg(\rho_3) = 2\pi$ is not realized for $\lambda > \lambda_R$. Note also that the PEC approximation ($\epsilon_m \to \infty$) gives $b_{\max} \to 0$ and $\mathrm{Max}[\arg(\rho_3)] \to \pi$, consistent with [28].

In practice, the effects from other diffraction orders can modify $\arg(\rho_3)$. Figure 3.6 (a) shows $\arg(\rho_3)$s obtained using Eq. 3.3 with diffraction orders up to 20th for the case of $n_3 = 3.6$ with various w_s. In the case of $w_s = 0.1\Lambda$ (the case of Fig. 3.2, $\arg(\rho_3)$ is much smaller than 2π. Even with the finite value of $\arg(\rho_1)$ (dashed line) taken into account, $\arg(\rho_1\rho_3) = 2\pi$ is not realized, explaining the disappearance of the BM for small h in Fig. 3.2. One can also see that, with the extremely narrow slit, $w_s = 0.01\Lambda = 4.33$ nm, $\arg(\rho_3)$ slightly exceeds 2π.

On the other hand, for a visible wavelength where $|\epsilon_m|$ is small and hence $b_{\max}$ is large, we can expect to find a wavelength realizing $\arg(\rho_3) = 2\pi$ with a more practical w_s. As an example, $\arg(\rho_3)$s in the grating designed for $\lambda_R = 780$ nm are shown in Fig. 3.6(b). One can see that $\arg(\rho_3) = 2\pi$ is realized in the range of $\lambda > \lambda_{\mathrm{R}}$ with $w_s = 43.3$ nm, so that the BM is expected to exist even for $h \to 0$.

The reflection phase $\arg(\rho_3)(= \arg(\rho_1))$ for the case of $n_3 = 1.0$ (grating in air) with $w_s = 43.3$ nm is shown in Fig. 3.6 (c). In this symmetric structure, the condition for the BM to exist for $h \to 0$ is $\arg(\rho_3) = \pi$. This condition is obviously realized in $\lambda > \lambda_{\mathrm{R}}$, consistently with Figs. 3.4 and 3.5(b). Interestingly, Eqs. 3.7 and 3.9 predict that, if $Y_{\mathrm{slit}}/Y_{\mathrm{eff}} > S^2$ is satisfied, $b_{\max}$ is positive and $\mathrm{Max}[\arg(\rho_3)] > \pi$. Hence,a wavelength giving $\arg(\rho_3) = \pi$ always exists, which guarantees the presence of the BM, in the range of $\lambda > \lambda_{\mathrm{R}}$ in the grating in symmetric ambient. Though it cannot be shown analytically, for the slit mode considered here, $Y_{\mathrm{slit}}/Y_{\mathrm{eff}} > S^2$ is satisfied for a very wide range of w_s and $|\epsilon_m|$. The case where the condition is not satisfied could be a wide slit where S^2 is large. To check the validity of the prediction, we performed a numerical survey for $\arg(\rho_3)$ using Eq. 3.3 with diffraction orders up to 20th. An example is shown in Fig. 3.6(d) for $w_s = 468$ nm$(= 0.3\Lambda)$. It can be confirmed that $\arg(\rho_3) = \pi$ is realized for a wide range (-5 to $-10,000$) of ϵ_m. For such a large w_s and large $|\epsilon_m|$, the SP resonance at the interface does not exist in the range of $\lambda > \lambda_{\mathrm{R}}$ [33]. Hence, we can conclude that the presence of the BM is essentially an intrinsic feature in symmetric structures, irrespective of the presence of the SP resonance.

Here, let us briefly comment on the analytic expression for the BM. With the same simplification as for Eq. 3.7, the lowest-order BM can be obtained from Eq. 3.4 to be

$$k_x = n_3 k_\omega \sqrt{1 + F^2}, \tag{3.10}$$

where

$$F = \frac{n_3}{Z_0 Y_{\mathrm{slit}}} S^2 \{b_{\max} - \cot(qh)\} \tag{3.11}$$

or

$$F = \frac{n_3 (= n_1)}{Z_0 Y_{\mathrm{slit}}} S^2 \{b_{\max} + \tan(qh/2)\} \tag{3.12}$$

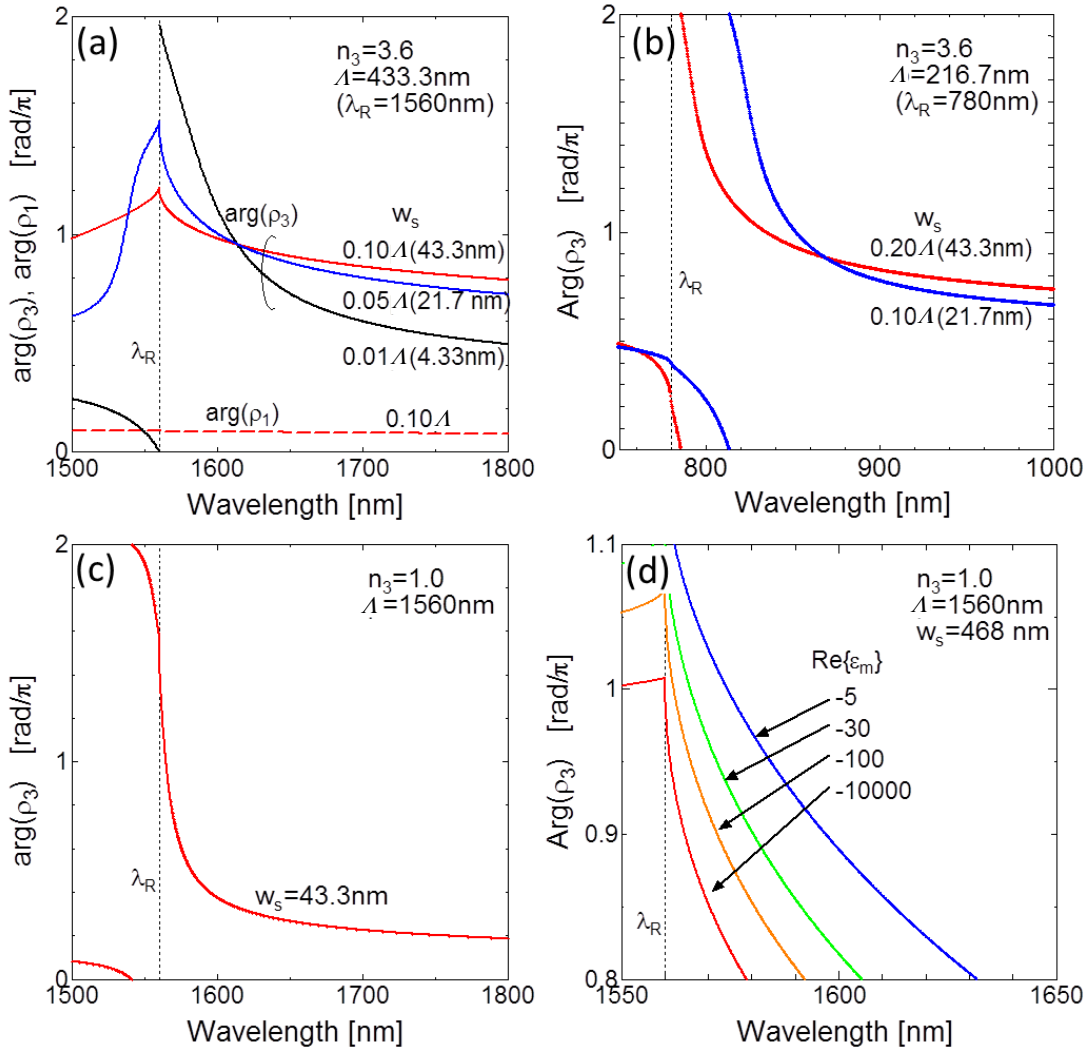

Figure 3.6: Wavelength dependence of the reflection phase $\arg(\rho_3)$ in the substrate side. (a) $n_3 = 3.6$ with various w_s (solid lines). $\mathrm{Arg}(\rho_1)$ for $w_s = 0.1\Lambda$ (dashed line) is also shown. (b) $n_3 = 3.6$ designed for $\lambda_R = 780$ nm. (c) $n_3 = 1.0$ with $w_s = 43.3$ nm. (d) $n_3 = 1.0$ with $w_s = 468$ nm for various ϵ_m. The black dotted lines indicate the position of λ_R.

for the asymmetric and symmetric structures, respectively. For the asymmetric case, $\rho_1 = 1$ was assumed for simplicity. A finite value of $\arg(\rho_1)$ can be included as an additional phase to qh. Here $b_{\max} > 0$ can be assumed, as shown above. The condition $F > 0$ corresponding to $\lambda > \lambda_{\mathrm{R}}$ is not satisfied for $h \to 0$ in the asymmetric case, while it is always satisfied in the symmetric case. The expressions 3.10–3.12 show explicitly that the asymmetry strongly affects the presence of the BM through the reflection phase $\arg(\rho_1\rho_3)$.

3.3.2 Effect of band gap

The dispersion of BM gives us a further insight into the origin of its disappearance in the asymmetric case. Figure 3.7(a) shows λ_{BM} (red line) and T_0 (gray scale) as functions of the in-plane wavenumber k_x for the case of $n_3 = 3.6$ and $h = 100$ nm. One can see that the BM disappears when λ_{BM} seeks to cross the light line of the corresponding diffraction order. An important point here is that the BM in the longer wavelength (lower) branch bends near $k_x = 0$, suggesting that the disappearing shorter wavelength (upper) branch near $k_x = 0$ also bends. The bending is due to the band gap caused by the mixing between the crossing diffraction orders. Therefore, in addition to the nature of the asymmetric structure discussed above, the mixing-induced band gap enhances the disappearance of the BM in the upper branch. It is obvious that the band gap observed here is predominantly related to the SP in the grating–substrate interface, since the light line in the air-side and the geometrical FP resonance are far away from this range. As is seen in the T_0 spectra (gray scale map), the peak along the lower branch is not visible for small k_x , because the slit mode is not excited well due to the mismatch between the slit mode and the incident wave in the in-plane symmetry.

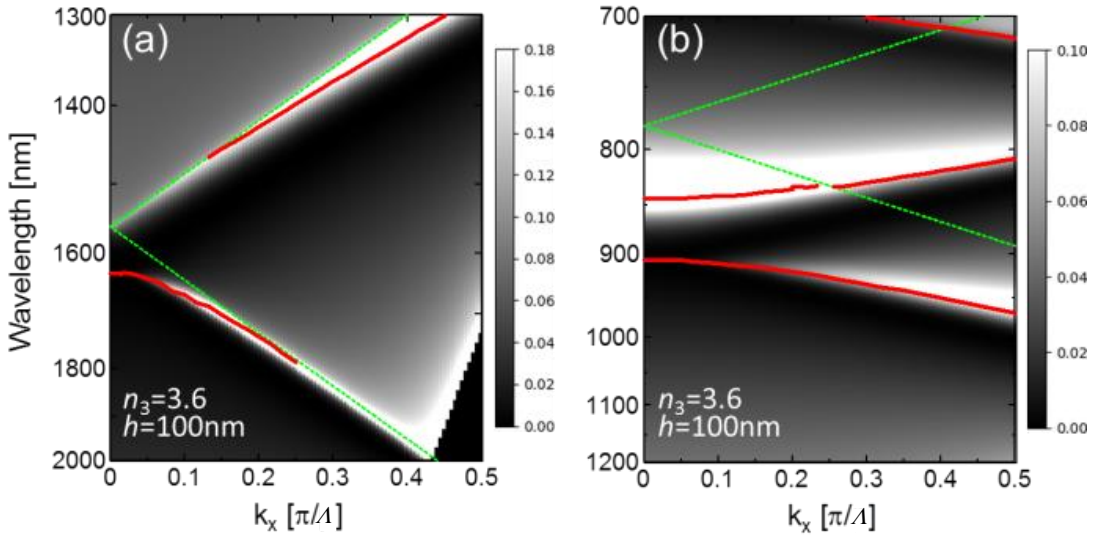

Figure 3.7: BM wavelength λ_{BM} (red line) and the T_0 spectra (gray-scale map) as functions of k_x for $n_3 = 3.6$ and $h = 100$ nm around the (a) 1st and (b) 2nd order λ_{R}. The green dotted lines indicate the light line.

Before discussing the band gap in the SP at the substrate side interface, we comment on the peaks in T_0 and E around 780 nm; i.e., the 2nd order λ_{R} seen in Fig. 3.2. Shown in Fig. 3.7(b) are λ_{BM} (red line) and T_0 (gray scale) as functions of k_x for the short wavelength range. For the case of $h = 100$ nm shown here, the BM does not disappear ($\lambda_{\mathrm{BM}} >$ 2nd order λ_{R}) because $|\epsilon_m|$ is small ($\sim$ 25 at 780 nm). The correspondence between the peak in T_0 (and E, though not shown here) and the BM can be confirmed, manifesting that the peaks in T_0 and E can be explained (with the effect in T_0 by the

Fano resonance of the corresponding diffraction order) by the excitation of the BM in the whole spectral range. Note that the band gap in the BM is clearly observed. In addition, there is a tiny, but a finite, jump in the BM when it crossed the light line ($k_x \sim 0.25\pi/\Lambda$), which comes also from the SP of the interface, as discussed below.

To confirm the band gap and the jump in the BM at the crossing with the light line observed above originate from the SP at the grating–substrate interface, we calculated the dispersion of the BMI, of which the real part λ_{BMI} corresponds to the SP resonance, at the interface using Eq. 3.6. The results for $n_3 = 3.6$ with several values of w_s are shown in Fig. 3.8(a). For $w_s = 0.1\Lambda$, the upper branch disappears when it seeks to become shorter than the light line. Therefore, in this case, SP resonance does not exist for normal incidence in the range of $\lambda > \lambda_{\mathrm{R}}$. In the case of $w_s = 0.01\Lambda = 4.33$ nm, though the upper branch exists at $k_x = 0$, a large splitting of the BMI is observed. In addition, a jump in the BMI at the crossing with the light line, as seen Fig. 3.7(b), is clearly observed. Therefore, the band gap in the BM shown in Fig. 3.7 is concluded to be caused by that in the SP (through ρ_3) at the grating-substrate interface. Though the physical interpretation of the jump in the BMI at the crossing with the light line is not clear at present, it is obvious numerically to be due to the change in the character (radiative or evanescent) of the diffraction order across the light line. We should stress that the appearance of the jump is confirmed not to be the artifact in the SCMT, since it is also observed in the RCWA calculation.

For comparison, the BMI in the case of $n_3 = 1.0$ with $w_s = 43.3$ nm is shown in Fig. 3.8(b). Though the band gap at $k_x \sim 0$ is present, it is very small. In addition, the jump in the BMI at the crossing with the light line is also very small. Therefore, we can conclude that the opening of the band gap, including the effect of the jump in the BMI, widens the parameter range of the BM to disappear in the gratings on a high-index substrate.

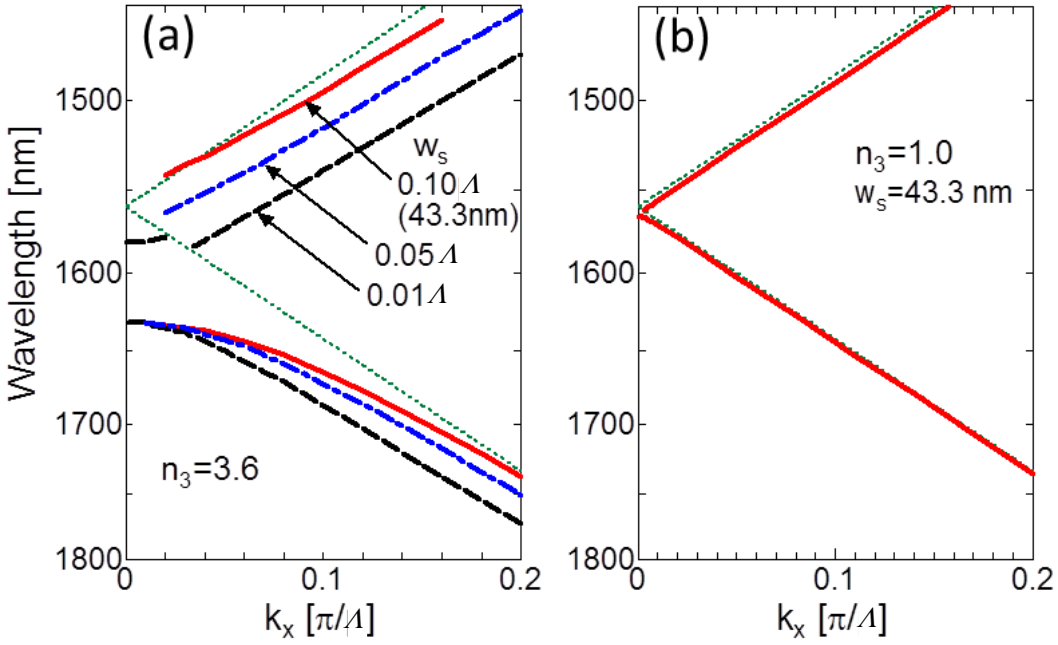

Figure 3.8: In-plane dispersion of λ_{BMI} at the substrate-side interface for (a) $n_3 = 3.6$ with $w_s = 0.10\Lambda(43.3\text{ nm})$, 0.05Λ and 0.01Λ and (b) $n_3 = 1.0$ with $w_s = 43.3$ nm.

3.4 Observation position dependence of enhancement in the substrate region

So far, enhancement was evaluated by averaging the electric fields 10 nm below the grating (in the substrate region) over one period in in-plane direction. However, the enhancement under the slit is sometimes important for some application such as improving the efficiency of the photo conductive antenna. Therefore, the enhancement was evaluated only under the slit. As a result, as will be shown below, a peculiar dark band (zero enhancement) which was not seen in the averaged enhancement was observed. The presence of dark band is critical problem for the practical application using enhancement. In this section, the mechanism of the dark band under the slit is analyzed.

3.4.1 Spectra of transmittance and enhancement

Figure 3.9 shows the gray scale mappings of T_0 and enhancement (under the slit E_{slit} and under the metal E_{metal}) of incident wavelength vs metal thickness. Several features are seen.

1) There are several bright lines in both enhancement and transmittance scale in Fig. 3.9. As described in the preceding section, bright lines correspond to the BMs. The red shift of the bright lines is explained by the correspondence of the BMs to the condition for the FP resonance (Eq. 3.4), which shifts linearly in varying thickness.

2) Even in the case that the slit ratio is low, transmittance is relatively high ($\max(T_0) > 0.8$ for $w_s = 0.1\Lambda$). Since, as mentioned above, the enhanced transmittance (bright lines in Fig. 3.9) originated from the FP resonance, such an enhanced transmission is not peculiar. This enhanced transmission is in other words, the extraordinary transmission. On the other hand, the enhancement is higher for the case of lower slit ratio ($w_s = 0.1\Lambda$). In the present case, the transmittance is high for the low slit ratio, and the energy is concentrated in the narrow slit. Therefore, the enhancement is high for the narrow slit.

3) Transmittance becomes 0 at λ_{SPF}, which came from the Fano resonance on the metal-dielectric interface.

4) The similar dark band appears at the wavelength slightly longer than λ_{R} for the enhancement under the slit E_{slit}. The dip caused by the Fano resonance occurs in the far field. Therefore, no such a dip occurs for the near field which corresponds to the enhancement. Indeed, no dark band appears for the enhancement under the metal E_{metal} (decrease of E_{metal} in $\lambda < \lambda_{\mathrm{R}}$ comes from the radiation of the 1st order diffraction).

In the following, the dark band in the enhancement under the slit is analyzed.

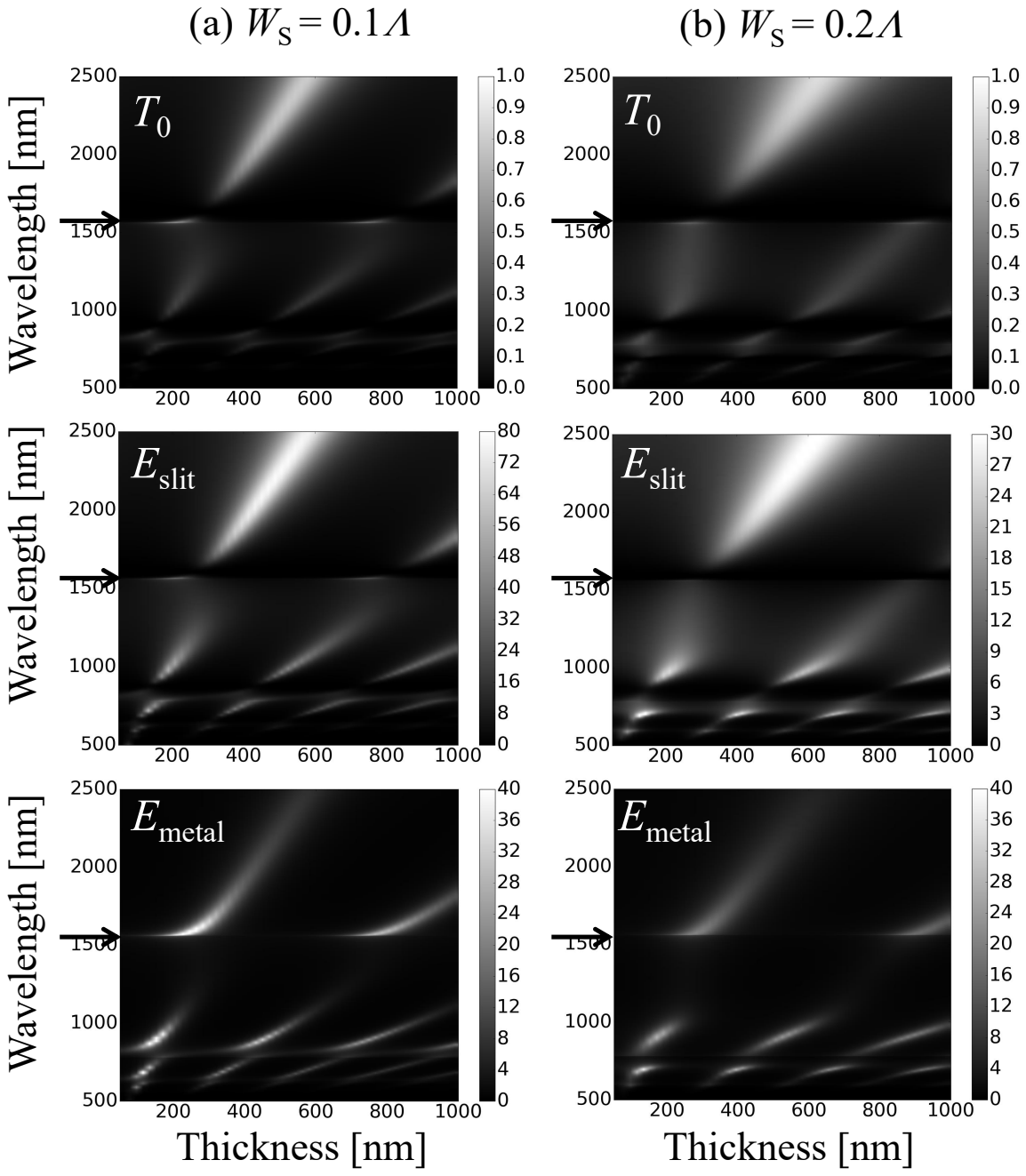

Figure 3.9: Zeroth order transmission T_0, enhancement under slit E_{slit}, and enhancement under metal E_{metal} in grayscale as functions of the wavelength and the metal thickness for $W_s = 0.1\Lambda$ (a) and 0.2Λ (b). The arrows on the vertical axes indicate the position of λ_{R}. Note that the scales for E_{slit} are different between the two cases.

3.4.2 Origin of the dark band for the enhancement under the slit

Basically, the peak of the enhancement occurs for the condition of Eq. 3.4 as mentioned above. To consider the origin of the dark band in the enhancement under the slit E_{slit}, the reflection coefficient on the substrate interface was calculated numerically. Figure 3.10 (a) shows the enhancement under the slit E_{slit} for the three different thickness, and Fig. 3.10 (b) shows the phase and amplitude of ρ_3 for $w_s = 0.1\Lambda$. At the dip wavelength (corresponds to the dark band), $|\rho_3| \simeq 1$ and $\arg(\rho_3) \simeq \pi$, which means $\rho_3 \simeq -1$ (fixed end), then the electric field component parallel to the interface is nearly 0 at the interface. In the narrow slit case, slit mode is the single TM_0 for the near infrared region and is similar to the TEM mode. In this case, the vertical component of the electric field E_{z} is also nearly zero. Therefore, the dark band which exists at the wavelength slight longer than λ_{R} was caused by fixed end reflection of the slit mode. Note that, although the rigorous fixed end is $\rho_3 = -1$, the wavelengths at which $\arg(\rho_3) \simeq \pi$ and $\rho_3 \simeq -1$ occur are not exactly the same. However, $\arg(\rho_3) \simeq \pi$ and $\rho_3 \simeq -1$ occur very close wavelengths. This indicates that presence of the dark band in the enhancement under the slit E_{slit} in $\lambda > \lambda_{\mathrm{R}}$ is the general nature of the metal grating.

3.4.3 Behavior of reflection coefficient

The approximated expression of the reflection coefficient was obtained as Eq. 3.7. For simplicity, the slit mode is approximated as the TEM mode inside the MIM waveguide with perfect conductor. Under this approximation, $Y_{\mathrm{eff}} = Y_{\mathrm{slit}} = Y_{\mathrm{TEM}} = 1/Z_0$. By substituting $k_x = 2\pi/\Lambda = 2\pi/n_3\lambda_{\mathrm{R}}$ whose in-plane wavenumber corresponds to the normal incident, then

$$b = \frac{1}{S^2}\left[\frac{1-S^2}{\sqrt{|\epsilon_{\mathrm{m}}|}} - \frac{1}{n_3}\sqrt{\left(\frac{\lambda}{\lambda_{\mathrm{R}}}\right)^2 - 1}\right] \tag{3.13}$$

is obtained. From Eq. 3.13, $b \simeq -\infty$ for the limit of the long wavelength $\lambda >> \lambda_{\mathrm{R}}$. In this case $\arg(\rho_3) \simeq 0$. By shifting the wavelength to the shorter region $\lambda = \lambda_{\mathrm{R}}$, b ($\arg(\rho_3)$) increases monotonously, and is

$$b(\lambda = \lambda_{\mathrm{R}}) = \frac{1}{S^2}\frac{1-S^2}{\sqrt{|\epsilon_{\mathrm{m}}|}} \tag{3.14}$$

for $\lambda = \lambda_{\mathrm{R}}$. Since $S^2 < 1$, $b(\lambda = \lambda_{\mathrm{R}}) > 0$. Therefore, $\arg(\rho_3) > \pi$.

Here, consider the wavelength which satisfies $\arg(\rho_3) = \pi$ and $|\rho_3| = 1$. $\arg(\rho_3) = \pi$ is satisfied when $b = 0$. Therefore, from Eq. 3.13, $\arg(\rho_3) = \pi$ and $|\rho_3| = 1$ is satisfied for

$$\lambda_\pi = \lambda_{\mathrm{R}}\sqrt{\epsilon_3\left(\frac{1-S^2}{\sqrt{|\epsilon_{\mathrm{m}}|}}\right)^2 + 1}. \tag{3.15}$$

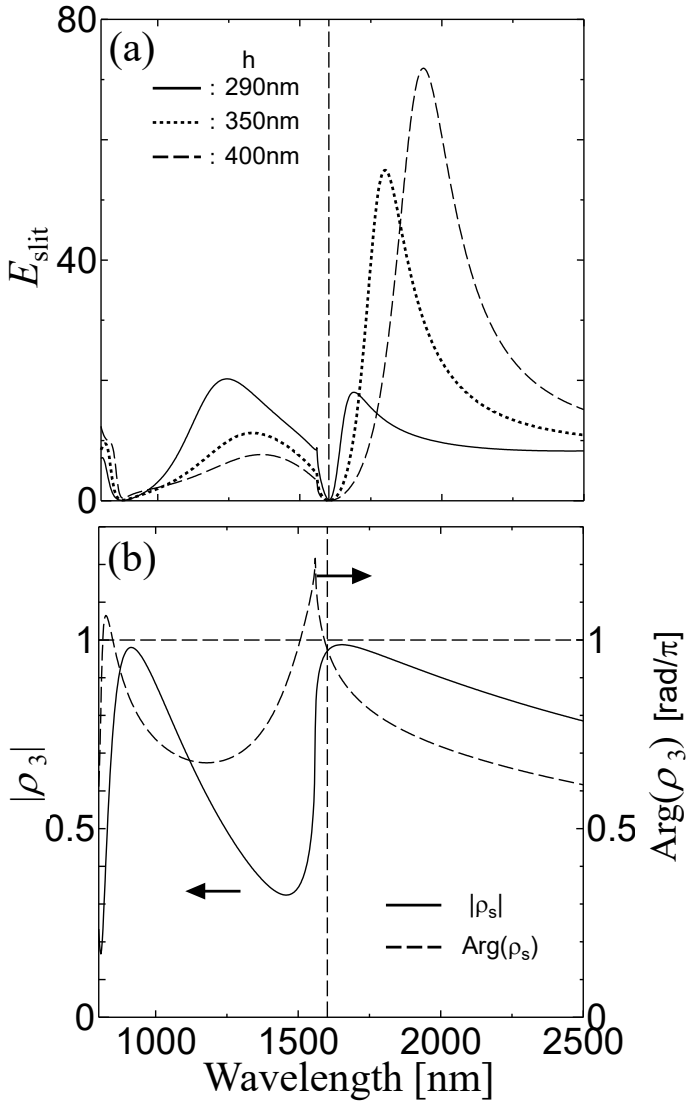

Figure 3.10: (a) Enhancement under slit E_{slit} and (b) the amplitude and phase of the reflection coefficient ρ_3 for the slit mode at the slit/substrate boundary. The dash-dotted lines indicate the wavelength at which E_{slit} becomes minimal.

On the other hand, $|\rho_3| = 1$ corresponds to $\tau_3 = 0$ (condition for the dip caused by Fano resonance in transmittance spectrum) and occurs at

$$\lambda_{\mathrm{SPF}} \simeq \lambda_{\mathrm{R}} \sqrt{\frac{|\epsilon_{\mathrm{m}}| + \epsilon_3}{|\epsilon_{\mathrm{m}}|}} \tag{3.16}$$

as mentioned in the section 3.4.1. At the wavelength λ_{SPF}, $b < 0$. Therefore, $\arg(\rho_3) < \pi$. $\arg(\rho_3) = \pi$ and $|\rho_3| = 1$ occurs close to each other in the spectrum, and $\rho_3 \simeq -1$ in between them. The presence of the dielectric ϵ_3 only slightly alters λ_π and λ_{SPF}. In the presence of the metal loss, $|\rho_3| < 1$ for $\tau_3 = 0$. Also, in case $|\epsilon_{\mathrm{m}}|$ is small (less than 5), the wavelength which $\tau_3 = 0$ occurs deviates from λ_{SPF}. Qualitatively, however, there always exists the wavelength which satisfies $\rho_3 \simeq -1$ in the wavelength longer than λ_{R}. Eq. 3.7 and the following equations (Eq. 3.13 to Eq. 3.16) were obtained by ignoring the diffraction (evanescent) wave in the region III. To confirm the validation of the above discussion which used these approximated equations, ρ_3 without the approximation were calculated for some conditions using SCMT as shown in Fig. 3.11. Solid and dashed lines are the narrow slit (S^2 is small) and wide slit (S^2 is large) cases, respectively.

Here, we comment on the case $|\epsilon_{\mathrm{m}}|$ is small ((a) or (c)). In such a case, λ_{SPF} shifts from λ_{R} toward longer wavelength because of the plasmonic properties of the metal surface. In addition, electromagnetic field is strongly confined on the metal/dielectric interface. Even in the finite slit width, surface plasmon is still quasi bound state as long as the slit width is narrow since, in such a narrow width, radiation via the scattering at the slits is weak. When such a relatively stable surface plasmon exists, absorption by the metal at the resonant frequency is strong. Because of this, phase of the reflection changes largely. Dips in $|\rho_3|$ for the solid lines of (a), (c) and the large variation of $\arg(\rho_3)$ correspond to the resonance. When the wavelength λ approaching λ_{R}, the reflection phase exceeds 2π, which cannot be expressed by Eq. 3.7 and 3.8. The discrepancy is considered to be come from ignoring the diffraction wave in Region III.

Although such a limitation exists for the range of application, the properties:

1) $\arg(\rho_3) \to 0$ for $\lambda \to \infty$

2) $|\rho_3| \simeq 1,\ \arg(\rho_3) < \pi$ for λ_{SPF}

3) $\lambda_{\mathrm{R}} < \lambda_\pi < \lambda_{\mathrm{SPF}}$

4) $\lambda_\pi \to \lambda_{\mathrm{SPF}}$ when $S^2 \to 0$

are shown based on the approximated expressions, and can be confirmed in Fig. 3.11. Therefore, it is the general property of the metal grating that the dark band which corresponds to the fixed end reflection of the slit mode appears at the wavelength slightly longer than λ_{R}. Note that, at the wavelength near λ_{SPF} of the metal/incident region interface, most of the incident wave will not enter the slit (reflected). Therefore, the enhancement on the exit side (substrate region) of the slit is also zero. In addition, the enhancement under the metal is nearly zero. Thus, when the value of the dielectric constant on each side of the grating is close, the origin of the dark bands in enhancement is different.

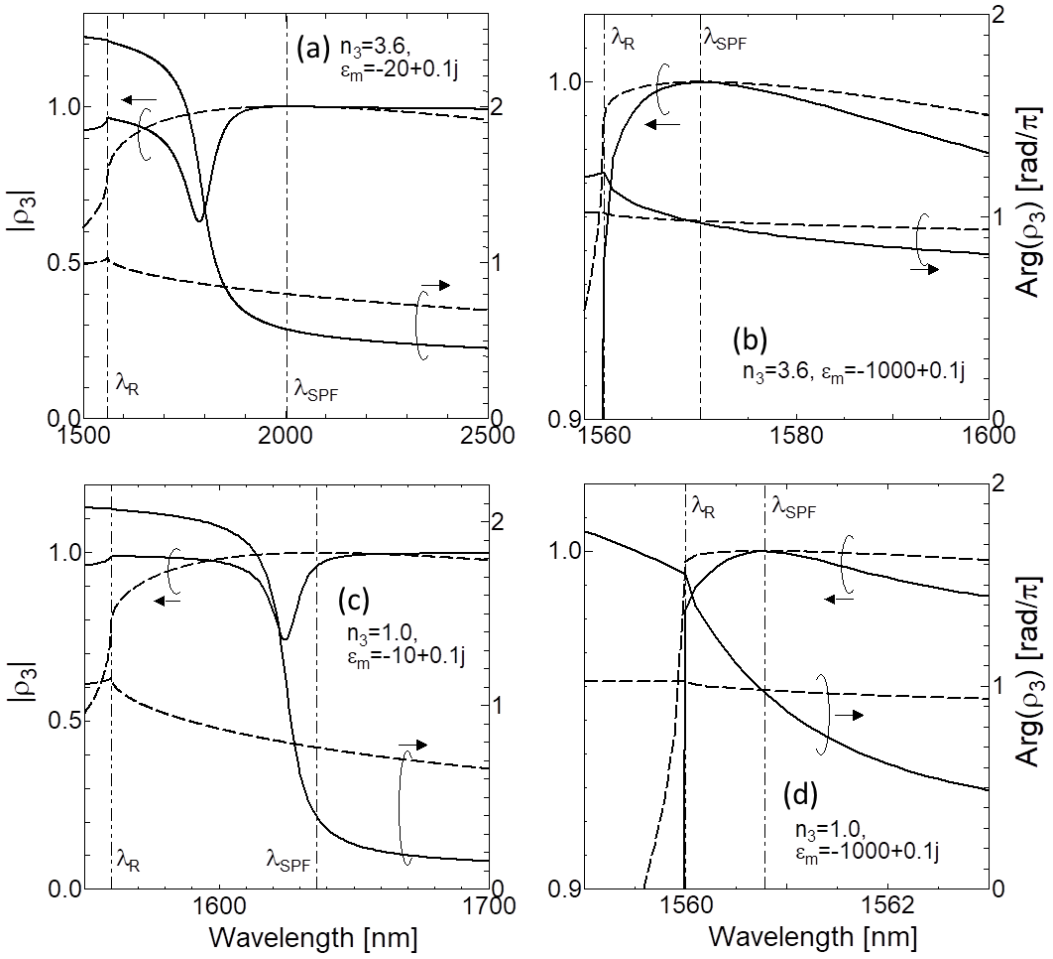

Figure 3.11: Amplitude and phase of the reflection coefficient ρ_3 for various cases of the grating and substrate parameters; (a) $n_3 = 3.6$, $\epsilon_{\rm m} = -20 + 0.1i$, (b) $n_3 = 3.6$, $\epsilon_{\rm m} = -1000 + 0.1i$, (c) $n_3 = 1.0, \epsilon_{\rm m} = -10 + 0.1i$, and (d) $n_3 = 1.0, \epsilon_{\rm m} = -1000 + 0.1i$. The solid and dashed lines are the results for $w_s = 15.6$ nm (0.036Λ) and $w_s = 130$ nm (0.3Λ) in (a) and (b), $w_s = 15.6$ nm (0.01Λ) and $w_s = 468$ nm (0.3Λ) in (c) and (d), respectively. In all the cases, $\lambda_{\rm R} = n_3\Lambda = 1560$ nm.

3.5 Summary

In this work, which focuses on the BM, we discussed the spectral features and the underlying physics in the transmission T_0 and the averaged near-field enhancement E in the metal gratings on a semiconductor substrate. It was found that, for telecom and longer wavelengths, the BM disappears in the thin grating and the peaks in T_0 and the averaged E are pinned at $\lambda_{\rm R}$. In contrast, the BM in the gratings in air is usually present, resulting in spectral peaks at the wavelength of the BM longer than $\lambda_{\rm R}$. However, the peaks are suppressed when the BM sits around $\lambda_{\rm SPF}$ due to the Fano resonance. We showed that the difference comes predominantly from the dielectric

symmetry above and below the grating and can be explained in terms of the reflection phase for the slit mode at the grating–dielectric interfaces. We also showed that the plasmonic band gap is large in the grating on a substrate enhancing the disappearance of the BM.

In addition, we investigated the enhancement under the slit E_{slit}. The peak of E_{slit} basically corresponds to BM. At the wavelength slightly longer than the Rayleigh wavelength, the dark band which corresponds to the decrease of enhancement exists. The dark band came from the fixed end reflection at the slit/dielectric interface. This phenomenon is general for the metal grating.

Though we showed in this paper the results for the cases of a relatively narrow slit, the discussion may also be valid for a wider slit as long as the propagating fundamental slit mode is dominant. In addition, the physical picture based on the BM analysis is valid for a wider range of the wavelength and of structural and material parameters.

Chapter 4

Polarization dependence of bound states in the continuum in the dielectric waveguide with metal grating

4.1 Study of bound states in the continuum

A bound state in the continuum (BIC) [8, 54] is a non-radiative state that lies in the continuous spectral range spanned by the radiation modes. Unlike the quasi-bound states, the BIC, in principle, has an infinitely high quality factor. Although the BIC itself cannot be excited by the incident wave, the Q factor becomes very high near the BIC, which is expected in high-Q devices. The BIC was originally mentioned in Quantum Mechanics in 1929 by Von-Neumann and Wigner [12]. The phenomenon is commonly seen in open-wave systems such as acoustics [55–57], water waves [58,59], and optics [11,60–89]. In optics, the BIC is attracting interest in the context of metasurfaces [60–62], photonic structures [11, 63–81, 84, 85, 88, 89] and plasmonics [82, 83]. So far, various nano-photonic/plasmonic applications using BICs have been proposed, such as lasers [84, 85], modulators [82], and filters [66], SHG or nonlinear optics [73, 77] etc.

Most of the BICs found so far are categorized into two types: the symmetry-protected BIC [60–62, 66, 68, 71–77, 80, 83, 85, 86] and the Friedrich-Wintgen (FW) BIC [55–57, 63–65, 67–70, 72–75, 78, 79, 81–84, 86–91]. The former BIC results from the incompatible symmetry of one of the localized modes with the external radiation field that usually appears at the center of the Brillouin zone (at Γ point). The latter results from the destructive interference of radiations from the two modes that can appear at the off-Γ point around the crossing or anti-crossing point of the dispersion curves of the two modes, depending on the strength of the coupling between them.

We focus on the FW-BIC formed between the two localized modes that are strongly coupled by the near-field overlap with the structural perturbation that produces the

coupling to external radiation. In this case, a mode anti-crossing occurs, and the BIC appears on one of the two split-branches. Such a type of BIC is reported in cylindrical resonator system [87–89] and the periodic structures such as photonic [63, 78, 79, 81] or plasmonic structures [83]. As is pointed out by Friedrich and Wintgen [90], the regime where the Q factor is kept high around the BIC becomes larger as the near-field coupling becomes stronger. This regime is called the near BIC [83] or the supercavity regime [88] and is targeted in searching for extraordinarily high-Q modes. Therefore, a thorough understanding of the physics behind this type of BIC is quite important for the realization of practical high-Q devices.

The position at which the FW-BIC appears is extremely sensitive to, and dependent on, the structure and parameters of the system. In FW theory [90], it was shown that the shift of the BIC position from the anti-crossing point is determined by the strength of the couplings among the two closed and one open channel based on the Feshbach projection operator method [92]. Moreover, which of the two interfering resonances becomes a BIC was shown to depend on the sign of the product of the matrix elements coupling these channels. Indeed, BICs have been observed on different branches depending on the system, e.g., on the lower energy branch in a metal relief grating coupled to a dielectric slab waveguide [83], and on the higher energy branch in a low-contrast dielectric grating [79]. Therefore, it is important to understand how the BIC position changes depending on the structure and parameters of the system, in order to characterize the interfering resonances and to determine the optimum design for a high-Q device.

In this chapter, we demonstrate a phenomenon where the branch at which the BIC appears changes depending on the polarization of the waveguide modes that compose the BIC, which can be selected by the polarization of incident light, in a dielectric-waveguide/metal-grating structure. If the conclusion of FW theory is applicable to this system, this phenomenon is caused by the sign change of the coupling coefficients among waveguide modes and external radiation. We carry out two actions to confirm this hypothesis. Initially, following temporal coupled mode theory (TCMT) [25, 93], which describes general classical open-wave systems, we obtain the BIC condition for the system with two resonant modes and one radiative mode. We pay attention to the signs of the coupling coefficients, and check whether the system conforms to FW theory. Next, we estimate the signs of the coupling coefficients by the waveguide-mode decomposition of the electric fields inside the dielectric layer, which is obtained numerically via the use of a spatial coupled mode theory (SCMT) [21,22,35], and observe how the sign of the product of the coupling coefficients depends on the polarization of incident light. We note here that SCMT and TCMT are essentially different theories despite their similar names. SCMT is an electromagnetic theory for those systems with a metallic aperture array, wherein Maxwell equations are solved by a modal expansion of electromagnetic fields. On the other hand, TCMT is a more general theory. This method derives a set of equations of motion for simple oscillators whose energy can be transferred to the outside. Therefore, no specific electromagnetic formulation is employed in it.

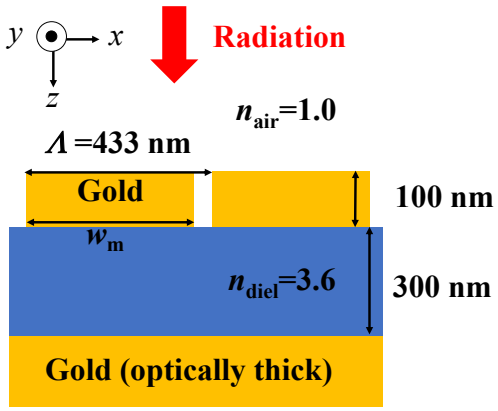

Figure 4.1: Cross sectional structure of the device considered in this work.

4.2 Device structure

As the complex permittivity of the gold grating and backing metal, unless otherwise stated, we used a Drude-Lorentz model fitted to the Johnson-Christy data [53]. In some analyses, we consider the lossless gold by ignoring the imaginary part (loss) of the gold permittivity. We note that this loss elimination is done only for the purpose of theoretical analysis to elucidate the behavior of the BIC. We consider a planar dielectric waveguide structure as shown in Fig. 4.1. It consists of a gold grating on a dielectric layer with a backing metal layer of infinite thickness. Therefore, any wave incident from the grating side is totally reflected except for some absorption. The reflectance as well as the fields inside the device were calculated by the SCMT, for the incident plane wave with S or P polarization, of which the electric or magnetic field has only y-component. The grating with a period of $\Lambda = 433$ nm is composed of a gold strip whose width w_{m} is 0.98Λ for the P-wave and 0.8Λ for the S-wave. These widths were chosen to facilitate clear observation of the BICs. Note that the grating is 0th order in the air for the wavelength range considered here.

4.3 Calculation results

We display the dispersion of the 0th order reflectance on the gray scale map for the two polarizations in Fig. 4.2. In both diagrams, dark bands (low reflectance = high absorption) are clearly seen. The dashed lines indicate the dispersion of the empty lattice modes of the dielectric waveguide sandwiched by the two flat metal planes. We name the lowest order waveguide modes TM_0 and TE_0, and the second modes, TM_1 and TE_1 for the P- and S-polarizations, respectively. The TE_1 mode is cut off for $\lambda > 1.25$ μm. The dark bands correspond well to the empty lattice modes. Therefore, they are attributed to absorption caused by the metallic loss in the grating and backing metal associated with the dielectric waveguide modes.

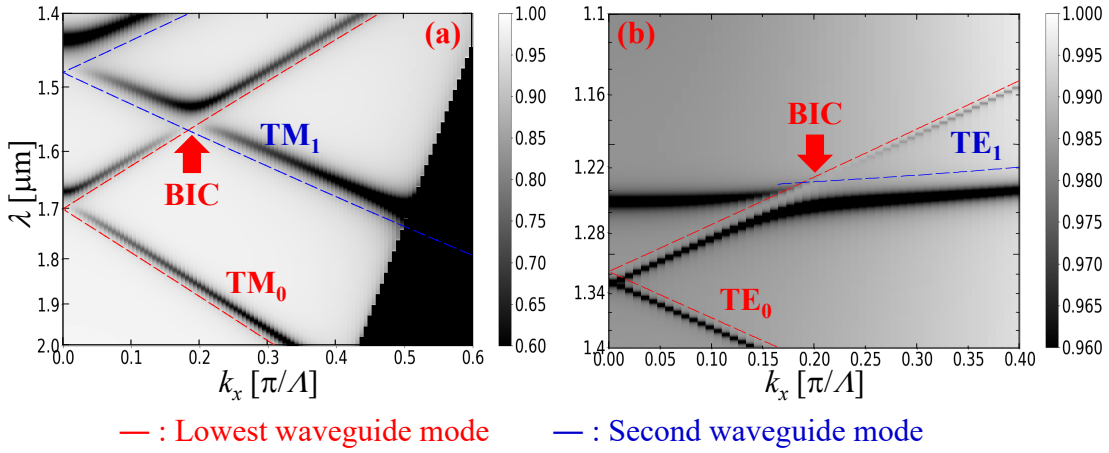

Figure 4.2: Reflectance as a function of the in-plane wave vector and the incident wavelength; (a) P-wave incidence, (b) S-wave incidence. Axis of the wavelength is in inverted scale (which means the linear scale in the frequency). The dashed lines indicate the dispersion of the empty lattice modes of the dielectric waveguide. The red arrows indicate the location of the BICs.

At the intersection of the two modes, in both polarizations, one can see an anti-crossing that is caused by the near-field coupling between the two modes induced by the grating. Moreover, near the anti-crossing, the dark band disappeared locally at the positions indicated by the arrows in both polarizations. The disappearance of the absorption corresponds to the BIC. Here a remarkable feature is that the BIC lies on the lower-frequency branch for the P-polarization, whereas it lies on the higher-frequency branch for the S-polarization. This feature is the subject of this study and will be discussed in detail in the next section. However, we first confirm that the disappearance of the absorption is indeed due to the formation of the BIC by evaluating the imaginary part of the eigenfrequency along the lower and upper dark bands for the P-wave and S-wave cases, respectively. In the calculation, the imaginary part of the metal permittivity was removed so that the imaginary part of the eigenfrequency corresponds to the external (radiation) loss. The results are shown in Fig. 4.3. In both polarizations, the imaginary parts drop to zero at the point where the absorption disappears ($k_x \sim 0.2\ [\pi/\Lambda]$), demonstrating that the BICs are indeed formed at that location.

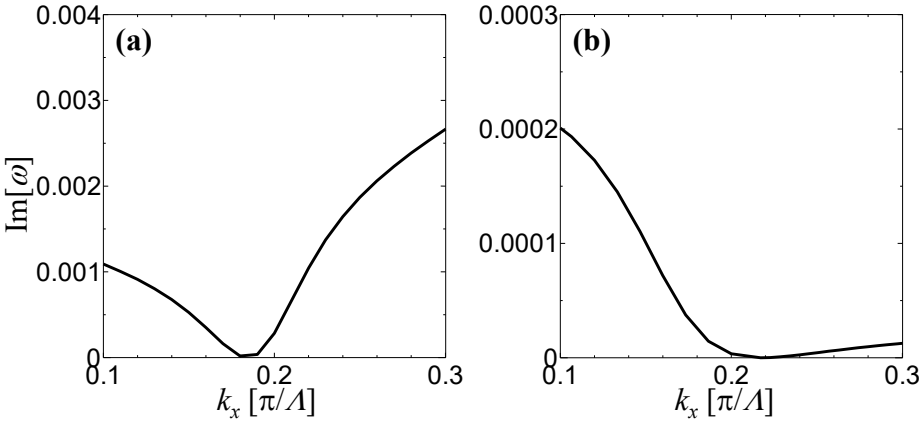

Figure 4.3: Imaginary part of the eigenfrequencies along the branch on which BIC appears; (a) P-wave (lower branch) and (b) S-wave (upper branch).

4.4 Discussion

4.4.1 Theoretical analysis using temporal coupled mode theory

In this chapter, the results were analyzed using the TCMT which was described in 2.3. First, the reflectance spectra calculated using Eq. 2.35 are shown in Figs. 4.4 (c) and 4.4 (d) for $p = 1$ and -1, respectively, and $\alpha > 0$ for both cases. The parameters used in the calculations, listed in the caption, were decided so as to fit the SCMT results redrawn in Figs. 4.4 (a) and 4.4 (b) from Figs. 4.2 (a) and 4.2 (b) with some magnification. As is clearly seen, the reflectance spectra were accurately reproduced by the TCMT calculation. Importantly, the positions of the BIC are correctly predicted.

The appearance of the BIC is analyzed as follows [24, 90, 94]. Omitting the internal loss $\mathbf{\Gamma_i}$, the eigenvalues for $\tilde{\mathbf{H}}$ are determined by

$$\left|\tilde{\mathbf{H}} - \omega\mathbf{I}\right| = \{(\omega_1 - \omega) - i\gamma_{e1}\}\{(\omega_2 - \omega) - i\gamma_{e2}\} + (i\alpha + p\sqrt{\gamma_{e1}\gamma_{e2}})^2 = 0, \tag{4.1}$$

where $\mathbf{I}$ is the identity matrix. If we express the two solutions of Eq. 4.1 as β and χ, the sum and the product of them yield

$$\beta + \chi = \omega_1 + \omega_2 - i\gamma_{e1} - i\gamma_{e2}, \tag{4.2}$$

$$\beta\chi = (\omega_1 - i\gamma_{e1})(\omega_2 - i\gamma_{e2}) + (i\alpha + p\sqrt{\gamma_{e1}\gamma_{e2}})^2. \tag{4.3}$$

When a BIC is realized, one of the solutions is purely real. In that case, the solutions can be expressed using real numbers A and B as

$$\beta = A - i\gamma_{e1} - i\gamma_{e2}, \tag{4.4}$$

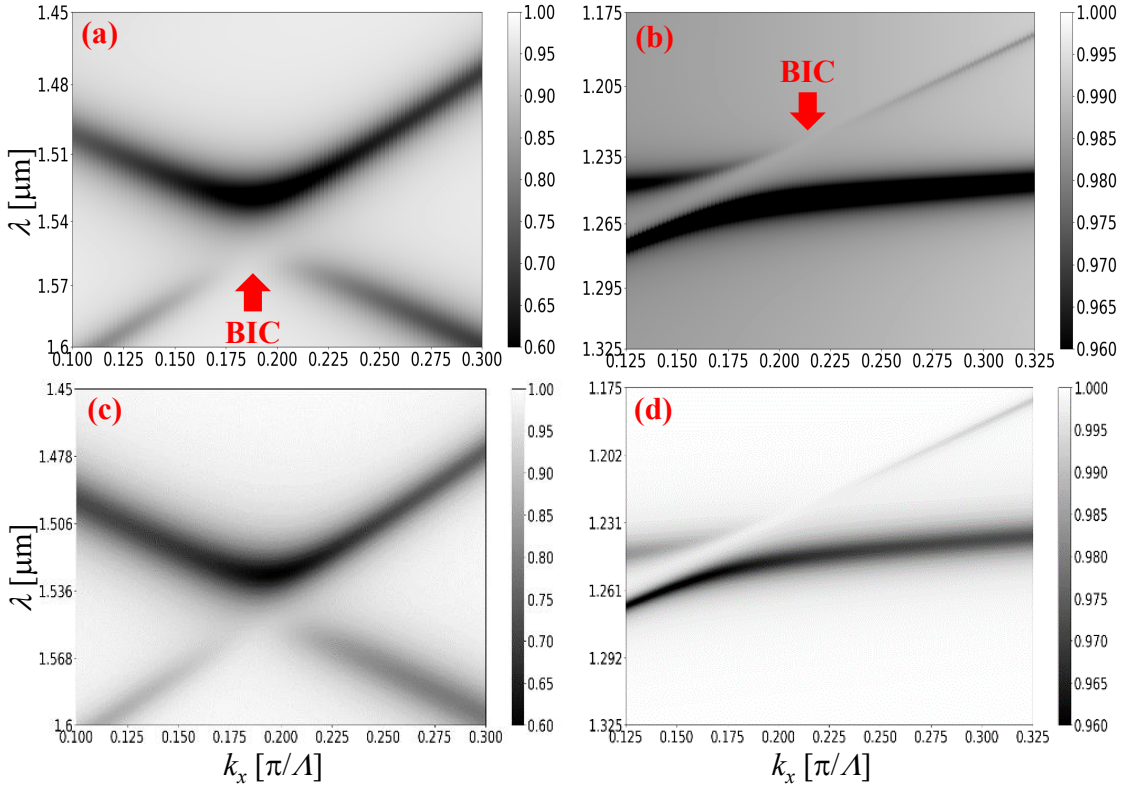

Figure 4.4: Reflectance as a function of the in-plane wave vector and the incident wavelength around the anti-crossing point. (a) P-wave and (b) S-wave redrawn from Figs. 4.2(a) and 4.2(b), respectively. The results of the TCMT calculation using Eq. 2.35 for (c) $p = 1$ and (d) $p = -1$ with the following parameters; (c) $\gamma_{i1}/c = 2.03 \times 10^{-2}, \gamma_{i2}/c = 3.15 \times 10^{-2}, \gamma_{e1}/c = 2.18 \times 10^{-3}, \gamma_{e2}/c = 4.42 \times 10^{-3}, \alpha/c = 3.52 \times 10^{-2}$, (d) $\gamma_{i1}/c = 6.24 \times 10^{-3}, \gamma_{i2}/c = 2.64 \times 10^{-2}, \gamma_{e1}/c = 5.77 \times 10^{-5}, \gamma_{e2}/c = 3.33 \times 10^{-4}, \alpha/c = 3.28 \times 10^{-2}$. Here c is the velocity of light in a vacuum.

$$\chi = B. \tag{4.5}$$

By substituting Eqs. 4.4 and 4.5 to Eq. 4.3, the following relations are obtained for A and B,

$$A + B = \omega_1 + \omega_2, \tag{4.6}$$

$$AB = \omega_1\omega_2 - \alpha^2. \tag{4.7}$$

Therefore, A and B are the solutions of the equation

$$x^2 - (\omega_1 + \omega_2)x + \omega_1\omega_2 - \alpha^2 = 0. \tag{4.8}$$

In addition, by comparing the imaginary parts of both sides of Eq. 4.3, the expression for B is obtained as

$$B = \frac{\omega_1\gamma_{e2} + \omega_2\gamma_{e1} - 2p\alpha\sqrt{\gamma_{e1}\gamma_{e2}}}{\gamma_{e1} + \gamma_{e2}}. \tag{4.9}$$

The solutions of Eq. 4.8 are

$$x_\pm = \frac{1}{2}\{\omega_1 + \omega_2 \pm \sqrt{(\omega_1 - \omega_2)^2 + 4\alpha^2}\}. \tag{4.10}$$

Because B must be one of the two solutions, $x_\pm$, the following condition must be satisfied for Eq. 4.9;

$$\pm\sqrt{(\omega_1 - \omega_2)^2 + 4\alpha^2} = -\frac{(\omega_1 - \omega_2)(\gamma_{e1} - \gamma_{e2}) + 4p\alpha\sqrt{\gamma_{e1}\gamma_{e2}}}{\gamma_{e1} + \gamma_{e2}}. \tag{4.11}$$

By squaring both sides of Eq. 4.11 the following conditions are obtained for the existence of the BIC;

$$p\alpha(\gamma_{e1} - \gamma_{e2}) = \sqrt{\gamma_{e1}\gamma_{e2}}(\omega_1 - \omega_2). \tag{4.12}$$

Here we note that the expression Eq. 4.12 was derived in [24, 90]. Substituting Eq. 4.12 into Eq. 4.1 and then solving Eq. 4.1 with respect to ω, we obtain the following solutions

$$\omega = \begin{cases} \frac{1}{2}(\omega_1 + \omega_2) + \frac{p\alpha}{2}(\sqrt{\frac{\gamma_{e1}}{\gamma_{e2}}} + \sqrt{\frac{\gamma_{e2}}{\gamma_{e1}}}) - i(\gamma_{e1} + \gamma_{e2}), \\ \frac{1}{2}(\omega_1 + \omega_2) - \frac{p\alpha}{2}(\sqrt{\frac{\gamma_{e1}}{\gamma_{e2}}} + \sqrt{\frac{\gamma_{e2}}{\gamma_{e1}}}). \end{cases} \tag{4.13}$$

The latter solution represents the BIC, which does not have an imaginary part. Therefore, the BIC appears in the lower frequency branch when

$$p\alpha > 0, \tag{4.14}$$

whereas the BIC appears in the higher frequency branch when

$$p\alpha < 0. \tag{4.15}$$

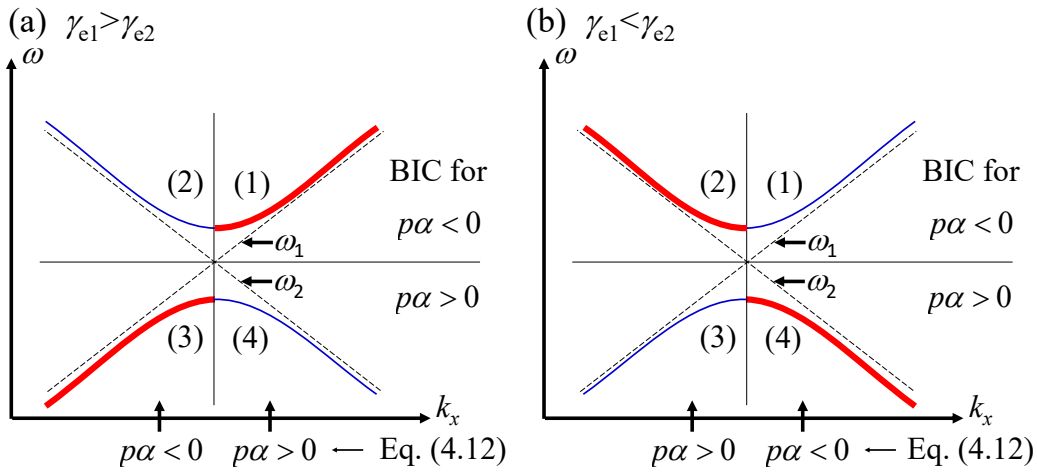

Figure 4.5: Illustration of the quadrant where BIC appears in the dispersion diagram near the anti-crossing point for (a)$\gamma_{e1} > \gamma_{e2}$ and (b)$\gamma_{e1} < \gamma_{e2}$. The red and blue lines depict the dispersions whose radiation loss is the larger (broad linewidth) and the smaller (narrow linewidth) of the two, respectively.

This result about the BIC-branch selection is consistent with the FW theory [90].

The regions where the BIC appears in the dispersion diagram can be discussed based on Eqs. 4.12, 4.14, and 4.15. Consider the dispersion of ω_1 and ω_2 having positive and negative slopes, respectively as shown in Fig. 4.5. Let us first consider the case of $p\alpha > 0$, for which, from Eq. 4.12, the signs of $\omega_1 - \omega_2$ and $\gamma_1 - \gamma_2$ should be the same. Hence, $\omega_1 > \omega_2$ must be satisfied for $\gamma_{e1} > \gamma_{e2}$, corresponding to division (1) or (4) in Fig. 4.5(a), while $\omega_1 < \omega_2$ for $\gamma_{e1} < \gamma_{e2}$, corresponding to division (2) or (3) in Fig. 4.5(b). On the other hand, considering Eq. 4.14, the BIC appears on the lower branch for $p\alpha > 0$. Therefore, the BIC appears in division (4) in Fig. 4.5(a) for $\gamma_{e1} > \gamma_{e2}$ and division (3) in Fig. 4.5(b) for $\gamma_1 < \gamma_2$, respectively. The case of $p\alpha < 0$ can be analyzed in a similar way. For $\gamma_{e1} > \gamma_{e2}$ and $\gamma_{e1} < \gamma_{e2}$, the BIC appears in division (2) in Fig. 4.5(a) and division (1) in Fig. 4.5(b), respectively. We further note that in both cases, the BIC appears on the mode with the lower radiative loss.

Next, let us check the correspondence between the above argument and the result in our structure shown in Fig. 4.4. In the case of P-wave excitation shown in Fig. 4.4(a), we can see that the TM_0 (ω_1) mode with positive slope is narrower than the TM_1 (ω_2) mode with negative slope, namely $\gamma_{e1} < \gamma_{e2}$ corresponding to Fig. 4.5(b), and the BIC is located on the branch in division (3), as confirmed by the fitting shown in Fig. 4.4(c). Hence, the above argument predicts $p\alpha > 0$. In the case of S-wave excitation, it is clear from Fig. 4.4(b) that the linewidth of the TE_0 (ω_1) mode is much narrower than the TE_1 (ω_2) mode, namely $\gamma_{e1} < \gamma_{e2}$ corresponding again to Fig. 4.5(b), and the BIC appears in division (1). Therefore, $p\alpha < 0$ is predicted. In the next subsection, we will confirm the above prediction, $p\alpha > 0$ and $p\alpha < 0$ for the P-wave and S-wave excitations, respectively, in our specific structure, by checking the signs of p and α from the SCMT

calculation.

4.4.2 Evaluation of the signs of p and α using spatial coupled mode theory

As shown in the preceding section, the branch on which the BIC appears depends on the sign of $p\alpha$. Here, p denotes the phase difference (sign) between the coefficients that couple the waveguide modes with the external radiation; $p = 1$ and -1 means $\varphi_1 - \varphi_2 = 0$ and π, respectively. The phase difference between the two waveguide modes excited by the incident radiation is determined solely by these coupling coefficients, if the effects of near- and far-field couplings are negligible. Thus, the sign p can be evaluated easily from the phases of the excited waveguide modes. On the other hand, α represents the near field (direct) coupling between two resonant modes. As shown below, the sign(α) can also be found by inspecting the phases of the waveguide modes that construct the coupled resonant modes at the anti-crossing point.

We determine the phase of the waveguide modes from the actual SCMT simulation. Assume that the electric and magnetic fields inside the dielectric layer is expanded by the propagating waveguide modes in the flat metal/dielectric/metal waveguide as [95]

$$\begin{aligned}
\mathbf{E}(x,z) &= a_{1+}\mathbf{E}_{1+}(x,z) + a_{2+}\mathbf{E}_{2+}(x,z) + \cdots \\
&\quad + a_{1-}\mathbf{E}_{1-}(x,z) + a_{2-}\mathbf{E}_{2-}(x,z) + \cdots, \\
\mathbf{H}(x,z) &= a_{1+}\mathbf{H}_{1+}(x,z) + a_{2+}\mathbf{H}_{2+}(x,z) + \cdots \\
&\quad + a_{1-}\mathbf{H}_{1-}(x,z) + a_{2-}\mathbf{H}_{2-}(x,z) + \cdots .
\end{aligned} \tag{4.16}$$

Here, $\mathbf{E}_{i\pm}$, $\mathbf{H}_{i\pm}$ represents the transverse components (in y-z plane in Fig. 4.1) of the electric and magnetic fields of the i-th waveguide mode, respectively, and the signs $+$ and $-$ denote the mode propagating in the $+x$ and $-x$ directions, respectively. $a_{i\pm}$ represents the complex amplitude of each waveguide mode. As seen in Fig. 4.2, only two modes are relevant near the BIC point. Hence, Eq. 4.16 can be simplified to

$$\begin{aligned}
\mathbf{E}(x,z) &= a_{1s}\mathbf{E}_{1s}(x,z) + a_{2s'}\mathbf{E}_{2s'}(x,z), \\
\mathbf{H}(x,z) &= a_{1s}\mathbf{H}_{1s}(x,z) + a_{2s'}\mathbf{H}_{2s'}(x,z),
\end{aligned} \tag{4.17}$$

where s and s' are either $+$ or $-$. In the case of Fig. 4.2(a) for the P-wave radiation, mode 1 and mode 2 correspond to the TM_0 mode propagating in $+x$ direction and the TM_1 mode propagating $-x$ direction, respectively. In the case of Fig. 4.2(b) for the S-wave radiation, they correspond to the TE_0 mode propagating in $+x$ direction and the TE_1 mode propagating in $+x$ direction, respectively. The direction of propagation was determined from the slope of the corresponding empty lattice mode. The amplitude a_{is} is obtained by

$$a_{is} = \int dz \left(\frac{\mathbf{E} \times \mathbf{H}_{is}^* + \mathbf{E}_{is}^* \times \mathbf{H}}{\mathbf{E}_{is} \times \mathbf{H}_{is}^* + \mathbf{E}_{is}^* \times \mathbf{H}_{is}} \right), \tag{4.18}$$

using the electric field $\mathbf{E}$ and the magnetic field $\mathbf{H}$ obtained by the actual SCMT calculation. The integration is performed over the dielectric region.

4.4.3 Evaluation of p

We evaluate the phase difference at the wavelength where the anti-crossing occurs, $k_x = 0.1905\ [\pi/\Lambda]$ and $0.1600\ [\pi/\Lambda]$ for the P-wave and S-wave excitations, respectively. The calculated phase difference in SCMT is shown in Figs. 4.6(a) and 4.6(b) for the P-wave and S-wave cases, respectively. We denote the upper and lower branch of the coupled resonant wavelength as ω_+ and ω_-, respectively.

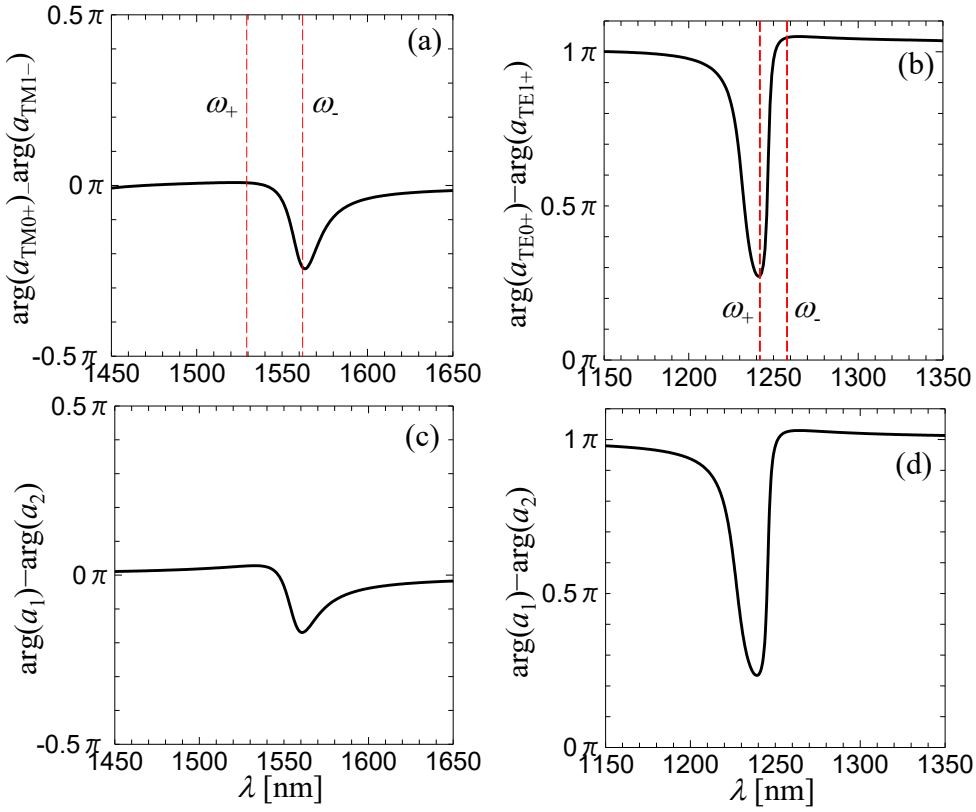

Figure 4.6: Phase difference of two modes excited by the external radiation; (a) P-wave at $k_x = 0.1905\ [\pi/\Lambda]$ and (b) S-wave at $k_x = 0.1600\ [\pi/\Lambda]$ by the SCMT calculations, (c)$p = 1$ and (d)$p = -1$ by the TCMT calculations. Red dashed lines in (a) and (b) indicate the wavelengths of the coupled resonant modes ω_+ and ω_-.

Around ω_+ or ω_-, the phase difference between the waveguide modes varies rapidly due to the influence of the excitation of each resonator. However, in the region far from ω_+ and ω_-, the phase difference shows a convergence to 0 for the P-polarization and π for the S-polarization. In this region, the phase difference (sign) between the resonances should coincide with p, because the effect of the resonances on the phase difference is considered to be negligible (see Chapter 2.3).

For comparison, the phase differences were also calculated in TCMT. Figure 4.6(c) is the phase difference for $p = 1$ using the same parameters as for Fig. 4.4(c), and Fig.

4.6(d) is that for $p = -1$ with the parameters for Fig. 4.4(d). The overall behavior of the phase difference in the SCMT results (Figs. 4.6 (a) and (b)) corresponds very well to that in the TCMT results (Fig. 4.6 (c) and (d)). Therefore, it can be concluded that $p = 1$ and $p = -1$ for the P- and S-polarizations, respectively.

4.4.4 Evaluation of α

The sign of α can be deduced from the phase of the eigenmode (quasi-bound mode). In our strong near-field coupling system, the eigenmode is mainly determined by α near the anti-crossing point. In TCMT, by equating the eigenfrequencies of the two resonant modes, $\omega_1 = \omega_2 = \omega_{12}$, and neglecting $\mathbf{\Gamma_i}$ and $\mathbf{\Gamma_e}$, we have the eigenfrequencies ω_+ and ω_- from

$$|\mathbf{\Omega} - \omega \mathbf{I}| = 0, \tag{4.19}$$

as

$$\omega_\pm = \omega_{12} \pm |\alpha|, \tag{4.20}$$

and the eigenvectors are derived from

$$\begin{pmatrix} \omega_{12} - \omega & \alpha \\ \alpha & \omega_{12} - \omega \end{pmatrix} \begin{pmatrix} a_1 \\ a_2 \end{pmatrix} = 0. \tag{4.21}$$

Hence, for $\alpha > 0$,

$$a_1 = a_2 \ \text{ for } \ \omega_+, \quad a_1 = -a_2 \ \text{ for } \ \omega_- \tag{4.22}$$

and when $\alpha < 0$ we have,

$$a_1 = -a_2 \ \text{ for } \ \omega_+, \quad a_1 = a_2 \ \text{ for } \ \omega_-. \tag{4.23}$$

Therefore, the sign of α can also be evaluated from the phase difference arg(a_1)-arg(a_2) at ω_+ or ω_- around the anti-crossing point. Here ω_1 and ω_2 correspond to either TM_0 (TE_0) or TM_1 (TE_1) for the P (S)-wave case. We evaluated a_1 and a_2 from the electric field using Eq. 4.18. The electric field of the coupled resonant modes can be obtained numerically by searching for the electromagnetic wave solution in the absence of the incident wave using SCMT. In the calculation, we eliminated the imaginary part of the permittivity of gold in the grating and backing metal. Table 4.1(a) shows the results for the P-wave excitation at $k_x = 0.1905$ $[\pi/\Lambda]$ and Table 4.1(b) shows those for the S-wave case at $k_x = 0.1600$ $[\pi/\Lambda]$. In both cases, the phase difference is about 0 at ω_+ and π at ω_-, respectively. Therefore, it can be concluded that α is positive for both polarizations.

4.4.5 Sign of $p\alpha$

As shown above, $p = 1$ and $p = -1$ for the P- and S-polarizations, respectively and α is positive for both cases. Although sign(p) can be changed by the redefinition of

Table 4.1: Phase difference between the two waveguide modes to determine the sign(α).

(a) P-wave at $k_x = 0.1905\ [\pi/\Lambda]$

$[\arg(a_{TM1-}) - \arg(a_{TM0+})](\omega_+)$	$[\arg(a_{TM1-}) - \arg(a_{TM0+})](\omega_-)$	sign(α)	p
$3.45 \times 10^{-4}\pi$	0.997π	+	+1

(b) S-wave at $k_x = 0.1600\ [\pi/\Lambda]$

$[\arg(a_{TE0+}) - \arg(a_{TE1+})](\omega_+)$	$[\arg(a_{TE0+}) - \arg(a_{TE1+})](\omega_-)$	sign(α)	p
$-1.93 \times 10^{-2}\pi$	0.989π	+	−1

the phase of one of the waveguide modes, this change must be accompanied by the change of sign(α) with sign($p\alpha$) unchanged [24]. Hence, we can conclude that sign($p\alpha$) is positive in the P-polarization and negative in the S-polarization in our structure, demonstrating that the prediction by the TCMT stated in Section 4.4.1 is correct.

4.5 Summary

In conclusion, we discussed, for the first time, the branch on which the FW-BIC appears in the anti-crossing dispersion of a photonic system with a simple and practically important structure, namely dielectric waveguide with metal grating. We demonstrated that the branch is selected by the incident polarization. The mechanism was explained by TCMT in terms of the polarization-dependent phase relation between the relevant waveguide modes forming the BIC. The polarization dependence of the BIC formation in our simple structure implies the external controllability of BICs in various optical and photonic devices. Here we want to mention that the polarization selectivity was not found in the device where the top metal grating was replaced by a dielectric grating. However, a question still remains whether the plasmonic nature plays an important role in our structure, which is important not only from a viewpoint of optical physics, but also for various applications, because non-plasmonic structures may be better to obtain higher Q values. Although an answer has not been obtained, our discussion based on the TCMT applies regardless of the presence of the plasmonic effect, implying that the same or similar control of BICs is possible in various devices including all dielectric ones.

Chapter 5

Bound states in the continuum and exceptional point in dielectric waveguide equipped with metal grating : grating thickness dependence

5.1 Bound states in the continuum and exceptional point

Resonant oscillations in open resonator systems (the system that possesses the radiation port to the far region) normally decay with time because of the radiative dissipation of the energy. Even in open systems, however, purely bound states can exist when some requisite conditions are fulfilled. Such a non-decaying state in an open system is called a bound state in the continuum (BIC) [8, 54] and was originally discussed in quantum mechanics in 1929 by von Neumann and Wigner [12]. In optics, BIC was first studied theoretically in 2008 [11] and then experimentally in a waveguide array in 2011 [96]. As BIC enables strong confinement of light, which results in high-Q resonances [65], applications such as single mode lasers [84, 85], high-efficiency harmonic generation [73, 97, 98], and biosensors [76] have been demonstrated. BICs can be categorized into several types based on their physical origin [8]. Among them, two types of BIC, the symmetry-protected BIC and accidental or Friedrich-Wintgen (FW) BIC [90], have been mostly investigated. The former originates from the incompatibility of the symmetry between the resonant mode and external radiation and appears at highly symmetric points such as the Γ point in the reciprocal space of the periodic structure. The latter is formed by the destructive interference between the radiation from the resonant modes [8, 99], where the symmetry is generally not required, and can appear at a point of no symmetry in the reciprocal space.

When the two relevant modes interact in the near field, the dispersion of the modes anti-crosses, and the BIC lies on one of the split branches [90, 91, 100]. In optics, recently, BICs appearing on the anti-crossed branch have been attracting attention and are being discussed [79, 83, 87, 88] for applications such as high-Q super cavities with subwavelength dielectric structures [88]. In the previous chapter ([101]), we presented that, in a dielectric waveguide connected with the far field through a metal grating, the branch at which the BIC appears depends on the polarization of the mode, which is explained by the difference in the parameter describing the coupling phase of the modes with the external radiation, in a consistent manner with the original theory of Friedrich and Wintgen [90]. In this chapter, we show that the branch at which the FW-BIC emerges also depends on the grating thickness. On carefully inspecting the dispersion relation, we found that the position at which the BIC appears is fixed at the crossing of the original waveguide modes, while the coupled resonant modes of the entire system move owing to the change in the grating thickness, thus resulting in the flipping of the BIC branch. We also show that the criteria discussed in our previous chapter for the branch at which the BIC appears still hold. In addition, we observed that the magnitude of the anti-crossing gap, and hence, the internal (near field) coupling, varies with the change in the grating thickness.

In parallel, with the equation of motion of essentially the same form as that describes a system exhibiting the FW-BIC, the dynamics of non-Hermitian systems have been intensively investigated with an emphasis on the presence and the influence of exceptional points (EPs) at which the eigen solutions (resonant modes) formed from more than one oscillator with the mutual coupling coalesce [102]. In optics and photonics, EPs in active or passive parity-time (PT) symmetric structures as well as those in non-PT symmetric structures have attracted a significant amount of interest [9,103] as such systems exhibit various exotic as well as practically important phenomena at or around the EP. For example, asymmetric mode switching [104], directional omni-polarizer [105], laser mode selection [106–108], unidirectional invisibility or reflectionlessness [109], directional total absorption [110], loss-induced transparency [111], polarization control [112], and enhancement of Sagnac sensitivity [113,114] have been proposed and/or demonstrated. They are expected to lead to a new paradigm of optical systems.

Though many of the reports on EPs have dealt with the case of no external (radiation) coupling, which is the origin of the FW-BIC, the EP is expected to appear even with the radiation coupling, and hence, the BIC and EP are closely located in the parameter space [102, 115]. In the last part of this article, we show that the EP can indeed be realized near the BIC point in our device, where the tuning of the internal coupling with the grating thickness plays a significant role. The continuous controllability of the system with the use of such an additional parameter is expected to encourage experimental investigations and the application of the BIC- and EP-related phenomena in optics and photonics [116].

5.2 Device structure and the methods of analysis

The system considered is a dielectric waveguide sandwiched by a metal grating and optically thick backing metal, which is essentially the same structure as that considered in our previous paper [101], as shown in Fig. 5.1. In this paper, we only vary the grating thickness h_{metal} and fix the other parameters. We consider the region of the wavelength where only the 0th order wave is radiative in the air region. For the permittivity of the gold, unless otherwise stated, the Drude-Lorentz model fitting the reported experimental data [53] was used. In some cases, however, we eliminated the imaginary part of the permittivity to neglect the loss and simplify the theoretical analysis. We will specify the elimination when it is done. We consider a case where a P-polarized wave is incident from the air region. Owing to the backing metal, the incident light is totally reflected unless it is absorbed due to the ohmic loss at the metal surface. Strong absorption occurs when the incident light excites the resonant mode, which comprises the waveguide modes in the dielectric region with a modification of the slit-induced internal and external (radiation) coupling. The dominant waveguide modes for the situation considered in this paper are the first (lowest) and second transverse magnetic (TM) modes, TM_0 and TM_1, respectively, in the metal-dielectric-metal (MIM) structure.

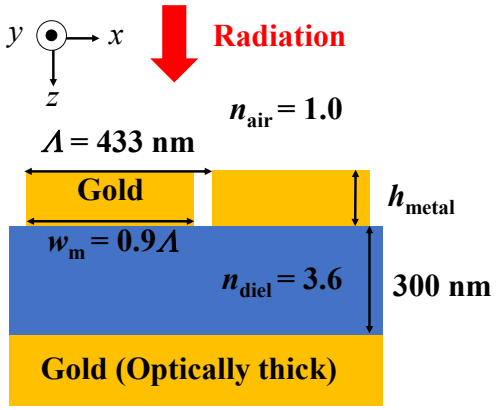

Figure 5.1: Cross-sectional structure of the device considered in this work.

For the analysis of the electromagnetic field and the resonant (eigen) mode in the device, a spatial coupled-mode method (SCMT) [35] was used. In the SCMT, the wave propagation in the grating layer was described by that in a slit sandwiched by the nearby metal bars and the modes were calculated taking into account the permittivity of gold [21, 22]. For the slit width of 43.3 nm considered here, only one propagating mode is present. In addition, a temporal coupled-mode theory (TCMT) [25, 93] was used to analyze the response obtained by the SCMT. It should be noted that the SCMT and TCMT are essentially different from each other; the former is a numerical solver of the EM field based on Maxwell's equations, while the latter is an equation that describes the motion of the oscillators corresponding, in the present case, to the original TM_0 and TM_1 modes with mutual internal and external coupling.

5.3 Absorption spectra and the resonant mode of the system

Figure 5.2 shows the dispersion relation of the absorption for the wave incident from the air region in the gray-scale maps for the four cases of the grating thickness h_{metal}. The solid lines on the absorption map indicate the wavelength corresponding to the real part of the resonant mode frequency. It can be observed that the high-absorption bands appear along the resonant modes. As mentioned above, each resonant mode can be assigned to an originating MIM mode, except in the case of the anti-crossing region wherein the modes are mixed by the slit. In all the cases of the grating thickness, as indicated by the dashed circles, the absorption disappears locally near the anti-crossing. This behavior is a signature of the emergence of the BIC. The imaginary part of the resonant mode frequency is depicted in the lower panel for each h_{metal} with the same colors for each branch as those used for the real part. In the calculation of the resonant modes, the imaginary part of the metal permittivity was set to zero such that the imaginary part of the resonant mode frequency is only due to the radiation loss. The disappearance of the absorption corresponds to the vanishing imaginary part, which confirms that the disappeared mode is indeed the BIC.

There are two remarkable features of the absorption map and resonant mode dispersion. First, the magnitude of the anti-crossing gap depends on h_{metal}. With the increase in h_{metal}, the gap first becomes small and almost diminishes for $h_{\mathrm{metal}} \sim 275$ nm. The gap then reappears with a further increase in h_{metal}. Second, the branch at which the BIC appears changes as h_{metal} crosses ~ 275 nm, where the gap shrinkage occurs. The BIC appears on the lower branch for $h_{\mathrm{metal}} < 275$ nm and on the higher branch for $h_{\mathrm{metal}} > 275$ nm. In the following, we discuss these features in detail, in the order of 1) the position and branch of the BIC and 2) the variation of the anti-crossing gap in Sec. 4 and Sec. 5, respectively.

5.4 Position of the BIC

5.4.1 The position of the BIC in terms of the empty lattice mode

Here, we first discuss the position and the branch of the BIC. In Fig. 5.3, we present a magnified view of Fig. 5.2 near the anti-crossing. The position of the BIC is indicated by the dashed circles. As mentioned above, the BIC appears on the lower (upper) branch for $h_{\mathrm{metal}} < 275$ (> 275) nm. For $h_{\mathrm{metal}} = 275$ nm, the anti-crossing disappears, and the BIC appears at the crossing point. On observing the figure more closely, we notice that the position of the BIC is not moved by the change in h_{metal}. The broken lines plotted in the figures are the empty lattice TM_0 and TM_1 waveguide modes, which were obtained by folding the dispersion curves of these modes in the MIM waveguide with flat metals (no slit) into the first Brillouin Zone. Interestingly and importantly, it

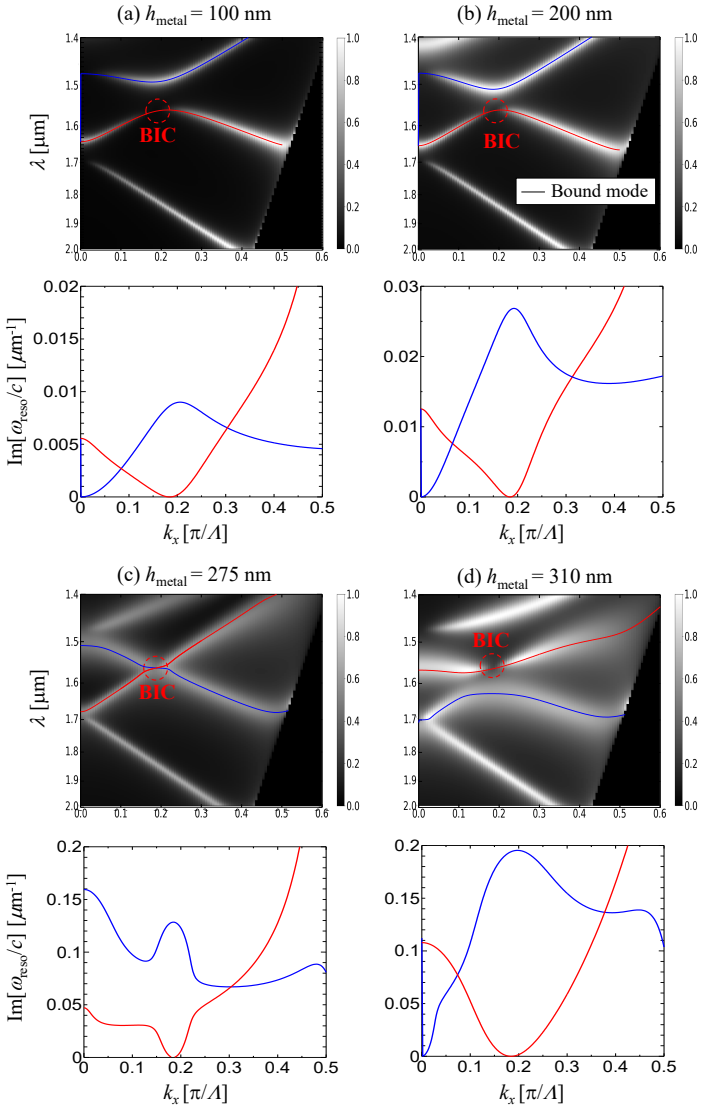

Figure 5.2: Dispersion relation of the absorption and the resonant mode for the four cases of h_{metal}: (a) 100 nm, (b) 200 nm, (c) 275 nm, and (d) 310 nm. In the upper panel, the absorption is depicted by the gray scale along with the wavelength corresponding to the real part of the resonant-mode frequency indicated by the blue and red lines. In the lower panel, the imaginary part of the angular frequency of the resonant mode is plotted using the same color as that used for the same branch in the real part. The frequency was normalized by the speed of the light c in vacuum. It should be noted that the wavelength is given in the inverted scale (linear in frequency). The dashed circles indicate the position of the BIC.

can be clearly observed that the BIC is always located at the crossing point of the two empty lattice bands, which does not move with the change in the grating thickness.

Therefore, the branch inversion of the BIC that is observed in Fig. 5.2 is understood to be a result of the movement of the leaky mode associated with the change in the grating thickness over the BIC point, which is fixed at the crossing of the empty lattice dispersion.

The appearance of the BIC at the crossing point of the empty lattice bands can be explained using the SCMT as follows. For the BIC solution, the radiative fields in the air region become null owing to the nature of the BIC. It can be realized when the fields inside the slit are null, if the slit is single mode as in the present device. In such cases, the fields in the dielectric region satisfy the same relation at the slit/waveguide interface as that of the empty lattice MIM modes, which means that the fields inside the dielectric region are those of the empty lattice modes when the BIC occurs. It should be mentioned that, if the slit is not single mode, the null field in the air region does not mean the null field in the slit and the BIC point can be shifted from the crossing point of the empty lattice.

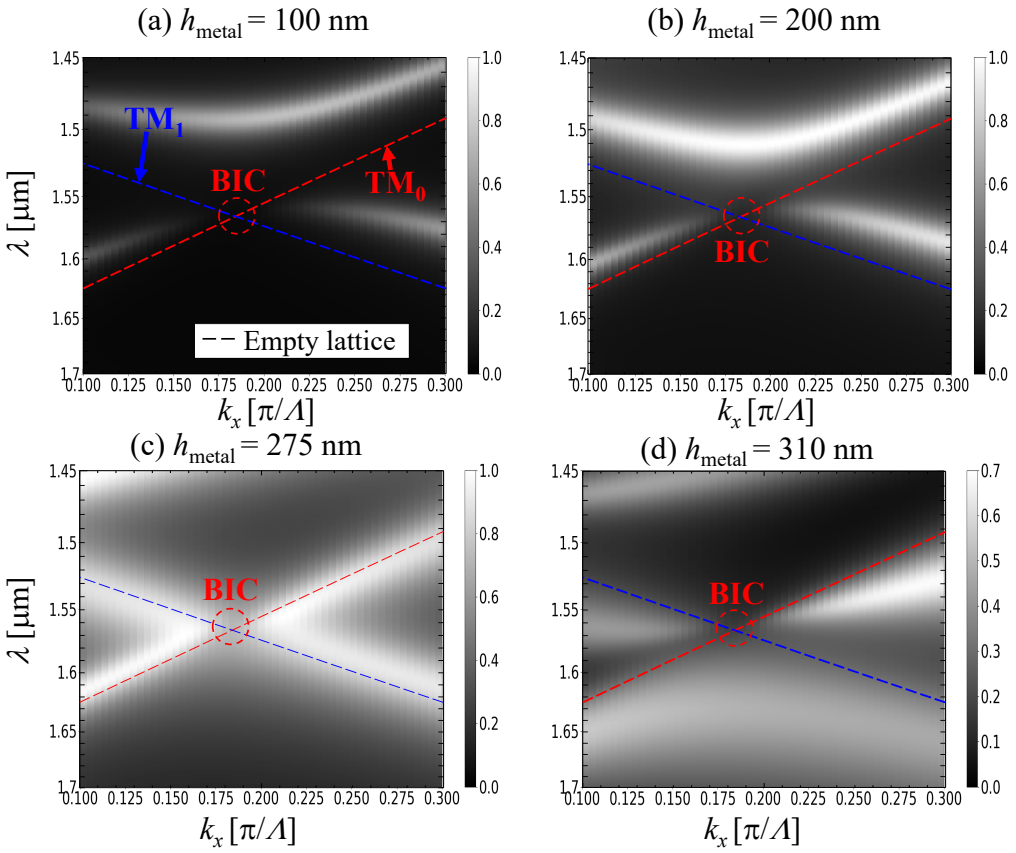

Figure 5.3: Magnified view of the absorption map shown in Fig. 5.2. The dashed circles and dashed lines indicate the position of the BIC and empty lattice bands, respectively

As another method of understanding the system, we calculated the reflection coefficient ρ_{diel} for the wave approaching the slit/dielectric interface from the infinitely thick

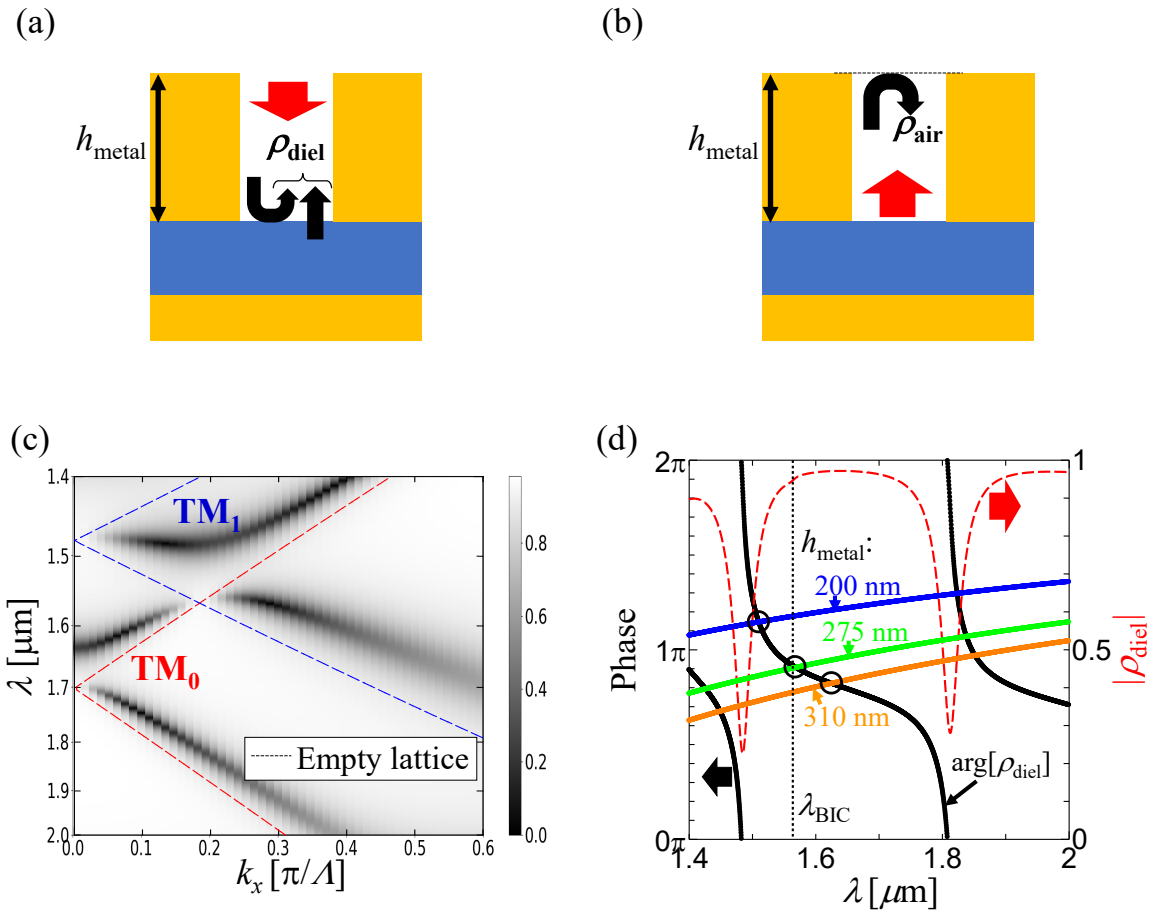

Figure 5.4: (a) Schematic showing the reflection coefficient ρ_{diel} at the slit/dielectric interface for the slit mode. (b) Schematic showing the reflection coefficient ρ_{air} at the slit/air interface for the slit mode. (c) $|\rho_{\text{diel}}|$ as a function of k_x and the wavelength depicted in gray scale. The empty lattice bands of the waveguide are superimposed by the dashed lines. (d) Amplitude (black solid line) and phase (red dashed line) of ρ_{diel} at $k_x = 0.185[\pi/\Lambda]$ for which the BIC appears. The blue, green, and orange lines indicate the value of $\arg(\rho_{\text{diel}})$ required to satisfy Eq. 5.1 for the cases of $h_{\text{metal}} = 200$, 275, and 310 nm, respectively. The solid circle indicates the intersection of these lines and $\arg(\rho_{\text{diel}})$, which gives the FP resonance.

grating as schematically depicted in Fig. 5.4 (a). Figure 5.4 (c) shows the dispersion of $|\rho_{\text{diel}}|$ along with the empty lattice bands (indicated by dashed lines). It can be observed that the anti-crossing of the bands and the BIC occurs and that the BIC is located at the crossing of the empty lattice band, which is not affected by the grating. Then let us elucidate the role of the finite thickness of the grating. Indicated by the black solid line in Fig. 5.4(d) is $\arg(\rho_{\text{diel}})$ as a function of the wavelength for $k_x = 0.185$ $[\pi/\Lambda]$, where

the BIC emerges at $\lambda = 1563$ nm. It should be noted that $\arg(\rho_{\text{diel}})$ is affected only by the radiative mode because the BIC mode is not coupled to the slit as mentioned above. The red dashed line is $|\rho_{\text{diel}}|$. Between the dips in $|\rho_{\text{diel}}|$, which correspond to the coupled TM_0-TM_1 mode at approximately 1500 nm and uncoupled TM_0 mode at approximately 1800 nm, $\arg(\rho_{\text{diel}})$ varies gradually from 2π to 0. The wavelength of the BIC λ_{BIC} is indicated by the vertical dotted line. Now, let us hypothesize that the solution of the radiative mode of the entire system with a grating of finite thickness can be viewed as the Fabry-Perot (FP) resonance for the wave propagating in the slit, which is given by

$$\arg(\rho_{\text{air}}) + \arg(\rho_{\text{diel}}) + 2\beta_{\text{slit}} h_{\text{metal}} = 2\pi m, \tag{5.1}$$

where $\arg(\rho_{\text{air}})$ is the phase of the reflection at the slit/air interface (See Fig. 5.4(b)), β_{slit} is the propagation constant in the slit, and m is an integer. The blue, green, and orange lines in Fig. 5.4(d) indicate the value of $\arg(\rho_{\text{diel}})$ required to satisfy Eq. 5.1 for $h_{\text{metal}} = 200$, 275, and 310 nm, respectively. Hence, the point at which the line for each h_{metal} crosses $\arg(\rho_{\text{diel}})$ (indicated by the black circles) provides the wavelength that satisfies Eq. 5.1. For $h_{\text{metal}} = 200$ nm, the wavelength of the crossing is shorter than λ_{BIC}. This corresponds to Fig. 5.3 (b) where the BIC is located on the longer-wavelength branch. For $h_{\text{metal}} = 275$ nm, the crossing is located near λ_{BIC}, which corresponds to Fig. 5.3 (c). Then, for $h_{\text{metal}} = 310$ nm, the wavelength of the crossing is greater than λ_{BIC}, which corresponds to Fig. 5.3 (d). It can be observed that the wavelength of the radiative mode in Fig. 5.3 at $k_x = 0.185$ $[\pi/\Lambda]$, where the BIC emerges, is predicted very well, which justifies the hypothesis, and that the thickness h_{metal} of the grating can be said to determine the wavelength that satisfies the FP condition in the slit for the radiative (non-BIC) solution. It should be mentioned again that the discussions presented here are valid for the case in which the wave propagation in the slit is in the single mode or only one mode is dominating.

5.4.2 Temporal coupled-mode theory appropriate for the present system

The response of the present device can be analyzed using TCMT in Chapter 2 for the two resonators corresponding to the empty-lattice TM_0 and TM_1 modes with the internal and external coupling. Though the framework is essentially the same as that in a previous chapter, it is necessary to modify $\mathbf{\Omega}$ in order to keep the BIC solutions fixed at the degenerate point of the two basis modes. As presented below, the matrix $\mathbf{\Omega}$ that satisfies this requirement is,

$$\mathbf{\Omega} = \begin{pmatrix} \tilde{\omega}_1 \equiv \omega_1 + p\alpha\sqrt{\frac{\gamma_{e1}}{\gamma_{e2}}} & \alpha \\ \alpha & \tilde{\omega}_2 \equiv \omega_2 + p\alpha\sqrt{\frac{\gamma_{e2}}{\gamma_{e1}}} \end{pmatrix}, \tag{5.2}$$

where $\omega_{1,2}$ and $\gamma_{e1,2}$ are the eigenfrequency and external (radiation) loss of modes 1 or 2, respectively; α is the internal coupling; and p is the phase difference between the

two modes for coupling to the external field. Here, p has the value of either $+1$ or -1; $p = +1$ if the two modes are in phase (no phase difference), and $p = -1$ if the two modes are out of phase (π phase difference) [101]. The modification comprises the addition of $p\alpha\sqrt{\frac{\gamma_{e1}}{\gamma_{e2}}}$ and $p\alpha\sqrt{\frac{\gamma_{e2}}{\gamma_{e1}}}$ to the diagonal terms of $\mathbf{\Omega}$. The matrices

$$\mathbf{\Gamma}_e = \begin{pmatrix} \gamma_{e1} & \gamma_0 \\ \gamma_0 & \gamma_{e2} \end{pmatrix}, \quad \mathbf{D}^{\mathrm{T}} = e^{i\varphi_d} \begin{pmatrix} \sqrt{2\gamma_{e1}} \\ p\sqrt{2\gamma_{e2}} \end{pmatrix}, \tag{5.3}$$

where $\gamma_0 = p\sqrt{\gamma_{e1}\gamma_{e2}}$ represents the radiation coupling and φ_d is an arbitrary phase, are the same as before, and the matrix

$$\mathbf{\Gamma}_i = \begin{pmatrix} \gamma_{i1} & 0 \\ 0 & \gamma_{i2} \end{pmatrix}, \tag{5.4}$$

where $\gamma_{i1,2}$ is the internal loss (in the metal in the present device) of each mode, was included in Eq. 2.17 for generalization. The expression for $\mathbf{D}$ and the off-diagonal terms of $\mathbf{\Gamma}_e$ are derived using the time-reversal symmetry and energy conservation law [25].

For the time dependence of $e^{-i\omega t}$, the eigenfrequencies of the resonant modes are obtained [24, 90, 94, 102] from Eq. 2.17 as the solution of

$$\{\omega - (\tilde{\omega}_1 - i\gamma_{t1})\}\{\omega - (\tilde{\omega}_2 - i\gamma_{t2})\} + (ip\alpha + \sqrt{\gamma_{e1}\gamma_{e2}})^2 = 0 \tag{5.5}$$

where $\gamma_{t1,2} = \gamma_{i1,2} + \gamma_{e1,2}$. The condition for one of the solutions being the BIC can be derived from Eq. 5.5, by assuming that one of the solutions is purely real [101]. On assuming $\gamma_{i1} = \gamma_{i2} = 0$ for simplicity, we obtain the condition

$$\omega_1 = \omega_2 \equiv \omega_0. \tag{5.6}$$

Then, the solutions are

$$\omega = \begin{cases} \omega_0 + p\alpha(\sqrt{\frac{\gamma_{e1}}{\gamma_{e2}}} + \sqrt{\frac{\gamma_{e2}}{\gamma_{e1}}}) - i(\gamma_{e1} + \gamma_{e2}) \\ \omega_0 \end{cases}. \tag{5.7}$$

The first solution is radiative (leaky) with the loss $\gamma_{e1} + \gamma_{e2}$, and the second solution is the BIC, which has no imaginary part. Thus, the formulation is confirmed to provide the BIC that always lies at the crossing point of the original eigenfrequencies, $\omega_0 = \omega_1 = \omega_2$.

5.4.3 Prediction of BIC-branch in terms of $p\alpha$

In the preceding subsections, we showed that the BIC appears at the crossing point of the empty-lattice modes. In our previous report [101], we showed that the branch at which the BIC appears is determined by the sign of $p\alpha$. Herein, we show that the aforementioned rule still holds. In the TCMT analysis, as observed in Eq. 5.7, the branches at which the BIC appears are determined as follows:

$$p\alpha \quad \begin{cases} > 0 & \text{(lower branch)} \\ < 0 & \text{(upper branch)} \end{cases}, \tag{5.8}$$

as in the case without modification [101]. Therefore, we check sign($p\alpha$) for the cases of $h_{\text{metal}} < 275$ nm and $h_{\text{metal}} > 275$ nm, where the BIC appears at the upper and lower branches, respectively, as shown in Fig. 5.2 or Fig. 5.3.

The evaluation of sign$\{p\alpha\}$ was conducted in the same manner as before [101], i. e. by expanding the electromagnetic fields inside the dielectric waveguide of the empty-lattice waveguide modes. In the present case, the dominant modes are the right-propagating TM_0 and the left propagating TM_1 modes near the anti-crossing point. Sign(p) and sign(α) are then evaluated from the complex amplitude of each mode obtained in the expansion. Sign(p) is evaluated directly from the phase difference between the complex amplitudes. Figure 5.5(a) and (b) show the calculated phase difference at $k_x = 0.1839[\pi/\Lambda]$, which is slightly displaced from the point at which the BIC emerges, for $h_{\text{metal}} = 200$ nm and 310 nm, respectively. At approximately $\lambda =$ 1550nm, the phase is disturbed because the coupled resonance is excited. However, the phase converges to 0 far away from the resonant wavelength in both cases. Therefore, it can be concluded that $p = 1$ in both cases.

Sign(α) is evaluated based on the phase difference between the amplitudes at the two solutions of the coupled resonant mode with the upper (ω_+) and lower (ω_-) frequencies, as the coupled mode oscillation is viewed as the bonding or anti-bonding solution depending on the sign of the coupling constant α. The phase difference for $h_{\text{metal}} = 200$ nm and 310 nm are summarized in Table. 5.1. For $h_{\text{metal}} = 200$ nm, the two modes are in phase (out of phase) at ω_+ (ω_-), which corresponds to $\alpha > 0$, while for $h_{\text{metal}} = 310$ nm, the two modes are out of phase (in phase) at ω_+ (ω_-), which corresponds to $\alpha < 0$. Therefore, we can conclude that $p\alpha$ is positive for $h_{\text{metal}} = 200$ nm and negative for $h_{\text{metal}} = 310$ nm, which confirms that the criteria of Eq. 5.8 are satisfied. We can also say that the sign($p\alpha$) is controlled by the grating thickness.

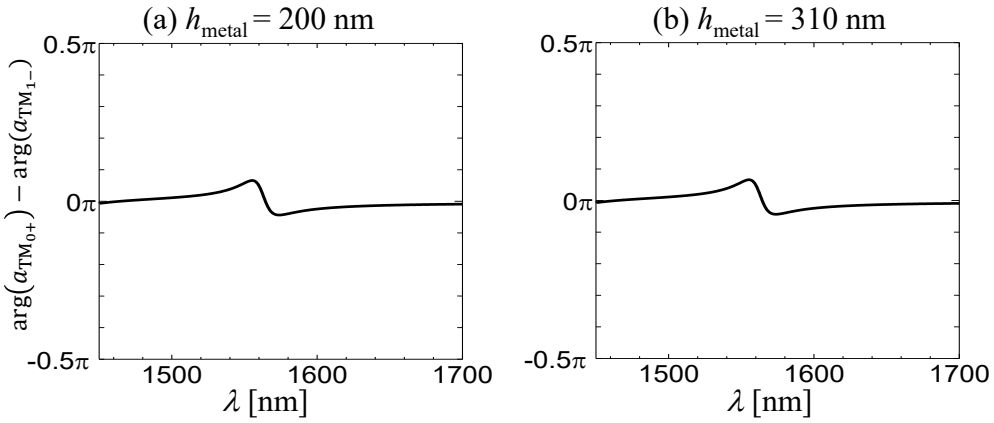

Figure 5.5: Phase difference between the amplitudes of the two waveguide modes near the anti-crossing ($k_x = 0.1839[\pi/\Lambda]$) as a function of wavelength. (a) $h_{\text{metal}} = 200$ nm and (b) $h_{\text{metal}} = 310$ nm.

Table 5.1: Phase difference between the amplitudes of the two waveguide modes near the anti-crossing ($k_x = 0.1839[\pi/\Lambda]$) at the two coupled resonant modes ω_+ and ω_-. (a) $h_{\text{metal}} = 200$ nm and (b) $h_{\text{metal}} = 310$ nm.

(a) Phase difference for $h_{\text{metal}} = 200$ nm

$[\arg(a_{TM1-}) - \arg(a_{TM0+})](\omega_+)$	$[\arg(a_{TM1-}) - \arg(a_{TM0+})](\omega_-)$	$\text{sign}(\alpha)$	p
$5.982 \times 10^{-3}\pi$	1.001π	+	1

(b) Phase difference for $h_{\text{metal}} = 310$ nm

$[\arg(a_{TM1-}) - \arg(a_{TM0+})](\omega_+)$	$[\arg(a_{TM1-}) - \arg(a_{TM0+})](\omega_-)$	$\text{sign}(\alpha)$	p
1.001π	$-6.063 \times 10^{-2}\pi$	–	1

5.5 Variation of the anti-crossing gap and the emergence of exceptional point

5.5.1 Grating thickness dependence of the anti-crossing gap

In this section, we discuss the second feature of the device, namely the variation of the anti-crossing gap with the change of the grating thickness, h_{metal}. As seen in Eq. 5.7, the difference in the real part of the angular frequency $\text{Re}\{\Delta\omega\}$ between the non-BIC (radiating) and the BIC solutions is

$$\text{Re}\{\Delta\omega\} = \frac{p\alpha}{2}\left(\sqrt{\frac{\gamma_{e1}}{\gamma_{e2}}} + \sqrt{\frac{\gamma_{e2}}{\gamma_{e1}}}\right). \tag{5.9}$$

Here, as mentioned above, $p = 1$ and $\text{sign}(\alpha)$ depends on h_{metal}. Although the radiation losses, γ_{e1} and γ_{e2}, are not exactly equal in our device, they are not much different, which can be observed from the linewidth of the two bright lines in Fig. 5.2. Therefore, we evaluate the value $p\alpha$ using an approximated relation $p\alpha = \Delta\omega$, where $\Delta\omega$ is evaluated based on the real part of the resonant-mode frequencies at $k_x = 0.185$ $[\pi/\Lambda]$, where the BIC appears. The result is shown in Fig. 5.6, where $\text{sign}(\alpha)$ was selected according to the result presented in Sec. 5.4.3. The value of $p\alpha$ decreases as h_{metal} increases and crosses zero at approximately $h_{\text{metal}} = 275$ nm.

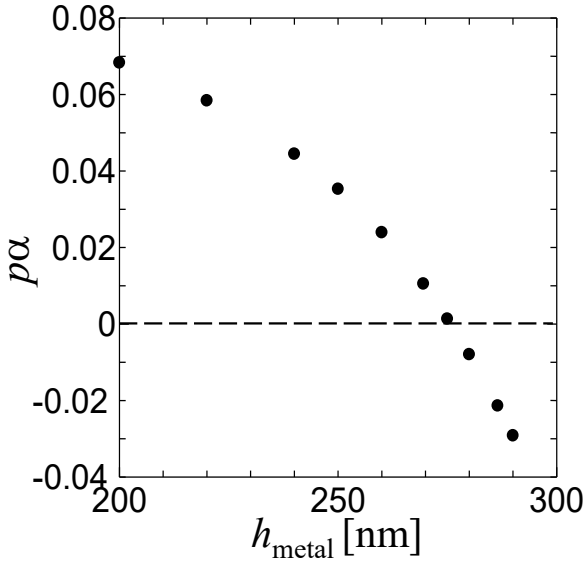

Figure 5.6: Value of $p\alpha$ as a function of the grating thickness calculated using Eq. 5.9. Here $p = 1$ and the sign(α) were selected in accordance with the result obtained in Sec. 4.3.

5.5.2 Emergence of the exceptional point

Recently, with the same type of equation of motion as the TCMT (Eq. 2.17) used above, the physics and the application of EPs in optics and photonics have been intensively investigated [9,103]. Hence, it is interesting to consider the possibility of the realization of EP in the device considered here. The eigenfrequencies of the system are obtained [24,102] as the solution of Eq. 5.5.

$$\omega = \frac{(\tilde{\omega}_1 + \tilde{\omega}_2) - i(\gamma_{t1} + \gamma_{t2}) \pm \sqrt{D}}{2}, \tag{5.10}$$

where

$$D \equiv \{(\tilde{\omega}_1 - \tilde{\omega}_2)^2 - (\gamma_{t1} - \gamma_{t2})^2 + 4(\alpha^2 - \gamma_0^2)\} - i2\{(\tilde{\omega}_1 - \tilde{\omega}_2)(\gamma_{t1} - \gamma_{t2}) + 4\alpha\gamma_0\}. \tag{5.11}$$

The EP, where both the real and imaginary parts of the eigenfrequency coalesce, is realized when D becomes zero, i.e., $\mathrm{Re}\{D\} = \mathrm{Im}\{D\} = 0$. $\mathrm{Im}\{D\} = 0$ presents the following condition.

$$\omega_1 - \omega_2 = -\frac{4\alpha\gamma_0}{\gamma_{t1} - \gamma_{t2}} - p\alpha\left(\sqrt{\frac{\gamma_{e1}}{\gamma_{e2}}} + \sqrt{\frac{\gamma_{e2}}{\gamma_{e1}}}\right), \tag{5.12}$$

for which

$$\mathrm{Re}\{D\} = \frac{\{(\gamma_{t1} - \gamma_{t2})^2 + 4\gamma_0^2\}\{4\alpha^2 - (\gamma_{t1} - \gamma_{t2})^2\}}{(\gamma_{t1} - \gamma_{t2})^2} \tag{5.13}$$

becomes zero when $4\alpha^2 = (\gamma_{t1} - \gamma_{t2})^2$. The condition for the EP is then expressed as

$$|\gamma_{t1} - \gamma_{t2}| = 2|\alpha|, \tag{5.14}$$

$$\omega_1 - \omega_2 = \pm 2\gamma_0 - p\alpha\left(\sqrt{\frac{\gamma_{e1}}{\gamma_{e2}}} + \sqrt{\frac{\gamma_{e2}}{\gamma_{e1}}}\right) = p\sqrt{\gamma_{e1}\gamma_{e2}}\left\{\pm 2 - \alpha\left(\frac{1}{\gamma_{e2}} - \frac{1}{\gamma_{e1}}\right)\right\}. \tag{5.15}$$

In our device, $\omega_1 - \omega_2$ in Eqs. 5.12 or 5.15 are selected based on k_x. The effect of the radiation loss $\gamma_{e1,2}$ and the radiation coupling γ_0 appears only in the form of the shift of the conditions.

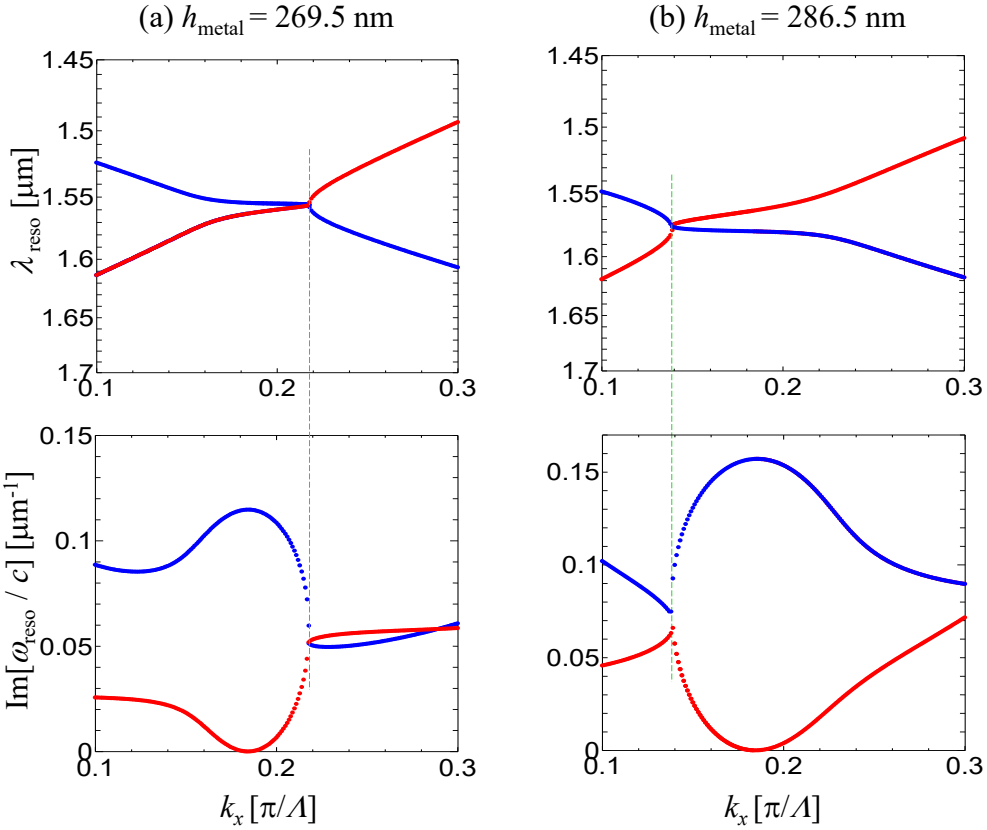

Figure 5.7: Real (upper) and imaginary (lower) parts of the coupled resonant modes for (a)h_{metal} = 269.5 nm and (b)h_{metal} = 286.5 nm. The real part is given by the corresponding wavelength . For each h_{metal}, there exists a point at which the real and imaginary parts coalesce, which indicates the EP.

Let us neglect the internal loss for the purpose of simplicity, i. e. $\gamma_{t1,2} = \gamma_{e1,2}$. Although it is difficult to evaluate precisely the values of $\gamma_{e1,2}$ in the specific structure, $|\alpha|$ can be tuned by changing the grating thickness h_{metal} as shown in Fig. 5.6. Therefore, we can identify a case where the EP emerges on varying h_{metal}. In Fig. 5.7, we show the dispersion relation of the resonant mode frequency for h_{metal} = 269.5 nm and 286.5

nm, for which the coalescence of both the real and imaginary parts are observed at $k_x = 0.217[\pi/\Lambda]$ and $k_x = 0.140[\pi/\Lambda]$, respectively, thus demonstrating that the EPs are generated as expected. Although not demonstrated here, the EP does not appear for other h_{metal}. For the two cases of h_{metal} for which the EP is realized, α is evaluated based on Fig. 5.6, and the values of $\gamma_{e1,2}$ are then estimated by the fitting of the k_x-dependent eigenfrequencies of the TCMT to those of the SCMT. The results are $\alpha/c = 0.01$ [$1/\mu$m], $\gamma_{e1}/c = 0.05$ [$1/\mu$m], and $\gamma_{e2}/c = 0.07$ [$1/\mu$m] for $h_{\mathrm{metal}} = 269.5$ nm and $\alpha = -0.02/c$ [$1/\mu$m], $\gamma_{e1}/c = 0.06$ [$1/\mu$m], and $\gamma_{e2}/c = 0.1$ [$1/\mu$m] for $h_{\mathrm{metal}} = 286.5$ nm, where c is the speed of light in vacuum. Therefore, in the present case, Eq. 5.15 is approximated as

$$\omega_1 - \omega_2 \simeq \pm 2\gamma_0, \tag{5.16}$$

which causes the EPs to appear at k_x in a manner nearly symmetrical with respect to the crossing point of the empty lattice modes, and hence, the BIC point, which is consistent with Fig. 5.7.

Eq. 5.13 suggests that the eigenfrequencies have a split real part and degenerated imaginary part for $4\alpha^2 > (\gamma_{t1} - \gamma_{t2})^2$, which corresponds to the effective (passive) PT symmetric case and a split imaginary part and degenerated real part for $4\alpha^2 < (\gamma_{t1} - \gamma_{t2})^2$, which corresponds to the broken (effective) PT case [116], provided that Eq. 5.12 is satisfied. For the present device, we can observe the latter case for 269.5 nm $< h_{\mathrm{metal}} <$ 286.5 nm at a point between $0.217\ [\pi/\Lambda] > k_x > 0.140\ [\pi/\Lambda]$ and the former case outside these regions. Moreover, the structure presented here is suitable for the introduction of the gain as the pumping can be performed either optically through the slit or electrically through the grating and back metal. In either case of with or without gain, the tunability of the parameter α in our structure is expected to be useful in the control of the device. Lastly, we highlight that the control of α, which is realized in this study by controlling the grating thickness, can be realized using non-built-in methods. As discussed in Sec. 5.4.1, the dependence of the resonant mode of the entire system, and hence, α, on the grating thickness can be attributed to the change in the FP resonance in the slit. Therefore, we can expect that α can be varied by filling the slit with a dielectric or applying a voltage between the neighboring metal bars of the grating when the slit is filled with an electro-optical material. The latter method, if realized, would be particularly useful.

5.6 Summary

In this paper, we reported the emergence of the FW-BIC and EP in a dielectric waveguide comprising a metal grating, while focusing on their dependence on the grating thickness. For any grating thickness, the BIC emerges at one of the branches near the anti-crossing formed from the two waveguide modes TM_0 and TM_1 with internal (near field) and external (radiation) coupling via the slit of the grating. It was determined that, with a change in the thickness, the coupled modes move with the varying anti-

crossing gap. The gap diminishes at a certain thickness, and the branch at which the BIC appears flips. The change in the anti-crossing gap corresponds to the change in the internal coupling constant.

We showed that, when the slit is narrow to support single-mode propagation, the branch and position of the FW-BIC is determined by a simple rule: the FW-BIC appears at the crossing point between the two waveguide modes in the empty-lattice (zero slit-width) limit. In addition, these results are consistent with the criteria for the branch at which the BIC appears based on the phase of each basis mode presented in our previous paper. Owing to the dependence of the internal coupling on the grating thickness, we can find the cases in which the EP appears in the same device based only on the selection of the grating thickness, consistently with the prediction. As the dependence of the anti-crossing gap on the grating thickness can be understood in terms of the FP resonance in the slit, tuning could be performed using other methods such as the voltage applied to the metal grating with the slit filled by an electro-optical material. The BIC and EP in the dielectric waveguide comprising a metal grating, particularly with such tunability, are expected to result in the development of functional and high-performance optical and photonic devices as well as to become a platform for the fundamental research of non-Hermitian systems.

Chapter 6

Summary and conclusion of this work

In conclusion, we have investigated the peculiar optical responses of metal grating theoretically. As the system, we considered the grating is placed on dielectric substrate or multimode waveguide, which are important for the applications. The summary of work is shown as follows.

In chapter 3, the optical properties of a metal grating on the high refractive index substrate were investigated. Especially, the difference of the optical response with or without the presence of the substrate was discussed. The peak was observed in the transmittance and electric field enhancement spectra, which corresponded to the bound mode of the system. Furthermore, the bound mode corresponds to FP resonant condition of the slit. As a most distinct feature of the metal grating on the substrate, the bound mode disappears when the grating is thin and corresponding peak of enhancement and transmittance also disappears.

In chapter 4 and 5, the peculiar phenomena were observed on the composite structure; metal grating placed on the multi-mode waveguide system were discussed. In this structure, the BIC was observed. The feature of the BIC observed in this structure is that the BIC lies on one of the anti-crossed branches, and the branch on which the BIC lies is different depending on the polarization.

In addition to the polarization, the BIC branch changed depending on the grating thickness. By the TCMT, the branch selection effect was explained by the two factors; phase difference of the internal coupling of two modes and the difference of phase change of two modes in coupling to the external field, which we denoted as $p\alpha$, determine the branch of the BIC.

Finally, the EP was observed at a certain grating thickness. Using the TCMT, the EP appeared because the difference of the (uncoupled) radiation losses of the two modes became comparable to the internal coupling coefficient of two modes. Similar to chapter 3, the FP condition of the slit corresponded to the variation of the anti-crossed gap level.

As a whole, the theoretical study to elucidate the mechanisms of the peculiar optical

responses of metal grating was greatly advanced. The behavior of anomalies and other peculiar phenomena such as the BIC and EP were explained very reasonably and simply by using SCMT and TCMT. We note that the EP on the grating/dielectric waveguide structure was discovered for the first time in this work.

The findings of this work may pave the new application using metal grating. First, the band gap level of the anti-crossed band varied depending on the grating thickness, and eventually, the branch on which BIC lies inverted. The dispersion of the anti-crossed bands corresponded to the FP condition of the slit. This implies that the band gap level or the branch of the BIC could be changed by filling some dielectric material or by changing the dielectric constant of the material placed within the slit by applying a voltage to the grating instead of varying the grating thickness. This may realize the sensing device or novel optical device that can be controlled by voltage. The advantage of the voltage control that it enables very fast modulation. Furthermore, using a similar way, the EP could be controlled. Although there has not been considered yet what kind of practical application is realized on this structure using EP, some practical application such as unidirectional reflection was proposed using EP recently. With the development of the study of the EP, the new application on this simple system might be realized.

Bibliography

[1] Born M and Wolf E (2013). *Principles of optics: electromagnetic theory of propagation, interference and diffraction of light.* Elsevier

[2] Joannopoulos J D, Villeneuve P R and Fan S. (1997). Photonic crystals: putting a new twist on light. Nature, 386(6621), 143

[3] Yu N, Genevet P, Kats M A, Aieta F, Tetienne J P, Capasso F and Gaburro Z. (2011). Light propagation with phase discontinuities: generalized laws of reflection and refraction. science, 334(6054), 333-337

[4] Barnes W L, Dereux A and Ebbesen T W. (2003). Surface plasmon subwavelength optics. nature, 424(6950), 824

[5] Yablonovitch E. (1987). Inhibited spontaneous emission in solid-state physics and electronics. Physical review letters, 58(20), 2059

[6] Khorasaninejad M and Capasso F. (2017). Metalenses: Versatile multifunctional photonic components. Science, 358(6367), eaam8100

[7] Ebbesen T W, Lezec H J, Ghaemi H F, Thio T and Wolff P A (1998). Extraordinary optical transmission through sub-wavelength hole arrays. Nature, 391(6668), 667

[8] Hsu C W, Zhen B, Stone A D, Joannopoulos J D and Soljačić M (2016). Bound states in the continuum. Nature Reviews Materials, 1(9), 16048

[9] Miri M A and Alù A (2019). Exceptional points in optics and photonics. Science, 363(6422), eaar7709

[10] Bethe H A (1944). Theory of diffraction by small holes. Physical review, 66(7-8), 163

[11] Marinica D C, Borisov A G and Shabanov S V (2008). Bound states in the continuum in photonics. Physical review letters, 100(18), 183902

[12] von Neumann J and Wigner E (1929). ́Uber merkwrdige diskrete Eigenwerte. Zh. Phys. 30, 465-470

[13] Wood R W (1902). On a remarkable case of uneven distribution of light in a diffraction grating spectrum. Proceedings of the Physical Society of London, 18(1), 269

[14] Rayleigh L (1907). On the dynamical theory of gratings. Proceedings of the Royal Society of London. Series A, Containing Papers of a Mathematical and Physical Character, 79(532), 399-416

[15] Fano U (1941). The theory of anomalous diffraction gratings and of quasi-stationary waves on metallic surfaces (Sommerfeld's waves). JOSA, 31(3), 213-222

[16] Hessel A and Oliner A A (1965). A new theory of Wood's anomalies on optical gratings. Applied optics, 4(10), 1275-1297

[17] Ritchie R H, Arakawa E T, Cowan J J and Hamm R N (1968). Surface-plasmon resonance effect in grating diffraction. Physical Review Letters, 21(22), 1530

[18] Schröter U and Heitmann D (1998). Surface-plasmon-enhanced transmission through metallic gratings. Physical review B, 58(23), 15419

[19] Cao Q and Lalanne P (2002). Negative role of surface plasmons in the transmission of metallic gratings with very narrow slits. Physical Review Letters, 88(5), 057403

[20] Yoon J W, Lee J H, Song S H and Magnusson R (2014). Unified theory of surface-plasmonic enhancement and extinction of light transmission through metallic nanoslit arrays. Scientific reports, 4, 5683

[21] Nishida M, Hatakenaka N and Kadoya Y (2015). Multipole surface plasmons in metallic nanohole arrays. Physical Review B, 91, 235406

[22] Kikkawa R, Nishida M and Kadoya Y (2017). Substrate effects on the optical properties of metal gratings. JOSA B 34 (12) 2578-85

[23] Garcia-Vidal F J and Martin-Moreno L (2002). Transmission and focusing of light in one-dimensional periodically nanostructured metals. Physical Review B, 66(15), 155412

[24] Volya A and Zelevinsky V (2003). Non-Hermitian effective Hamiltonian and continuum shell model. Physical Review C, 67(5), 054322

[25] Suh W, Wang Z and Fan S (2004). Temporal coupled-mode theory and the presence of non-orthogonal modes in lossless multimode cavities. IEEE Journal of Quantum Electronics, 40(10), 1511-1518

[26] J. A. Porto, F. J. García-Vidal, and J. B. Pendry, "Transmission resonances on metallic gratings with very narrow slits," Phys. Rev. Lett. 83, 2845–2848 (1999).

[27] S. Collin, F. Pardo, R. Teissier, and J.-L. Pelouard, "Strong discontinuities in the complex photonic band structure of transmission metallic gratings," Phys. Rev. B 63, 033107 (2001).

[28] F. J. García-Vidal and L. Martín-Moreno, "Transmission and focusing of light in one-dimensional periodically nanostructured metals," Phys. Rev. B 66, 155412 (2002).

[29] P. Lalanne, C. Sauvan, J. P. Hugonin, J. C. Rodier, and P. Chavel, "Perturbative approach for surface plasmon effects on flat interfaces periodically corrugated by subwavelength apertures," Phys. Rev. B 68, 125404 (2003).

[30] F. Marquier, J.-J. Greffet, S. Collin, F. Pardo, and J. L. Pelouard, "Resonant transmission through a metallic film due to coupled modes," Opt. Express 13, 70–76 (2005).

[31] D. Crouse and P. Keshavareddy, "Role of optical and surface plasmon modes in enhanced transmission and applications," Opt. Express 13, 7760–7771 (2005).

[32] H. Liu and P. Lalanne, "Microscopic theory of the extraordinary optical transmission," Nature 452, 728–731 (2008).

[33] B. Sturman, E. Podivilov, and M. Gorkunov, "Theory of extraordinary light transmission through arrays of subwavelength slits," Phys. Rev. B 77, 075106 (2008).

[34] S. Collin, G. Vincent, R. Haïdar, N. Bardou, S. Rommeluere, and J.-L. Pelouard, "Nearly perfect Fano transmission resonances through nanoslits drilled in a metallic membrane," Phys. Rev. Lett. 104, 027401 (2010).

[35] F. J. García-Vidal, L. Martín-Moreno, T. W. Ebbesen, and L. Kuipers, "Light passing through subwavelength apertures," Rev. Mod. Phys. 82, 729–787 (2010).

[36] M. Guillaumée, L. A. Dunbar, and R. P. Stanley, "Description of the modes governing the optical transmission through metal gratings," Opt. Express 19, 4740–4755 (2011).

[37] T. Søndergaard, S. I. Bozhevolnyi, J. Beermann, S. M. Novikov, E. Devaux, and T. W. Ebbesen, "Extraordinary optical transmission with tapered slits: effect of higher diffraction and slit resonance orders," J. Opt. Soc. Am. B 29, 130–137 (2012).

[38] J. W. Yoon, M. J. Jung, S. H. Song, and R. Magnusson, "Analytic theory of the resonance properties of metallic nanoslit arrays," IEEE J. Quantum Electron. 48, 852–861 (2012).

[39] M. Sarrazin, J.-P. Vigneron, and J.-M. Vigoureux, "Role of Wood anomalies in optical properties of thin metallic films with a bidimensional array," Phys. Rev. B 67, 085415 (2003).

[40] C. Genet, M. P. van Exter, and J. P. Woerdman, "Fano-type interpretation of red shifts and red tails in hole array transmission spectra," Opt. Commun. 225, 331–336 (2003).

[41] S. Savoia, A. Ricciardi, A. Crescitelli, C. Granata, E. Esposito, V. Galdi, and A. Cusano, "Surface sensitivity of Rayleigh anomalies in metallic nanogratings," Opt. Express 21, 23531–23542 (2013).

[42] R. W. Wood, "Anomalous diffraction gratings," Phys. Rev. 48, 928–936 (1935).

[43] D. Okamoto, J. Fujikata, K. Nishi, and K. Ohashi, "Numerical study of near-infrared photodetectors with surface-plasmon antenna for optical communication," Jpn. J. Appl. Phys. 47, 2921–2923 (2008).

[44] A. Karar, N. Das, C. L. Tan, K. Alameh, Y. T. Lee, and F. Karouta, "High-responsivity plasmonics-based GaAs metal-semiconductormetal photodetectors," Appl. Phys. Lett. 99, 133112 (2011).

[45] S. Y. Chou and M. Y. Liu, "Nanoscale terahertz metal-semiconductormetal photodetectors," IEEE J. Quantum Electron. 28, 2358–2368 (1992).

[46] S.-G. Park, K. H. Jin, M. Yi, J. C. Ye, J. Ahn, and K.-H. Jeong, "Enhancement of terahertz pulse emission by optical nanoantenna," ACS Nano 6, 2026–2031 (2012).

[47] C. W. Berry and M. Jarrahi, "Terahertz generation using plasmonic photoconductive gratings," New J. Phys. 14, 105029 (2012).

[48] B. Heshmat, H. Pahlevaninezhad, Y. Pang, M. Masnadi-Shirazi, R. B. Lewis, T. Tiedje, R. Gordon, and T. E. Darcie, "Nanoplasmonic terahertz photoconductive switch on GaAs," Nano Lett. 12, 6255–6259 (2012).

[49] A. Jooshesh, V. Bahrami-Yekta, J. Zhang, T. Tiedje, T. E. Darcie, and R. Gordon, "Plasmon-enhanced below bandgap photoconductive terahertz generation and detection," Nano Lett. 15, 8306–8310 (2015).

[50] N. T. Yardimci and M. Jarrahi, "High sensitivity terahertz detection through large-area plasmonic nano-antenna arrays," Sci. Rep. 7, 42667 (2017).

[51] R.-L. Chern, Y.-T. Chen, and H.-Y. Lin, "Anomalous optical absorption in metallic gratings with subwavelength slits," Opt. Express 18, 19510–19521 (2010).

[52] X. Chen, X. Yan, P. Li, Y. Mou, W. Wang, Z. Guan, and H. Xu, "Mechanism of resonant perfect optical absorption in dielectric film supporting metallic grating structures," Opt. Express 24, 19435–19447 (2016).

[53] P. B. Johnson and R. W. Christy, "Optical constants of the noble metals," Phys. Rev. B 6, 4370–4379 (1972).

[54] Koshelev K, Favraud G, Bogdanov A, Kivshar Y and Fratalocchi A 2019 Non-radiating photonics with resonant dielectric nanostructures *Nanophotonics* **8** (5) 725-45

[55] Lyapina A A, Maksimov D N, Pilipchuk A S and Sadreev A F 2015 Bound states in the continuum in open acoustic resonators *J. Fluid. Mech.* **780** 370-387

[56] Sadreev A F, Pilipchuk A S, and Lyapina A A 2017 Tuning of Fano resonances by rotation of continuum: Wave faucet *EPL* **117** 50011

[57] Lyapina A A, Pilipchuk A S, and Sadreev A F 2018 Trapped modes in a non-axisymmetric cylindrical waveguide *J. Sound Vib.* **421** 48-60

[58] Linton C M, and McIver P. 2007 Embedded trapped modes in water waves and acoustics *Wave motion* **45** (1-2) 16-29

[59] Cobelli P J, Pagneux V, Maurel A and Petitjeans P 2011 Experimental study on water-wave trapped modes *J. Fluid Mech.* **666** 445-76

[60] Koshelev K, Lepeshov S, Liu M, Bogdanov A and Kivshar Y 2018 Asymmetric metasurfaces with high-Q resonances governed by bound states in the continuum *Phys. Rev. Lett.* **121** 193903

[61] Fan K, Shadrivov I V and Padilla W J 2019 Dynamic bound states in the continuum *Optica* **6** (2) 169-73

[62] Cong L and Singh R 2019 Symmetry protected Dual Bound States in the Continuum in Metamaterials *Adv. Opt. Mat.* **7** 1900383.

[63] Paddon P and Young J F 2000 Two-dimensional vector-coupled-mode theory for textured planar waveguides *Phys. Rev. B* **61** (3) 2090

[64] Hsu C W, Zhen B, Chua S, Johnson S G, Joannopoulos J D and Soljačić M 2013 Bloch surface eigenstates within the radiation continuum *Light: Science & Applications* **2** (7) e84

[65] Hsu C W, Zhen B, Lee J, Chua S L, Johnson S G, Joannopoulos J D and Soljačić M 2013 Observation of trapped light within the radiation continuum *Nature* **499** 10188

[66] Foley J M, Young S M and Phillips J D 2014 Symmetry-protected mode coupling near normal incidence for narrow-band transmission filtering in a dielectric grating *Phys. Rev. B* **89** 165111

[67] Yang Y, Peng C, Liang Y, Li Z and Noda S 2014 Analytical perspective for bound states in the continuum in photonic crystal slabs *Phys. Rev. Lett.* **113** 037401

[68] Yoon J W, Song S H and Magnusson R. 2015 Critical field enhancement of asymptotic optical bound states in the continuum *Sci. Rep.* **5** 18301

[69] Li L and Yin H 2016 Bound States in the Continuum in double layer structures *Sci. Rep.* **6** 26988

[70] Blanchard C, Hugonin J P and Sauvan C 2016 Fano resonances in photonic crystal slabs near optical bound states in the continuum *Phys. Rev. B* **94** 155303

[71] Wang Y, Song J, Dong L and Lu M 2016 Optical bound states in slotted high-contrast gratings *J. Opt. Soc. Am. B* **33** 122472

[72] Ni L, Wang Z, Peng C and Li Z 2016 Tunable optical bound states in the continuum beyond in-plane symmetry protection *Phys. Rev. B* **94** 245148

[73] Wang T and Zhang S 2018 Large enhancement of second harmonic generation from transition-metal dichalcogenide monolayer on grating near bound states in the continuum *Opt. Exp.* **26** (1) 322-337

[74] Sadrieva Z F, Sinev I S, Koshelev K L, Samusev A, Iorsh I V, Takayama O, Malureanu R, Bogdanov A A and Lavrinenko A V 2017 Transition from optical bound states in the continuum to leaky resonances: role of substrate and roughness *ACS Photonics* **4** (4) 723-27

[75] Bulgakov E N, Maksimov D N, Semina P N and Skorobogatov S A 2018 Propagating bound states in the continuum in dielectric gratings *JOSA B* **35** (6) 1218-22

[76] Romano S, Zito G, Torino S, Calafiore G, Penzo E, Coppola G, Cabrini S, Rendina I and Mocella V 2018 Label-free sensing of ultralow-weight molecules with all-dielectric metasurfaces supporting bound states in the continuum *Photonics Research* **6** 726-33

[77] Krasikov S D, Bogdanov A A and Iorsh I V 2018 Nonlinear bound states in the continuum of a one-dimensional photonic crystal slab *Phys. Rev. B* **97** 224309

[78] Koshelev K L, Sychev S K, Sadrieva Z F, Bogdanov A A and Iorsh I V 2018 Strong coupling between excitons in transition metal dichalcogenides and optical bound states in the continuum *Phys. Rev. B* 98 161113

[79] Bulgakov E N and Maksimov D N 2018 Avoided crossings and bound states in the continuum in low-contrast dielectric gratings *Phys. Rev. A* **98** 053840

[80] Wang H F, Gupta S K, Zhu X Y, Lu M H, Liu X P and Chen Y F 2018 Bound states in the continuum in a bilayer photonic crystal with TE-TM cross coupling *Phys. Rev. B* **98** 214101

[81] Mermet-Lyaudoz R, Dubois F, Hoang N, Drouard E, Berguiga L, Seassal C, Letartre X, Viktorovitch P and Nguyen H S 2019 Realization of Bound state In the Continuum induced by vertical symmetry breaking in photonic lattice arXiv preprint arXiv:1905.03868

[82] Zhang J, Kosugi Y, Otomo A, Nakano Y, and Tanemura T 2017 Active metasurface modulator with electro-optic polymer using bimodal plasmonic resonance *Opt. Exp.* **25** (24) 30304-311

[83] Azzam S I, Shalaev V M, Boltasseva A and Kildishev A V 2018 Formation of bound states in the continuum in hybrid plasmonic-photonic systems *Phys. Rev. Lett.* **121** 253901

[84] Kodigala A, Lepetit T, Gu Q, Bahari B, Fainman Y and Kant B 2017 Lasing action from photonic bound states in continuum *Nature* **541** 11196

[85] Ha S T, Fu Y H, Emani N K, Pan Z, Bakker R M, Paniagua-Domínguez R and Kuznetsov A I 2018 Directional lasing in resonant semiconductor nanoantenna arrays *Nature nanotech.* **13** (11) 1042

[86] Zhang W, Charous A, Nagai M, Mittleman D M and Mendis R. 2018 Extraordinary optical reflection resonances and bound states in the continuum from a periodic array of thin metal plates *Opt. Exp.* **26** (10) 13195-204

[87] Lepetit T and Kanté B 2014 Controlling multipolar radiation with symmetries for electromagnetic bound states in the continuum *Phys. Rev. B* **90** 241103

[88] Rybin M V, Koshelev K L, Sadrieva Z F, Samusev K B, Bogdanov A A, Limonov M F and Kivshar Y S 2017 High-Q supercavity modes in subwavelength dielectric resonators *Phys. Rev. Lett.* **119** 243901

[89] Bogdanov A A, Koshelev K L, Kapitanova P V, Rybin M V, Gladyshev S A, Sadrieva Z F, Samusev K B, Kivshar Y S, and Limonova M F 2019 Bound states in the continuum and Fano resonances in the strong mode coupling regime *Adv. Photon.* **1** 016001

[90] Friedrich H and Wintgen D 1985 Interfering resonances and bound states in the continuum *Phys. Rev. A* **32** 3231-42

[91] Sadreev A F, Bulgakov E N and Rotter I 2006 Bound states in the continuum in open quantum billiards with a variable shape *Phys. Rev. B* **73** 235342.

[92] Feshbach H 1958 Unified theory of nuclear reactions *Annals of Physics* **5** 4 357-90

[93] Fan S, Suh W and Joannopoulos J D 2003 Temporal coupled-mode theory for the Fano resonance in optical resonators *JOSA A* **20** (3) 569-72

[94] Remacle F, Munster M, Pavlov-Verevkin V B, and Desouter-Lecomte M 1990 Trapping in competitive decay of degenerate states *Phys. Lett. A* **145** (5) 265-268.

[95] Snyder A W and Love J 1983 *Optical waveguide theory* Springer

[96] Plotnik Y, Peleg O, Dreisow F, Heinrich M, Nolte S, Szameit A and Segev M 2011 Experimental observation of optical bound states in the continuum *Phys. Rev. Lett.* **107**(18) 183901

[97] Carletti L, Koshelev K, De Angelis C and Kivshar Y 2018 Giant nonlinear response at the nanoscale driven by bound states in the continuum *Phys. Rev. Lett.* **121**(3) 033903

[98] Minkov M, Gerace D and Fan S 2019 Doubly resonant $\chi^{(2)}$ nonlinear photonic crystal cavity based on a bound state in the continuum *Optica* **6**(8) 1039-1045

[99] Gao X, Hsu C W, Zhen B, Lin X, Joannopoulos J D, Soljačić M and Chen H 2016 Formation mechanism of guided resonances and bound states in the continuum in photonic crystal slabs *Sci. Rep.* **6** 31908

[100] Wiersig J 2006 Formation of Long-Lived, Scarlike Modes near Avoided Resonance Crossings in Optical Microcavities *Phys. Rev. Lett.* **97**(25) 253901

[101] Kikkawa R, Nishida M and Kadoya Y 2019 Polarization-based branch selection of bound states in the continuum in dielectric waveguide modes anti-crossed by a metal grating *New J. Phys.* **21** 113020

[102] Eleuch H and Rotter I 2017 Resonances in open quantum systems *Phys. Rev. A* **95**(2) 022117

[103] Özdemir S K, Rotter S,Nori F and Yang L 2019 Parity-Time symmetry and exceptional points in photonics *Nature Materials* **18** 783-798

[104] Doppler J, Mailybaev A A, B$\acute{}$ohm J, Kuhl U, Girschik A, Libisch F, Milburn T J, Rabl P, Moiseyev N and Rotter S 2016 Dynamically encircling an exceptional point for asymmetric mode switching *Nature* **537** 76-80

[105] Hassan A U, Zhen B, Soljacic M, Khajavikhan M and Christodoulides D N 2017 Dynamically Encircling Exceptional Points: Exact Evolution and Polarization State Conversion *Phys. Rev. Lett.* **118**(9) 093002

[106] Feng L, Wong Z J, Ma R M, Wang Y and Zhang X 2014 Single-mode laser by parity-time symmetry breaking *Science* **346** 972-975

[107] Hodaei H, Miri M A, Heinrich M, Christodoulides D N and Khajavikhan M 2014 Parity-time symmetric microring lasers *Science* **346** 975-978

[108] Liu W, Li M, Guzzon R S, Norberg E J, Parker J S, Lu M, Coldren L A and Yao J 2017 An integrated parity-time symmetric wavelength-tunable single-mode microring laser *Nat. Comm.* **8** 15389

[109] Huang Y, Shen Y, Min C, Fan S and Veronis G 2017 Unidirectional reflectionless light propagation at exceptional points *Nanophotonics* **6**(5) 977-996

[110] Huang Y, Min C and Veronis G 2016 Broadband near total light absorption in non-PT-symmetric waveguide-cavity systems *Opt. Exp.* **24**(19) 22219-22231

[111] Guo A, Salamo G J, Duchesne D, Morandotti R, Volatier-Ravat M, Aimez V, Siviloglou G A and Christodoulides D N 2009 Observation of PT-Symmetry Breaking in Complex Optical Potentials *Phys. Rev. Lett.* **103**(9) 093902

[112] Baum B, Lawrence M, Barton III D and Dionne J 2018 Active polarization control with a parity-time-symmetric plasmonic resonator *Phys. Rev. B* **98**(16) 165418

[113] Lai Y H, Lu Y K, Suh M G, Yuan Z and Vahala K 2019 Observation of the exceptional-point-enhanced Sagnac effect *Nature* **576** 65-71

[114] Hokmabadi M P, Schumer A, Christodoulides D N and Khajavikhan M 2019 Non-Hermitian ring laser gyroscopes with enhanced Sagnac sensitivity *Nature* **576** 70-75

[115] Cerjan A, Hsu C W and Rechtsman M C 2019 Bound States in the Continuum through Environmental Design *Phys. Rev. Lett.* **123**(2) 023902

[116] Tuniz A, Wieduwilt T and Schmidt M A 2019 Tuning the Effective PT Phase of Plasmonic Eigenmodes *Phys. Rev. Lett.* **123**(21) 213903

Acknowledgements

This work was achieved by the great support and direction of teachers and member of my laboratory and many other people.

First of all, I really appreciate my advisor Professor Yutaka Kadoya for numerous directions of my research. Especially, Professor Kadoya took a lot of time to check my slides for the presentation, narrative in the papers and data of the numerical simulations. In addition, he gave me a lot of significant insight to solve the problems that I had faced during the research. I could not have accomplished the research with his direction.

I appreciate Associate Professor Munehiro Nishida sincerely. He checked the outcomes of the research and took a lot of time to derive the theories that were needed to advance my research. In addition, he gave me a lot of important knowledge in doing researches on this thesis, which had resulted in the achievement of the thesis. I would like to show my appreciate again.

I really appreciate Associate Professor Yoriko Tominaga for supporting me during the doctoral course. In this doctoral course, I faced difficulty in doing research many times. In such cases, I was mentally supported a lot.

I really appreciate Associate Professor Holger F. Hofmann. He told me a lot of things such as history, politics and letters in the parties of the laboratory. I also gained knowledge about quantum optics during the conversation, which becomes important knowledge in my research of nanophotonics since the framework of the quantum optics was sometimes applied or used.

Finally, I also appreciate all the people who supported me in the doctoral course.

公表論文

(1) Substrate effects on the optical properties of metal gratings.
Ryo Kikkawa, Munehiro Nishida and Yutaka Kadoya.
Journal of the Optical Society of America B, **34**(12), 2578-2585 (2017).

(2) 半導体基板上金属グレーティングにおける開口下の光増強
吉川遼, 合田圭佑, 上山大輝, 西田宗弘, 角屋豊
レーザー研究, **47**(7), 375-379 (2019).

(3) Polarization-based branch selection of bound states in the continuum in dielectric waveguide modes anti-crossed by a metal grating.
Ryo Kikkawa, Munehiro Nishida and Yutaka Kadoya.
New Journal of Physics **21**, 113020, 1-11 (2019).